INVESTIGATION OF THE MECHANICAL BEHAVIOR OF RIM/BLISTER STRUCTURE HYDRIDE PHASES IN ZIRCALOY-4 BY UTILIZING HIGH ENERGY SYNCHROTRON X-RAY DIFFRACTION

BY

JUN-LI LIN

THESIS

Submitted in partial fulfillment of the requirements
for the degree of Master of Science in Nuclear, Plasma and Radiological Engineering
in the Graduate College of the
University of Illinois at Urbana-Champaign, 2015

Urbana, Illinois

Master's Committee:

Professor Brent J.Heuser, Chair
Professor James F. Stubbins

ABSTRACT

Zircaloy-4 is one of the most common fuel cladding materials used in light water reactors due to excellent mechanical properties, corrosion resistance and low thermal neutron absorption cross-section. However, in service absorption of hydrogen by Zircaloy-4 (Zry-4) cladding is potentially problematic. One issue is the delayed hydride cracking (DHC) phenomenon which occurs during storage of used nuclear fuel (UNF). DHC is a time-dependent subcritical crack growth mechanism that can be induced by tensile stress hoop stress within the fuel cladding, even when this hoop stress is lower than the yield stress of the cladding materials. DHC eventually leads to the failure of the cladding, potentially resulting in the release of radioactive fission gas inside the storage casks. This naturally increases the difficulty of transportation of UNF to a permanent storage site. The root-cause of the DHC is hydride re-orientation, where, under sufficient stress, plate-like hydrides dissolve and reprecipitate with plate normal axis parallel to the stress axis. Hydride reorientation provides a brittle pathway for crack propagation and may potentially decrease the lifetime of UNF in storage.

The concern of DHC have engendered studies of the microstructure and mechanical response of the hydride phase to externally applied tensile stress in order to understand hydride reorientation behavior. In this thesis, the mechanical response of the δ zirconium hydride phase in Zry-4 material under an applied load at the temperature similar to the dry cask storage was investigated. More specifically, the stress-strain behavior of the zirconium and zirconium hydride phases were studied at 200 °C with different hydrogen concentrations. The hydride phase was intentionally created with a rim/blister (a region with high density of hydride) within the sample, similar to the hydride rim/blister observed in UNF cladding material.

High energy synchrotron X-ray diffraction at the APS 1-ID was utilized to study the

mechanical response of hydride and matrix phase with the rim/blister distribution in a cold worked stress-relieved (CWSR) Zry-4 sheet. The only hydride phase observed in the Zry-4 sheet material for hydrogen concentration from 97 to 977 weight parts per million (wppm) is the δ phase. The lattice strain evolution of δ zirconium hydride and the α zirconium phase as a function of the applied stress was studied. Two stages of different stress-lattice strain behaviors were identified. Load partitioning between the zirconium matrix phase and the hydride phase is responsible for this change in behavior. The highest internal stress or the effective von Mises stress was analyzed on the δ (220) hydride plane. The degree of load transfer from the matrix to the hydride phase increased as hydrogen content increased in the samples. This load transfer may potentially lead to the early fracture of the brittle hydride phase.

The evolution of the full-width at half maximum (FWHM) and the integrated diffraction intensity was also studied. The FWHM of δ (220) hydride reflection decreased in the direction parallel to the applied stress axis and increased in the direction perpendicular to the applied stress axis, which is inconsistence with published results of the FWHM signature of reoriented hydride. The integrated diffraction intensity of δ (220) hydride reflection only slightly decreased in the direction parallel to the applied stress axis and remained unchanged in the direction perpendicular to the applied stress axis. Therefore, no strongly direct evidence of hydride reorientation was observed, which implies that the hydride blister/rim structure is fairly stable under the environment tested in this study.

TABLE OF CONTENTS

LIST OF TABLES

LIST OF FIGURES

CHAPTER 1

INTRODUCTION

1.1 Fuel storage issue

Since early 1980s, the need for additional storage became an important issue due to increasing amount of used nuclear fuels (UNF). Because the postponed of Yucca Mountain Nuclear Waste Repository, it has came to a conclusion that the only viable option is to store the used fuel interim on site and cooperate with dry-cask storage which is certified by NRC to store fuels for at least 100 years [18]. However, because of the limited capacity of on-site storage pool, the dry storage has been considered as an alternative way to store UNF till the fuel reprocessing or final disposal location has been decided [19, 20]. The primary structure component of UNF is the cladding. Any possible forms which lead to the failure of the cladding may result in serious contamination and make it infeasible to be retrieved from the storage site. Thus the primary concern for designing the dry storage is to assure the integrity of the fuel cladding [19].

Creep has been known as a dominant mechanism which leads to deformation and failure of the cladding [19]. Since 1990s, many studies have focused on cladding creep testing under high storage temperature and stress. These efforts have demonstrated that the hoop stress which is generated by thermal expansion of cladding will result in significant creep deformation [21, 22]. Base on this, the Interim Staff Guidance-11 Revision 3, which is the latest document concerning about cladding integrity by NRC, suggests that at normal storage temperature (less than 400°C) the storage cladding should not experience gross rupture since the temperature of cladding will decrease slowly over time and so does the hoop stress and the creep rate [19]. However, there are other phenomena such as delayed hydride cracking (DHC) which also has potential to cause failure of storage cladding but had not been addressed in

the report. The illustration of the DHC is in the latter section.

1.2 Application of zirconium alloys

Zirconium alloys are commonly used in today's nuclear reactors because of the combination of their high strength, high corrosion resistance and low thermal neutron absorption cross-section which is a critical factor to sustain the fission chain reaction. Pure zirconium has been alloyed with several different elements, such as tin (Sn), iron (Fe), chromium (Cr), nickel (Ni) and niobium (Nb) in order to improve its properties [1]. Table 1.1 lists the standard chemical specifications of three most commonly applied zirconium alloys. Zr-2.5Nb alloy is used in CANDU reactors and Russian RBMK reactors [23, 24]. Zircaloy-2 (Zry-2) and Zircaloy-4 (Zry-4) alloys are commonly used in boiling water reactors (BWR) and pressurized water reactors (PWR) [23, 24] in the United States as structural material and fuel cladding. In BWR, several components such as fuel rods, bottom and top end plugs and fuel channel boxes are builded by Zry-2, and spacer grids is builded by Zircaloy-4. The main difference between Zry-2 and Zry-4 is the replacement of Nickel by Iron, which reduces the amount of hydrogen pick up by Zry-4 [25]. Thus Zry-4 is more suitable for more significant hydrogen dissolving operating environment in PWR. However, the cladding in PWR and BWR is more susceptible to DHC than cladding in CANDU and RBMK reactor. The reasons are the former has higher operating temperature and longer fuel cycle, which results in higher total hydrogen absorption amount during life time of the cladding. The discussion in this thesis will mainly focus on the Zry-4 (UNS R60804) cladding.

Table 1.1: Standard chemical composition of three zirconium alloys listed as atomic percent, from ASTM standard B353 [1]

	Zircaloy-4 (UNS R60804)	**Zircaloy-2 (UNS R60802)**	**Zr-2.5Nb (UNS R60904)**
Tin	1.20-1.70	1.20-1.70	...
Iron	0.18-0.24	0.07-0.2	...
Chromium	0.07-0.13	0.05-0.15	...
Nickel	...	0.03-0.08	...
Niobium(columbium)	...	...	2.5-2.8
Oxygen	†	†	†

†The permissible oxygen amount need to be specified when purchased the material [1].

1.3 Delayed hydride cracking during dry storage

Delayed hydride cracking (DHC) is a time-dependent mechanism of cracking which involves localized hydride precipitation at stress concentrators under tensile loading that eventually leads to cladding failure. hydrides tend to precipitates locally at regions where the flaw and crack (regions with the maximum tensile stress) existed, embrittle the area and generate new crack. Repeating of the mechanism leads to subcritical crack growth of materials [23]. Three stages have been characterized in DHC and are shown in Fig. 1.1 [2]. Crack growth velocity increases rapidly with increases stress intensity factor (K) in Stage I, follows by Stage II where crack growth velocity is a constant and independent of K. Unstable crack growth then takes place in Stages III after the critical K is exceeded [3].

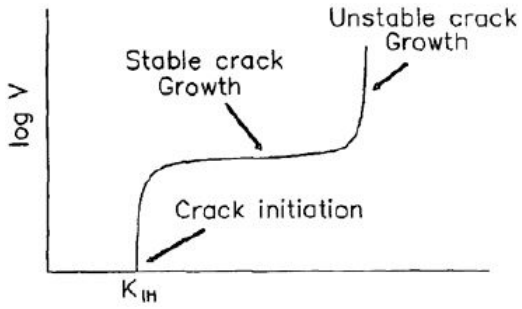

Figure 1.1: Three stages with different crack growth velocity depend on stress intensity factor [2].

Simpson and Ells first reported the failure of experimental nuclear fuel element Zr-2.5Nb alloy end cap welds after long term storage (1.5 year) at room temperature [26]. They came to a conclusion that despite these elements were stored at the low temperature, there still existed a driving force for hydrogen diffusion and accumulate on the internal notch between the welds end cap and the cladding. The notches were generally created by resistance force between the cladding and the weld. Accumulation of local hydrogen then started precipitating when the hydrogen concentration surpassed the solvus line. Cracks were formed when length of individual hydrides reached the critical value. Latter, Coleman and Ambler reported a similar observation on delayed hydrogen cracking in Zr-2.5Nb alloys [27]. These two observations verified the diffusive nature of this mechanism and confirmed that concentrated stress at crack tips will effectively enhance the growth of hydrides.

It is clear that fuel cladding in long term dry storage will have risk of failure if flaws are presence on the interface of cladding and fuel pellet. A common mechanism which will cause the formation of incipient crack inside cladding is known as pellet-cladding mechanical interaction (PCMI) [28]. PCMI is caused by the different amount of expansion between the fuel and the cladding tube which leads to direct contact of the two elements. PCMI posts a threat to cladding integrity either during operation (due to creep and possible consequent failure by strain fatigue) or post-use storage (incipient crack may exist inside the cladding due to PCMI) especially for high burn up fuels, since the PCMI induced strain can be assumed proportional to the heat load of the reactors [28].

Dutton et al. have formulated the first DHC model by combining the effect of stress gradient on hydrogen diffusion and stress assisted hydride precipitation [3]. Fig. 1.2 shows a cylindrical geometry used in this model, where $r = \ell$ is the center of the crack and $r = L$ is the average distance between hydrides. The hydrostatic stress at $r = \ell$ affects the local hydrogen terminal solubility, which results in different hydrogen concentration between $r = \ell$ and $r = L$ (concentration is lower at $r = L$ since hydrides precipitate at $r = \ell$). In addition, the local tensile stress is higher than the tensile stress which is far from the crack tip (at $r = L$). The stress gradient between ℓ and L also contributes to hydrogen diffusion. Thus crack growth rate can be calculated by inserting the ideal morphology of hydrides and assuming that the crack growth rate is equal to the average hydride precipitation rate

(hydrides form cracks as soon as they precipitate). Crack growth forms two different stages in this model. Stage I is controlled by elastic behavior at the crack tip and is highly dependent on the stress. Stage II is controlled by plastic behavior at the crack tip but has weak dependence on the stress [3].

In order to prove the effect of stress on terminal solid solubility of hydrogen in Zr-2.5Nb alloy, a neutron diffraction experiment was preformed at Argonne National Laboratory to measure the partial molal volume of deuterium (deuterium was used in this experiment to increase neutron scattering intensity) in the solution ($\bar{V}_H$) and partial molal volume of deuterium in the deuteride phase ($\bar{V}_H^h$) [29]. The difference between the $\bar{V}_H$ and $\bar{V}_H^h$ was used to determine the effect of stress on the terminal solution solubility with the following equation [29]:

$$C_\sigma^s = C_0^s exp[\frac{P(\bar{V}_H^h - \bar{V}_H)}{RT}] \tag{1.1}$$

where C_σ^s and C_0^s are the terminal solid solubilities with and without a hydrostatic stress P, respectively. The result shows that the difference between partial molal volume of deuterium in the two phases is minor, which is at most -0.27 even with high applied stress

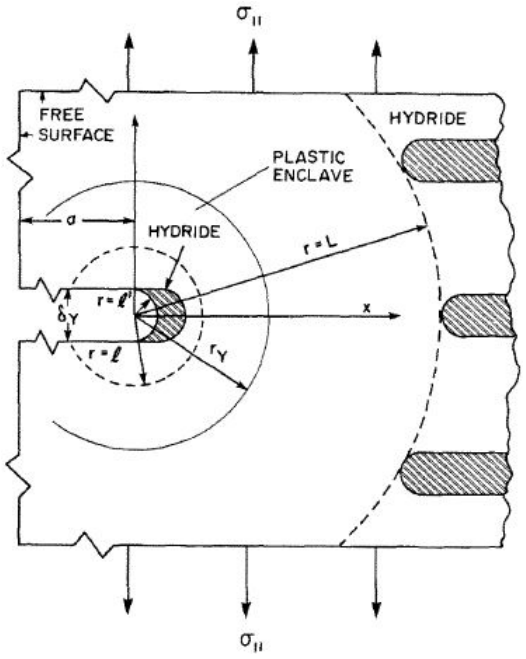

Figure 1.2: Schematic of the assumption geometry of the hydride and the crack proposed by Dutton et al. [3].

(500MPa) [29]. The observation is in contrast with Dutton-Pul's DHC model, which predicts the effect of stress on the local terminal solubility would be significant enough to create a concentration gradient between the crack tip and bulk region and generates enough driving force for hydrogen diffusion [3]. However from Eq. (1.1) such effect would just be minor and is not able to support previous observation, which crack propagates in relatively high rate [26, 27].

Another DHC model was recently proposed by Kim [2]. Kim's model is based on the hysteresis effect on the terminal solid solubility (TSS) of hydrogen in zirconium solution, which is the result of the volume difference between zirconium matrix and zirconium hydride. This volume difference is due to the precipitation of δ hydrides in zirconium and is postulated by Weatherly [30] from the analysis on the volume difference between γ hydrides and pure zirconium matrix. The volume difference was determined can be as large as 17% for most of the δ hydride habit planes. During cool-down, the equilibrium TSS is determined as the point where increase of lattice strain energy (due to precipitation of δ hydride which has larger volume) and decrease of lattice strain energy (due to hydrogen is taken out from the solution) is balanced. Increase of lattice strain is larger due to large volume difference between hydrides and matrix, which causes hydride formation being suppressed and leaves supersaturated hydrogen solid solution [2]. Thus TSS is raised during cool-down. However during the heat-up, the hydrogen content which can be dissolved into the matrix is reduced, since the lattice strain energy is consumed by forming dislocations in plastically deformed matrix around hydrides. Thus TSS decreases during the heat-up [2]. Mechanism of Kim's model is illustrated in Fig. 1.3 [2]: A specimen with specific amount of hydrogen is heated up to the peak temperature (point A) follows up by cool-down to the test temperature (point B). TSS follows the TSSD line while heat-up and TSSP line while cool-down. If TSSD at the peak temperature is lower than TSSP at the test temperature (point A and point B in Fig. 1.1), the supersaturated hydrogen solution will be formed. If any cracks exist in the specimen while external tensile stress is applied, the work energy which is given by the stress will balance the increase of strain energy by forming hydrides and becomes a trigger of hydrides nucleation. The supersaturated solution at point B will then be brought down to the equilibrium point of TSSD (point C). However for bulk region which is far from

the crack tip the hydrogen concentration remains at B due to the smaller tensile stress. This creates a concentration gradient between B and C which becomes the primary driving force for DHC [2]. Kim concluded that the maximum concentration gradient ($\triangle C_{max}$) is the difference between TSSD and TSSP at any temperature, and since the driving force originates from the hysteresis of TSS between heating and cooling, DHC may exist in any metals which experience hysteresis effect during hydride precipitation [2].

More recent, Chao et al. have applied finite element analysis with computer code ANSYS (2000) and strain energy density theory to study the relationship between crack length, crack orientation and strain energy density factor. The result shows that the presence of radially oriented hydrides significantly increases the chance of cladding failure [31].

Despite so many effort has been done to understand the mechanism of DHC, a model which can predict accurate crack growth rate and the life time of dry storage cladding quantitatively has not been formulated yet. Also there is controversy exists between existing DHC models. Kim's model [2] suggests that externally applied stresses lead to precipitation of hydrides on crack tips and dissolution of hydrides at bulk region; however Dutton's model [3] suggests that significant lattice strain around crack tips due to volume difference between hydrides and material matrix leads to dissolution of matrix hydrides. In view of this, it is important

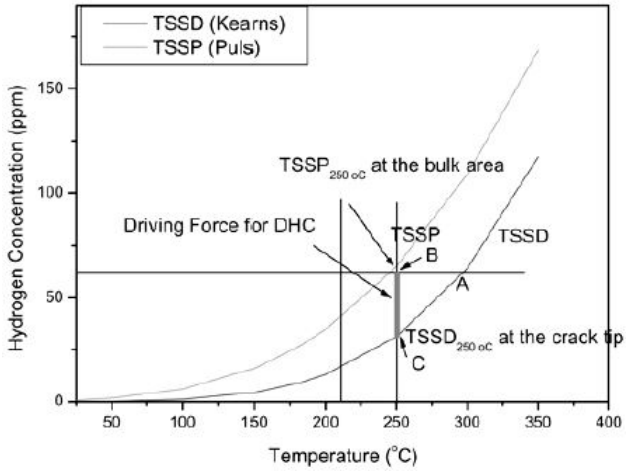

Figure 1.3: The TSSP [4] and TSSD [5] line of hydrogen in Zr-2.5Nb tube sample. The high stress at the crack tip acts as a trigger for hydrides nucleation and results in concentration gradient between crack tip and bulk region(from point B to point C), which is the main driving force for DHC [2].

to re-examine the properties of hydride phase in zirconium based material and the influence of hydride on properties of the matrix.

This thesis used high energy X-ray in Advanced Photon Source(APS), which is the third generation synchrotron source located at Argonne National Laboratory, to study the mechanical response of hydride phase with *in-situ* tensile testing and wide angle x-ray diffraction. Different from conventional x-ray source, high energy x-ray in APS has lower absorption cross section and higher penetration ability, and is a optimum tool to study weak hydride phase in Zry-4 matrix [32]. The goal of this thesis is to investigate the fundamental mechanical properties of hydrides phase and its mechanical response while tested under environment that is relevant to the storage conditions, which gives solid foundation for the future DHC model development.

CHAPTER 2

LITERATURE REVIEW

2.1 Zircaloy-4 cladding

Hexagonal close-packed (hcp) α phase and body-centered cubic (bcc) β phase are two crystallographic structures exist in pure zirconium. The phase transformation temperature of α to β phase is near 1440 K and the melting temperature of zirconium is 2123 K at atmospheric pressure [33]. The relationship between the α and β-Zr is

$$[0001]_\alpha//[110]_\beta \text{ and } (11\bar{2}0)_\alpha//(111)_\beta$$

The transformation process is very similar to diffusionless martensite formation or bainite formation. The major difference from martensite formation is when slowly cooled from β phase to α phase, needle α phase precipitates slowly in the β phase matrix [34]. Lichter's [35] data gives accurate calculation for temperature dependence of lattice parameters for high purity α-zirconium, which is:

$$a_0(t^\circ C) = 3.23118 + 16.626 \times 10^{-6}(t-25) \tag{2.1}$$

$$\begin{aligned} c_0(t^\circ C) &= 5.14634 + 47.413 \times 10^{-6}(t-25) \\ &- 32.859 \times 10^{-9}(t-25) + 95.161 \times 10^{-12}(t-25)^3 \\ &- 50.722 \times 10^{-15}(t-25)^4 \end{aligned} \tag{2.2}$$

Both a_0 and c_0 increase as temperature increases. According to Eq. (2.1) and Eq. (2.2) the c/a ratio in α-zirconium can be calculated and is expected to increase nonlinearly with

temperature because of c_0:

$$\begin{aligned} c/a(t^{\circ}\mathrm{C}) = 1.59271 &+ 6.283 \times 10^{-6}(t-25) \\ &- 9.628 \times 10^{-9}(t-25)^2 + 28.981 \times 10^{-12}(t-25)^3 \\ &- 15.698 \times 10^{-15}(t-25)^4 \end{aligned} \tag{2.3}$$

Zirconium is known to be susceptible to corrosion environment in nuclear reactor, such as oxidation on the water side of cladding and the uptake of hydrogen. Thus alloying development strategies for zirconium is necessary. During the development, a batch of zirconium materials was accidentally contaminated with tin (Sn) and was observed to have better corrosion resistance than pure zirconium. Further studies have observed some impurities such as nitrogen, aluminum and titanium has deleterious effect on corrosion behavior of zirconium, which can be remedied by adding tin. Other elements such as tantalum also has ability to reduce the harmful effect from impurities, but tin is less poisonous to nuclear reaction, which made future fuel cladding development focuses most on zirconium-tin system. Different from the United States, Canada and Soviet Union has concentrated much on zirconium-Nb alloys which has superior mechanical properties and adequate corrosion resistance [36]. Three most commonly applied zirconium based alloys and their standard chemical composition are listed in Table 1.1.

Major alloying element for Zry-4 is tin with composition of $1.2-1.8\%$. Fig. 2.1 shows the binary phase diagram of zirconium-tin system [6]. Tin is an α stabilizer and remains in solid solution in zirconium matrix and strengthens the zirconium by solid solution strengthening [24]. Other alloying elements such as iron and chromium have low solubility in zirconium and form second phase particles (SPP). The dominant SPP in α-recrystallized Zry-4 is $\mathrm{Zr(Fe,Cr)_2}$ with hexagonal crystal structure and for β-quenched Zry-4 (quenched from $\alpha+\beta$ or β phase field), it is $\mathrm{Zr_4(Fe,Cr)}$ with face-centered cubic crystal structure [37,38]. Different distributions of SPP have different effects on corrosion resistance of Zry-4 matrix. The chainlike $\mathrm{Zr_4(Fe,Cr)}$ maintains high electric conductivity of surface $\mathrm{ZrO_2}$ film, which limits the reaction of hydrogen with cladding on the surface zirconia and prevents occurring of nodular corrosion. However the dispersion of $\mathrm{Zr(Fe,Cr)_2}$ particles decrease the corrosion

resistance of α-recrystallized Zry-4 [37].

Common thermomechanical manufacture processes similar to other industrial alloys have been adopted after Zry-4 ingots were melted. These processes include forging at temperature range within β phase, followed by water quenching from homogenous β phase in order to increase the corrosion resistance. Forging or rolling then is performed at intermediate temperature in α phase ($> 750°C$) [24, 39]. Extrusion would also be performed to fabricate cladding tubes. Two common tube diameters nowadays after tube-reduced extrusion are 10.9 mm (Supertrex) and 7.6 mm(Trex) [39]. Supertrex later has became the most common extrusion process. Cold rolling is performed to homogenize the distribution of precipitation followed by final annealing treatment. Final annealing is done at different temperatures to fulfill different applications. Annealing temperature of 600 °C is generally used for Zircaloys to achieve full recrystallization and retain the ductility of the material. Lower annealing temperature would be chosen to achieve stress-relived condition if the purpose is to improve mechanical properties of the material [24].

Zirconium has the typical basal pole orientation with the c/a ratio less than 1.633 ($c/a < 1.633$). The basal pole aligns perpendicular to the rolling direction and tilts $\pm 20°$ to $\pm 40°$

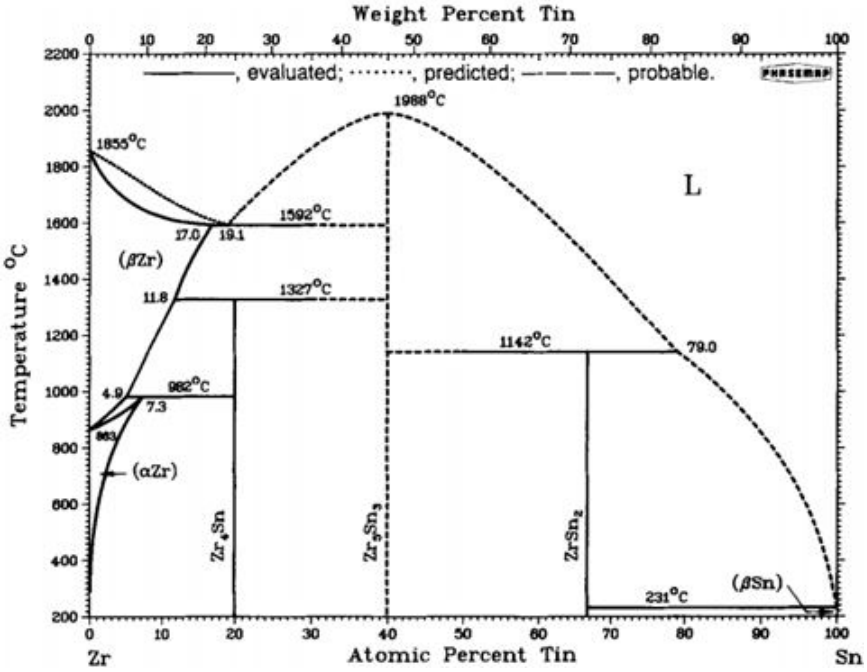

Figure 2.1: Zr-Sn binary phase diagram [6].

toward transverse direction from normal direction. Development of texture in Zry-4 varies differently with different material shapes (tube or sheet) and different final annealing treatments. General phenomenon has been observed as basal planes will always align parallel to the primary deformation. However, the final orientation of basal pole varies differently depending on the deformation and final annealing conditions [40]. For example for Trex or Supertrex treatment which the reduction of wall thickness is usually greater than the reduction of tube diameter, the greater compressive stress is generated in radial direction which aligns the basal pole directly to the normal direction. For cold-rolled and stress-relived Zry-4 materials, the typically basal poles alignment is perpendicular to the rolling direction and tilts $\pm 30^\circ$ to $\pm 40^\circ$ toward transverse direction from the normal direction [24, 39, 40]. Comparing with the deformation process, annealing has little effect on basal pole alignment but will change the pole figure of prism $(11\bar{2}0)$ and pyramidal planes $(10\bar{1}0)$. For cold-worked materials, the $[10\bar{1}0]$ aligns parallel to the rolling surface; after being treated in recrystallized condition, basal plane will rotate $\pm 30^\circ$ based on its axis which aligns the rolling direction with the $[11\bar{2}0]$ [11, 24, 40]. Thus an effective measurement for degree of recrystallization is to calculate the ratio of pole density of $(10\bar{1}0)$ to $[11\bar{2}0]$ in the rolling direction [11]. This ratio is high for heavy cold worked zirconium alloys and decreases as increases of degree of recrystallization.

Similar to other h.c.p metals (magnesium and titanium for example), zirconium lacks of slip systems. The two main deformation mechanisms for zirconium are slip and twinning. The primary slip system is prism slip on $\{10\bar{1}0\}$ plane in $\langle 1\bar{2}10\rangle$ direction. However, zirconium is observed to high ductility so other deformations must exist to satisfy Von Mises compatibility criterion (at least 5 independent deformation modes must exist to ensure deformation of a grain). Therefore prime plane slip in the (c+a) direction is often suggested to explain the high ductility of zirconium [40]. Other slip systems such as pyramidal planes $\{10\bar{1}1\}$ and $\{11\bar{2}1\}$ in (c+a) direction will also be activated if increases deformation temperature [24, 40]. Twinning system usually happens on $\{10\bar{1}2\}\langle\bar{1}011\rangle$ or $\{11\bar{2}2\}\langle\bar{1}\bar{1}23\rangle$ system when tensile or compressive stress is applied on c axis, respectively. Activation of twinning and slip depend on several factors such as Schmid factor, alloying elements, grain orientation and temperature. Although prism slip system has lower critical resolved stress, twinning is

activated before slip due to stronger dependence of Schmid factor on position of poles and stress direction. Generally, twinning is preferred at low temperature and slip is preferred at high temperature [24, 40].

After all the treatments, the final product of Zry-4 has higher minimum yield strength than the pure zirconium, which caused by strengthening effect from the SPPs. At the room temperature, the minimum yield strength of Zry-4 is 240 MPa in longitudinal direction [41], and can be increased to 400-450 MPa after final stress-relived treatments [24]. It is also worth noting that due to the anisotropic behavior of zirconium, the transverse direction normally has the highest tensile strength [40].

2.2 Hydriding of Zircaloy cladding

Unlike neutron irradiation which affects mechanical properties of cladding at the early fuel circle and soon becomes saturation, the corrosion and hydriding of cladding become more serious when it comes to the end of the fuel cycle. Hydrogen is created by radiolysis of water at the normal operation condition by the following reaction:

$$2H_2O \rightarrow H_2O_2 + H_2 \tag{2.4}$$

Zircaloy cladding also reacts with the water to form zirconia (ZrO_2) and generates hydrogen during the service in reactors:

$$Zr+2H_2O \rightarrow ZrO_2 + 4H \tag{2.5}$$

Part of hydrogen recombines to form hydrogen gas, while some hydrogen transports through the zirconia layer and reaches the fresh cladding matrix. The fraction of hydrogen transports into the metal depends on the flow velocity of the water and the thickness of the zirconia layer. Thicker zirconia layer usually has more surface defects such as cracks and pores, which trap hydrogen and reduce the fraction of hydrogen moving into the metal. At normal operating conditions of PWRs the hydrogen transportation fraction first decreases as the

oxide thickness increases, and reaches a constant ($\sim$ 15%) when oxide layer grows over 50µm [42]. Hydrides then precipitate when the hydrogen concentration in the cladding exceeds the terminal solid solubility (see Fig.1.3).

Early observation by X-ray and metallographic analysis has identified three distinct zirconium hydride phases, which are δ, ϵ, and the metastable γ phase [7,43]. The δ hydride forms f.c.c in the zirconium sublattice with extended stoichiometry from $ZrH_{1.59}$ to $ZrH_{1.66}$ [43]. Orientation relationships between the δ hydride and the α zirconium are [44]

$$(111)_\delta//(0001)_\alpha,\ (1\bar{1}0)_\delta//(11\bar{2}0)_\alpha$$

$$(111)_\delta//(10\bar{1}0)_\alpha,\ (1\bar{1}0)_\delta//(11\bar{2}0)_\alpha$$

ϵ phase has the face-centered tetragonal structure with $c/a > 1$ and exists from $ZrH_{1.67}$ to ZrH_2. γ hydride phase has face-centered tetragonal structure with $c/a < 1$ (but less than ϵ) and is only stable at stoichiometry of ZrH [23, 43]. Orientation relationships between γ and α zirconium phase are [30]

$$(111)_\gamma//(0001)_\alpha,\ (1\bar{1}0)_\gamma//(1\bar{2}10)_\alpha$$

$$(001)_\gamma//(0001)_\alpha,\ (1\bar{1}0)_\gamma//(1\bar{2}10)_\alpha$$

Fig. 2.2(a) shows the binary phase diagram of hydrogen-zirconium system. Formation and equilibrium of the γ hydride phase has long been a controversy. From the variation of peak intensities of hydride phases from the x-ray diffraction, Beck [7] concluded that the γ phase is a metastable phase and is a high temperature product from the δ phase. Barraclough and Beever [43] have observed the precipitation of banded γ hydride in the δ matrix which indicated the change of δ phase composition from eutectoid to room temperature (see high hydrogen content part in Fig. 2.2(a)) is a result of the formation of γ hydride. This observation further supports Beck's assumption. Similar observation from the Zry-2 cladding fuel pin which was served in the BWR (with burn up of 12000 MWd/t UO_2) was reported, where γ phase was observed to be contained in massive δ phase [45]. Nath et al. [8] has

quenched and furnace cooled the zirconium sheets with 500 wppm hydrogen and followed by aging at $150°C$, $200°C$ and $250°C$ for three weeks. Precipitation of full γ phase after being quenched and full δ phase after being furnace-cooled was observed. The final aging then leads to full replacement of the γ by the δ phase and has no influence on the original δ phase, which indicates the δ is a stable hydride phase at room temperature.

Studies on the effect of cooling rate on hydride phase formation observed that the fraction of γ hydride decreases with decreases cooling rate [8, 44, 46], since slow cooling rate is not able to build up enough hydrogen supersaturation for γ phase nucleation. Bradbook et al. [44] quantified this cooling rate and concluded that for cooling rate less than 10 $°C\,min^{-1}$ the δ phase will precipitate mainly; on the other hand when the cooling rate is greater than 10 $°C\,min^{-1}$ the γ phase becomes more dominant. Same behavior was also observed in Zr-20%Nb alloy [47].

In contrast to those observations, Bailey [48] observed full precipitation of the γ hydride in both quenched and slow-cooled samples with hydrogen content ranged from 10 wppm to 500 wppm by using x-ray and electron diffraction. Another study by Mishra et al. [9] observed the γ phase was stable at the room temperature which had not been affected by ageing and can be decomposed easily to α and δ phase when heated over 250 °C. Mishra et al. then concluded that the γ was formed by a peritectoid reaction which was $\alpha + \delta \rightleftharpoons \gamma$ at around 250 °C. In addition, Cann and Atrens [49] and Weatherly [30] observed the full γ precipitation in samples with hydrogen content of 4-230 wppm after being furnace-cooled. A modified hydrogen-zirconium phase diagram was proposed by Mishra et al. which is shown in Fig. 2.2(b) [9].

Because of the disagreement among these observations, Cann et al. [50] studied other factors which might affect the hydride precipitation. In this study, four metallurgical factors were investigated (alpha zirconium grain size, heat treatment temperature, impurity and hydriding technique) on pure zirconium rod with hydrogen content of 25-200 wppm and concluded that only the specimen purity (oxygen impurity) would affect the hydride precipitation phase. The δ phase was observed to be dominated when oxygen level was over 1000 wppm (except for low hydrogen content) while γ phase became dominant when oxygen was below 200 wppm.

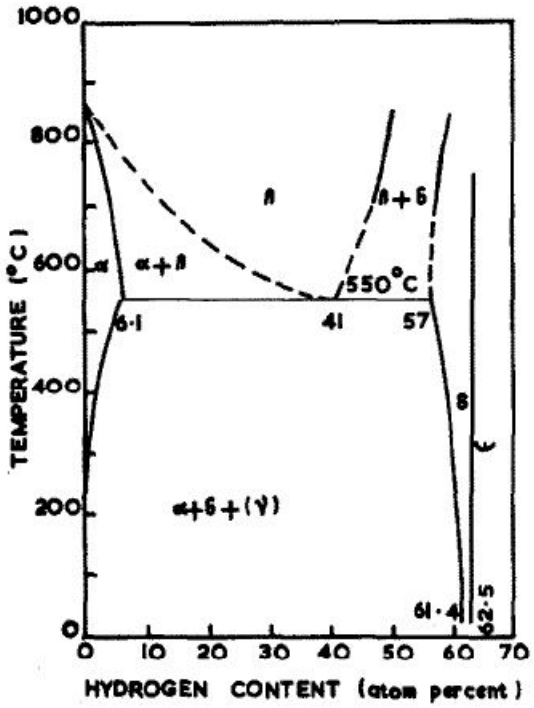

(a)

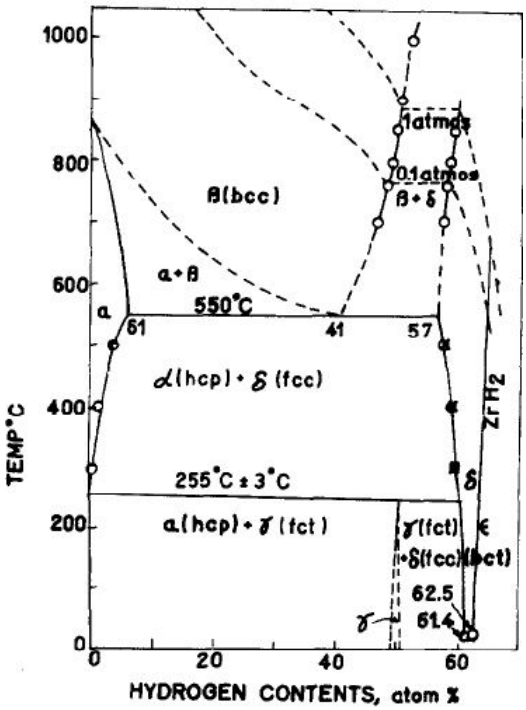

(b)

Figure 2.2: Zr-hydrogen phase diagram by (a) Beck [7] (reprinted from Nath et al. [8]) and (b) Mishra et al. [9].

Recent studies utilized synchrotron x-ray to identify and quantify hydride phases in Zirconium alloys [51, 52]. For quantification of hydride phases, an estimated volume fraction can be calculated by using the ratio of the integrated diffraction intensity of each phase [51, 53]. For example:

$$\frac{I_{\delta(111)}}{I_{\alpha(002)}} = \frac{R_{\delta(111)}V_{\delta}}{R_{\alpha(002)}V_{\alpha}} \tag{2.6}$$

where R is a volume fraction related factor which takes into account the characteristic of crystallographic properties of each plane:

$$R_{hkl} = (\frac{1}{\mu^2})[|F|^2_{hkl}p_{hkl}(\frac{1}{\sin^2\theta_{hkl}\cos\theta_{hkl}})](e^{-2M})_{hkl} \tag{2.7}$$

where μ is the volume of unit cell, $|F|^2$ is the structure factor, p is the multiplicity factor, θ is the Bragg angle for each plane (hkl) and e^{-2M} is the temperature factor. Eq. (2.7) was further modified by Daum et al. [51] by taking into account the crystallographic texture factors. Daum et al. [51] then applied this method to study the hydrogen content in CWSR Zry-4 materials with both uniform and non-uniform (hydride rim) hydride distribution; good agreement was observed between the calculated and the measured value. In Daum et al's study, the δ hydride phase was identified predominantly in both uniform and non-uniform cases. For hydrogen content greater 1250 wppm, both γ and δ phase were seen, while ϵ hydride was only observed when hydrogen content was over 3000 wppm in the material which had hydride rim structure. Another study by Tulk et al. [52] focused on the effect of matrix strength on the stability of δ and γ hydride phase in different zirconium based alloys. It was observed that increased the yield strength of Zry-2 would suppress the formation of γ phase. The possible explanation is that since γ phase has lower hydrogen enrichment, γ phase will precipitate more particles for a certain hydrogen content compares with the δ phase, thus generates more strain. This causes γ hydride to be suppressed in harder materials quench is performed to intentionally precipitate the γ phase. However, this trend was not observed in Zr-2.5%Nb, which indicates that niobium rich β-Zr phase has ability to stabilize the γ phase. Other important observations such as only $\gamma \rightarrow \delta$ was observed during the *in-situ* heating test in both Zry-2 and Zr-2.5%Nb alloys further implies that γ phase is

a metastable zirconium hydride phase.

ϵ hydride phase was commonly observed at high hydrogen content [7, 43, 51, 54–56]. A common conclusion was made such that the transformation of $\delta \rightarrow \epsilon$ phase involved the martensitic type f.c.c$\rightarrow$ f.c.t transformation. Kempter et al. [54] measured the thermal expansion of two hydride phases by using X-ray diffraction and observed the ϵ phase was stable at $ZrH_{1.92}$. Barraclough and Beevers observed the transformation started at $ZrH_{1.67}$ and extended to ZrH_2 and associated with decreased of microhardness [43]. Cassidy and Wayman [55] observed spear morphology in the ϵ phase at $ZrH_{1.67}$, which was a typical microstructural characteristic of martensitic transformation.

Finally, Zhao observed a new hydride phase in Zry-4 with hydrogen content of 210 wppm by using the electron microdiffraction technique and the electron energy loss spectroscopy (EELS) [57]. The new hydride phase was named ζ phase and belonged to trigonal crystal system with a space group of P3m1.

Many recent studies on zirconium hydride phase have taken the advantageous of high energy synchrotron x-ray diffraction, which is an ideal technique for studying the minor phases in a matrix [14, 51, 52, 58–61].

The crystallographic texture of hydrides was studied by dividing the Debye ring into 72 incomplete pole figures (5° for each segment) and applied into the MTEX or E-WIMV algorithm to determine the ODF [59, 61]. Santisteban et al. [59] and Alvarez et al. [61] observed the well-known relationship between the δ and α zirconium phase in Zr-2.5%Nb alloy, which is $((111)_\delta//(0001)_\alpha, (1\bar{1}0)_\delta//(11\bar{2}0)_\alpha)$, by using the algorithm. Same orientation relationship was also observed for samples with a hydride blister structure by Alvarez et al. [61], which indicates that the formation of hydride blister will not affect the texture development of the hydride phase.

Hydrides dissolution and precipitation kinetics in zirconium based alloys was also studied by synchrotron x-ray diffraction [60,62]. Studies of dissolution and precipitation of hydrides were based on the variation of diffraction intensities of hydride phase peaks. Colas et al. [60] determined the dissolution temperature (T_d) and precipitation temperature (T_p) by studying the variation of integrated δ (111) peak intensity in a fully recrystallized Zry-2 bar and CWSR Zry-4 sheet. The result of two materials were in a good agreement with previous literature

where the differential scanning calorimetry (DSC) was used to study the (T_d) and (T_p) [63]. Cooling and Heating rate was observed to have little effect on the (T_d) and (T_p) in this study. In stead of studying the δ (111) peak, Zanellato et al. [62] studied the change of intensity on δ (311) peak in a recrystallized Zry-4 sheet. In this study, the evolution of hydrogen content in solid solution as the function of temperature can be fitted into the classical Arrhenius equation:

$$[H] = Aexp(-Q/RT) \tag{2.8}$$

where $[H]$ is the content of hydrogen in the solid solution and Q is the activiation energy for hydride precipitation. The result of T_d and T_p was also in good agreement with previous studies. They also observed the change of slope in Arrhenius plot in low temperature range (from the room temperature (RT) to 200 °C) which indicates the decrease of Q in that range. This might be caused by changing of hydride microstructure or phases at the low temperature. Later, the shift of Q in low temperature range was also been observed by Colas et al. [13], who studied the effect of thermal cycles on hydride reorientation in CWSR Zry-4 sheets. In contrast to [62], they observed an increase of Q at low temperature range with the transition temperature at 230 °C. However, this was only observed in a sample which had radially reoriented hydrides. For samples with only circumferential hydrides, the Q_{circum} remained as a constant and was much lower than Q_{radial}. All the above studies observed that both T_d and T_p for hydrides in zirconium based alloys is hardly affected by the heating or cooling rate, stresses, thermal cycles and orientation of hydrides. The reorientation of hydride will be discussed in the next section.

2.3 Reorientation of hydrides in Zirconium based cladding

A phenomenon observed during DHC is called hydride re-orientation, where, under sufficient stress, plate-like hydrides dissolve and precipitate parallel to the redial direction. Hydride re-orientation provides a brittle pathway for crack propagation decreasing the lifetime in storage. For typical Zircaloy fuel cladding in LWRs, hydride plates precipitate preferentially in the circumferentially direction (plates grow along the longitudinal direction

with normal direction of surface parallel to the radial direction of the cladding). However when external tensile stress is applied on the cladding, hydrides will reorient in the direction which is perpendicular to the stress [10]. Fig. 2.3 shows the orientation of original and reoriented hydrides. The influence of tensile stress on hydride orientation can be explained by the effect of the tensile stress on the interaction energy of hydride [64]. The presence of tensile stress increases the negative interaction energy of radial hydride. At the same time, the positive interaction energy of circumferentially hydride will also be increased as the stress increases. This results in higher formation probability of radial hydrides when the tensile hoop stress is applied on the cladding [64]. It is widely known that the reoriented hydride (radial hydride in the cladding) will significantly decreases the ductility of cladding material, which posts a potential risk to cladding during service and post-use storage. An early study demonstrated that as little as 40 wppm hydrogen in Zircaloy could produce complete brittle behavior if most of hydride oriented perpendicular to the tensile stress [65]. During the service of zirconium based cladding in LWRs, hydride reorientation is one of the important factors that causes hydrogen embrittlement [66]. It was also reported that, during reactivity initiated accident (RIA) in BWRs the pellet-cracking mechanical interaction (PCMI) can lead to catastrophic cladding failure in axial direction of cladding, if associated with formation of 20% to 30% radial hydride and irradiation hardening effect [67]. Moreover,

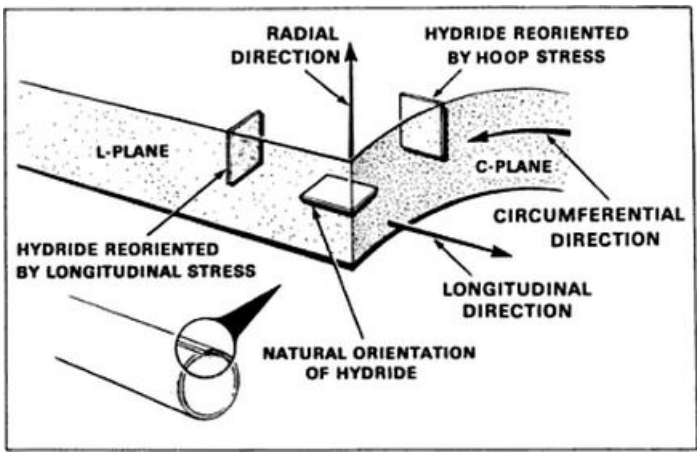

Figure 2.3: Schematic of orientation of original and reoriented hydrides. The stress is applied in hoop direction. Note that hydride plates will preferentially oriented perpendicularly to the stress direction [10].

reoriented hydrides assist the crack growth rate of DHC in UNF while being stored in pools and the dry casks. A recent study also demonstrated that the formation of radial hydride in a stress-relieved Zry-4 cladding decreases the fracture toughness of the material, which makes crack propagate more easily [68].

In order to understand the process of DHC, it is important to learn and review literatures which are relevant to the stress-induced hydride reorientation with the relevant on service or post-use storage thermal-mechanical conditions. The property and behavior of zirconium based matrix and hydride phase under these conditions will be learned. The effect of temperature, hydride density (with blister/rim structure or uniformly distributed hydride) on stress-induced hydride reorientation in zirconium based alloys and their criteria will also be reviewed.

2.3.1 Factors affect hydride stress-reorientation

Early studies focused on factors which affected hydride orientation and sensitivity of hydride orientation to the stress. Louthan and Marshall [65] first observed hydrides preferentially precipitated perpendicular to the tensile stress and parallel to the compressive stress in Zircaloys. The observation also indicated that the orientation of hydride was highly dependent on the fabrication history of Zircaloy tubes. Hydride in extruded and drawn tubes was very susceptible to stress orientation, where stress caused preferable orientation started being observed at ∼34 MPa and increased linearly with increased stress. On the other hand, no stress oriented hydride was observed in reduced tubes even when stressed at ∼150 MPa. This was further confirmed by Kearns and Woods [11] who studied the effect of matrix texture on hydride orientation in Zricaloy tubes and plates. Kearns and Woods concluded that the most desirable texture was the one which has the minimum circumferential basal pole intensity and the strongest radial basal pole intensity, since this texture will least likely to form radial hydride. The fabrication which caused high wall reduction (R_w) to diameter reduction (R_D) ratio generated this preferable texture. Experiment by Marshall [17] tested the influence of fabrication history on stress-oriented hydride in several Zircaloy tubes with different fabrication processes. In this test, three tubes were reduced to different R_w

to R_D ratio. The one which had highest R_w to R_D ratio was observed least susceptible to stress-induced reorientation; the tube which was as-extruded was most susceptible to stress-induced reorientation. Similar result was also reported by Hardie and Shanahan [69]; no appreciable hydride reorientation was observed by Hardie and Shanahan in the Zr-2.5%Nb plate which had strong circumferentially zirconium basal pole when being stressed up to 240 MPa. These observations further supported the previous presumption. It is worth noting here that the preferable fabrication process has direct connection with Trex and Supertrex treatment, which have been discussed in Section 2.1.1.

The effect of matrix grain size on the susceptibility of stress-induced hydride reorientation was studied by Kearns and Woods [11]. Kearns and Woods calculated the maximum reoriented hydride fraction with different grain sizes based on the experimental observation by the following equation [11]:

$$\triangle\% = 100V[\frac{2.1 \times 10^4 t}{DC} - 1] \tag{2.9}$$

where $\triangle\%$ is the maximum reoriented hydride fraction, V is the matrix grain with hydride habit planes tilted 60° to 90° to the stress axis (regard as oriented hydride), D is the average diameter of grains and C is the average hydrogen content. Fig. 2.4 shows the plot of Eq. (2.9) compared with the experimental data. The concept behind is that hydride preferentially precipitate at grains which have habit planes reoriented perpendicular to the stress axis. However, as the concentration of hydrogen in each grain decreases with increases grain size, hydrides are forced to accommodate more matrix grains which do not have favorable habit planes and reduce the fraction of reoriented hydride. Fig. 2.4 indicates that increases grain size will reduce the susceptibility of stress-induced reorientation in Zircaloy [11]. In contrast to Kearns and Woods, Leger and Donner [70] observed that increased grain size also increased the susceptibility of stress-induced reorientation in Zr-2.5%Nb tubes. However it needs to be noted that the grain size of Zr-2.5%Nb tubes (0.31 μm) in [70] is much smaller than grain size (>10 μm) of Zircaloy in [11].

The influence of matrix strength on hydride stress orientation was studied by Leger and Donner [70], where they observed the increased of threshold stress for hydride reorientation

in Zr-2.5%Nb and Zry-2 tubes as increased of matrix tensile strength. Leger and Donner concluded that during the tube fabrication the compressive residual stress was generated along the tube deformed direction and increased the hydride nucleation energy at the grains. The residual stress need to be eliminated by the applied stress before hydride can nucleate on these grains. Thus higher the residual stress was, higher applied stress was needed. The magnitude of the residual stress was unknown but should be related to the fabrication history and was proportional to the ultimate tensile strength of the matrix.

The hydrogen content in materials is expected to have effect on hydride reorientation behavior. Higher hydride concentration means less nucleation sites for radial hydride to precipitate and the probability of reorientation is then decreased. Kearns and Woods [11] studied the influence of grain size on hydride reorientation and came to a conclusion that higher hydrogen concentration needed to occupy more matrix grains when precipitated and was forced to precipitate on grains which have less favorable habit planes, thus decreased the fraction of radial hydride. Cladding tube deformation test (CTDT) experiment on fully recrystallized Zry-2 cladding tubes was tested by Alam and Hellwig [71] which supported the

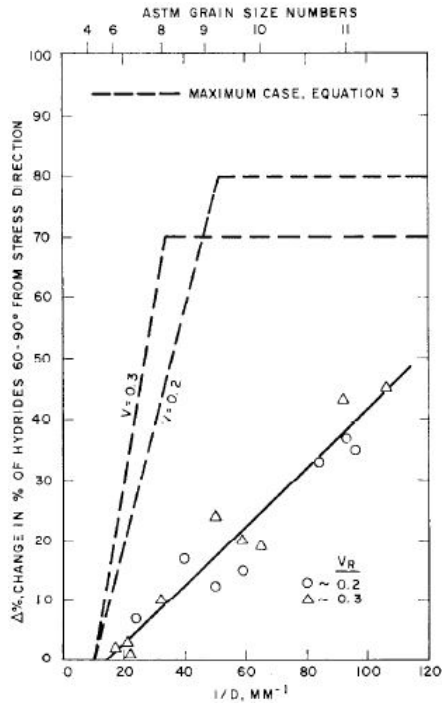

Figure 2.4: Model of the susceptibility of stress-induced hydride reorientation as the function of matrix grain size with the experimental data [11].

above assumption. The hydrogen content in this test varied from 250 wppm to 750 wppm. Samples were heated to 400 °C and slowly cooled down ($\sim$0.5 °C min^{-1}) to the RT. The threshold stress for hydride reorientation was observed between 65 MPa and 120 MPa and increased with increased hydrogen concentration. Similar result was also observed by Daum et al. [72], who performed the compression ring test (CRT) on irradiated and unirradiated CWSR Zry-4 tubes with temperature ranged from RT to 400 °C. For both irradiated and unirradiated tubes, more radial hydride fraction was observed on sample which had relative low hydrogen content ($\leq$350 wppm) and was more susceptible to hydride embrittlement. Samples which had higher hydrogen content had less radial hydride and higher ductility. Colas et al. [13] also suggested that there should be limited number of reorientation sites for hydride to precipitate; once these sites were filled , the circumferential hydride was then forced to form. Colas et al. observed a reduction of radial hydride fraction with increased hydrogen content in the temperature range which all hydride were dissolved before cooling. However, Sakamoto and Nakatsuka reported another result of recrystallized Zry-2 sheets [73] that the fraction of reoriented hydride was independent of hydrogen content within the measurement range of 61 to 668 wppm in the temperature range of 290 °C to 355 °C. The threshold stress they observed was 80 MPa. It should be noted that the effect of grain size should be taken into account. Later, Chu et al. [12] indicated that when discussed the effect of hydrogen content, the hysteresis behavior of TSS of hydrogen in zirconium should be considered as well. In Chu et al's test, the highest fraction of radial hydride in stress-relieved annealed (SRA) Zry-4 cladding tubes was observed for sample which had medium hydrogen content instead of the lowest. The explanation was if hydrogen content was lower than the certain level at the certain temperature, more supercooling was then needed to start nucleating the hydride. Fig. 2.5 shows the experiment data of Chu et al. [12], where the peak fraction of reoriented hydride was observed at $\sim$300 wppm. The concentration of hydrogen at peak reorientation fraction should vary with the tested temperature, since TSS of hydrogen in zirconium is the function of temperature as well. Chu et al's work also included the effect of thermal cycles, which will be discussed in more detail in the following paragraphs.

Effect of temperature on hydride orientation under stress can be expected to be related

to the matrix strength, since the strength of matrix decreased as the temperature increased. Bell and Duncan [74] reported that the threshold stress for hydride reorientation in Zr-2.5%Nb alloy should drop to zero when temperature was at 704 K. This was in contrast with the latter observation by Singh et al., [66], who observed no hydride reorientation in CWSR Zr-2.5%Nb tubes at 723 K with zero stress. Singh et al. explained that the difference could be caused by the different matrix material microstructure tested in two studies, or threshold stress might have non-linear relationship with the temperature. The non-linear relationship between the reorientation threshold stress and the temperature suggested by Singh et al. was [66]:

$$\sigma_{th} = 2.99 \times 10^4 - 160T + 0.29T^2 - 1.732T^3 \tag{2.10}$$

Instead of testing hydride reorientation at isothermal condition, Hong and Lee [75] tested CWSR Zry-4 cladding tube materials with three different cooling conditions which were 1) 400 °C to 300 °C, 2) 300 °C to 200 °C and 3) 200 °C to 100 °C at cooling rate of 4 $^{\circ}\mathrm{C\,min^{-1}}$ with the applied tensile stress of magnitude of 67.5% yield strength. Sample which has been cooled down from 300 °C to 200 °C was observed to have the highest fraction of radial hydride. The result was expected since the difference of hydrogen terminal solid

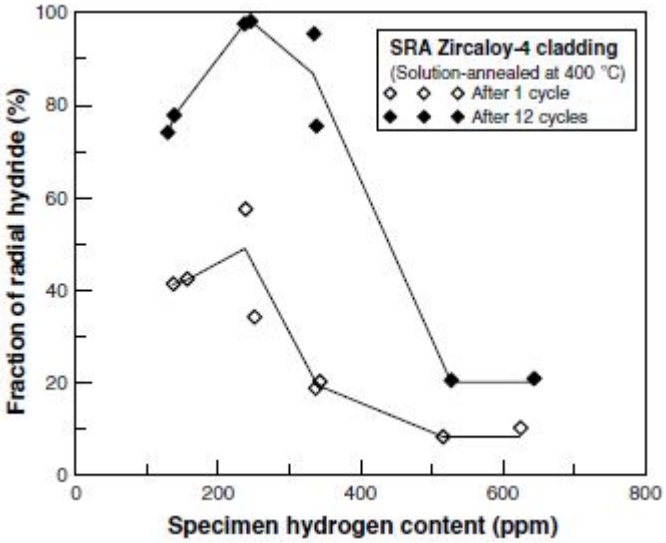

Figure 2.5: The effect of hydrogen content and thermal cycle on fraction of radial hydride [12]. Empty squares are experimental data after 1 thermal cycles, filled squares are experimental data after 12 thermal cycles.

solubility in zirconium is the largest between 300 °C and 200 °C compared with the other two, which mean that under this condition more hydride was dissolved and reprecipitated. Hong and Lee's [75] result supports the assumption by Ells [16], who emphasized that the hydride reorientation should be determined by nucleation orientation, but not by preferable orientation during the grain growth.

During the operation of nuclear reactors, cladding may encounter several thermal cycles due to change of fuels and minor accidents [76]. After being served in nuclear reactors, used nuclear fuels are first stored in fuel pool for certain number of years until heat decays to the regulated level. Before moved to the dry storage cask, the spent fuels are dried by applying several vacuum drying cycles (between 400 °C to RT) [13]. Due to the facts above, several studies focused on the effect of temperature cycles on stress-induced hydride reorientation [12, 13, 76]. The earliest study was done by Mishima and Okubo [76] on CWSR Zry-2 cladding tubes with temperature cycles between 300 °C and 100 °C at the cooling rate of 1.3 $^{\circ}\mathrm{C\,min^{-1}}$. This test demonstrated that the reorientation of hydride can happen at stress as low as 20 MPa when with the presence of temperature cycles. The fraction of radial hydride increased while the size of hydride particles decreased with increased number of cycle. However, Sakamoto and Nakatsuka [73] observed that the number of thermal cycles did not affect the threshold stress for reorientation but only affected the fraction of radial hydride on recrystallized Zry-2 sheet. Similar result was also observed by Chu et al. [12] on SRA Zry-4 cladding tubes with 160 MPa hoop stress, where increased number of thermal cycles increased the fraction of radial hydride. Most recent study on effect of thermal cycles

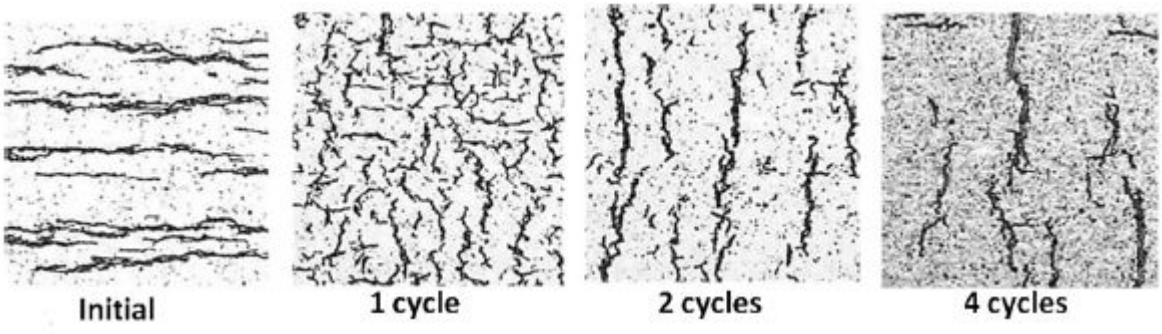

Figure 2.6: Optical metallographic result shows the evolution of the size and the connectivity of radial hydride with increases number of thermal-mechanical cycles [13].

was reported by Colas et al. [13] on CWSR Zry-4 sheets. In this study, temperature was cycled between 150 °C and 400 °C with heating rate of 25 °C min^{-1} and cooling rate of 1 °C min^{-1}. The tensile stress with magnitude of 240 MPa was applied in the transverse direction during the cooling. The full transformation from circumferential hydride to radial hydride only after two thermal-mechanical cycle was observed (with hydrogen content of 192 wppm). The size of radial hydride was observed to increase linearly with increased number of thermal-mechanical cycles, which made radial hydride become more connective; the result can be seen in Fig. 2.6. These connected radial hydride provided a continuous brittle path for crack propagating through the thickness of the cladding and eventually lead to the cladding failure.

The effect of irradiation on hydride reorientation was studied by Daum et al. [72] on CWSR Zry-4 cladding with the average burn up of 67 GWd/MTU and the maximum hydrogen content of 900 wppm. Ring compression tests on both irradiated and unirradiated tubes were conducted to generate hoop stress with range of 0 to 190 MPa at different temperatures. The σ_{th} was observed at 80 MPa for the unirradiated sample and 75 MPa for the irradiated sample. The irradiation did not affect the σ_{th} if the error was counted. However, the formation of the hydride rim structure on the irradiated sample increased the difficulty to resolve the radial hydride which increased the uncertainty of this study.

2.3.2 Application of synchrotron x-ray study on hydride reorientation

As aforementioned, synchrotron X-ray diffraction provides direct observation on minor hydride phase thus is a powerful tool to study hydride reorientation in zirconium based materials. The x-ray diffraction peak of hydrides can be fitted iteratively to obtain 1) integrated peak intensity, 2) the FWHM and 3) the shift of peak positions. These information can then be further interpreted to study the stress-induced hydride reorientation [14, 60].

Since hydride reorientation is highly related to the tensile hoop stress, it is also important to learn the mechanical response of the hydride phase compares with the zirconium matrix phase while external stress is applied. Kerr et al. [14] studied the strain evolution of hydride phase in warm-rolled Zry-2 plate by using synchrotron x-ray diffraction with *in-situ* tensile

testing; the tensile stress was applied in the transverse direction. The lattice strain of (111) hydride peak and the average of 5 zirconium peaks were then calculated after diffraction peaks were fitted. Three regimes were observed in hydride lattice strain evolution, which were 1) elastic response, 2) regime of load transfer and 3) regime of strain saturation. The load partitioning between the two phases and fracture of hydride were explained as reasons for transition from regime 1 to regime 2 and regime 2 to regime 3, respectively. The (111) hydride lattice strain evolution is shown in Fig. 2.7.

Colas et al. [60] studied the variation of FWHM of δ (111) hydride peak in the warm-rolled fully recrystallized Zry-2 bar and the CWSR Zry-4 sheet with the *in-situ* tensile test. The hydride reorientation and the reorientation threshold stress ($\sigma_{threshold}$) was determined by optical metallography method. $\sigma_{threshold}$ was found lower than 75 MPa for Zry-2 and ~80 MPa for Zry-4. Colas et al. observed the increased of FWHM in the direction where hydride plane oriented perpendicular to the stress (rolling direction in this case), while in other direction where hydride plane oriented parallel to the stress (transverse direction), the FWHM remained as a constant. The peak broadening effect was a result of strain broadening, where the strain originated from the growth of the reoriented hydrides. Another

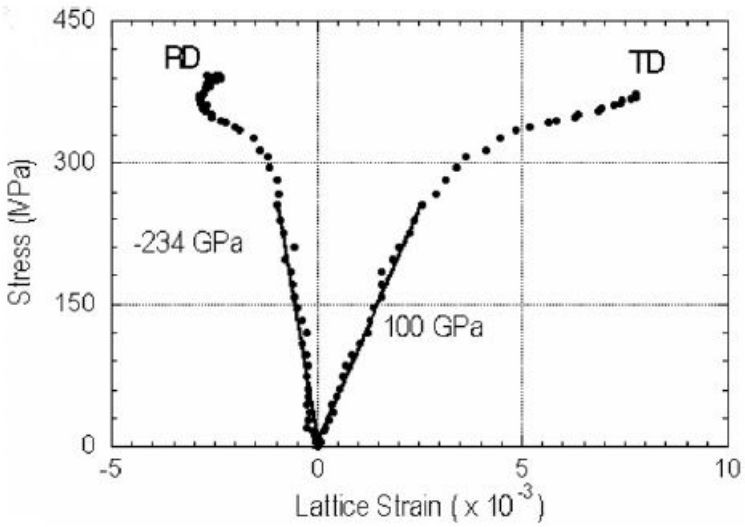

Figure 2.7: Lattice strain evolution of (111) hydride phase in transverse direction (TD) and rolling direction (RD) [14]. Three different regime with different slopes were identified. Elastic modulus of the (111) hydride was measured by linear fitting in regime 1 and is similar to the elastic modulus of zirconium.

different diffraction signature for δ (111) hydride FWHM variation during reorientation was observed by Colas et al. [13], who did thermal-mechanical cycles on CWSR Zry-4 sheets with 230 MPa tensile stress applied in the transverse direction during the cooling. The FWHM in both rolling and transverse direction was observed first decreased due to a fact that a single population of reoriented radial hydride was formed. After all hydride precipitated, the FWHM in TD (direction which was parallel to the stress) then slightly increased, and FWHM in RD (direction which was perpendicular to the stress) remained as a constant. This observation confirmed the diffraction signature which reported earlier by Colas et al. [60]. The signature was only observed in the first thermal-mechanical cycle, since after the second cycle all circumferential hydrides were reoriented to radial hydride.

Alvarez et al. [15] studied the stress status and reorientation of hydride particles in Zr-2.5%Nb pressure tube and suggested another hydride reorientation diffraction-based signature which may imply the hydride reorientation. During the hydride precipitation, compressive stress was generated from to volume difference between the hydride and the matrix phase. The volume difference can be as large as 17% for δ hydride [30]. Fig. 2.8 represents the different effect of compressive stress on circumferential and radial hydride which is proposed by Alvarez et al. [15]. The interplanar spacings (d) of hydride phase are expected to

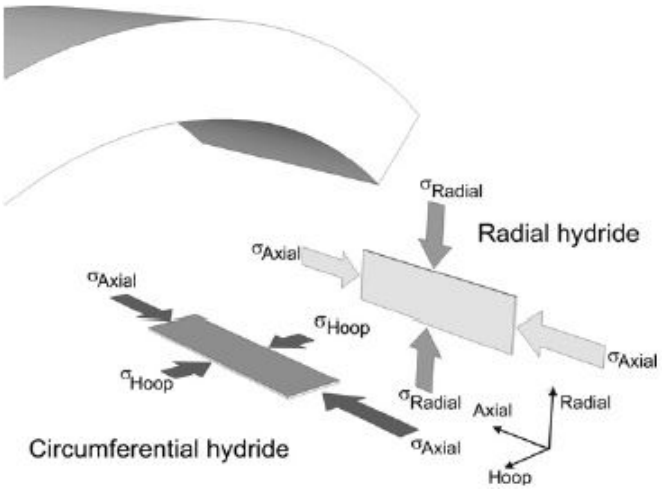

Figure 2.8: Schematic shows the effect of compressive stress on circumferential and radial hydride [15]. The compressive stress increases the interplanar spacing of planes which are parallel to the stress direction, and reduces the interplanar spacing of planes which are perpendicular to the stress direction due to Poisson's effect.

increase for hydride planes which are parallel to the compressive stress, and decrease for hydride planes which are perpendicular to the compressive stress. From Fig. 2.8, it is expected that for circumferential hydride the $d_{Radial} > d_{Hoop}$, and $d_{Radial} < d_{Hoop}$ for radial hydride. However the assumption has not been confirmed in this experiment. The proposed geometry is not convenient for measurement since normally for x-ray diffraction test the radial plane would be the plane which has its normal parallel to the x-ray direction, and will not generate any diffraction signal.

2.3.3 Modelling stress-oriented hydride in zirconium based alloys

The first stress-induced reorientation model of hydride in zirconium based alloys was formulated by Ells [16] by applying d Li's [77] stress orientation theory on disc shaped precipitation. The model starts from the expression of free energy of hydride nuclei and its relationship with the nucleation frequency, bases on the assumption that the number of hydrides grow to the experimentally observable size is directly proportional to the number of formed stable nuclei. The fraction of reoriented hydrides then can be calculated and was observed vary exponentially with the applied stress in a relation of [16]:

$$R_\sigma = R_0 \exp(\frac{V_c \delta \sigma w}{kT}) \tag{2.11}$$

The detailed derivation of Eq.2.11 is in [16] and its Appendix A. Here V_c is the volume of the hydride nucleus, δ is the lattice strain due to hydride formation in applied stress direction, k is the Boltzmann's constant and T is the temperature. w is related to the angle between applied stress axis and the normal direction of hydride planes. w can be also written as $\cos\theta^2$ [73], where θ is the angle between the stress direction and normal direction of hydride planes ($w \longrightarrow 0$ when $\theta \longrightarrow 90°$). w in Eq.2.11 includes the strong effect of crystallographic texture. Finally R_σ is the ratio between the number of reoriented and non-reoriented hydrides, and will be used to calculate F_x, which is the percentage of

hydride which has certain angle (x°) to the stress direction [16]:

$$F_x = 100\frac{R_\sigma}{1+R_\sigma} \tag{2.12}$$

The comparison of calculated result with the experimental data by Marshall [17] is shown in Fig. 2.9 [16]. Eq. (2.11) is in good agreement with the two sets of data from two different tubes with different fabrication history. It can be seen that in Ell's equation neither the effect of matrix texture nor the effect of the threshold stress has not been considered. The equation was then further modified by Sakamoto and Nakatsuka [73]. The modification bases on the experimental data from the study of stress-induced reorientation of hydride in recrystallized Zry-2 sheets under various conditions (texture, temperature, thermal cycling and hydride morphology). Additional parameters were introduced in modified Ells's equation [73]:

$$R = R_0 + \alpha exp(\beta(\sigma - \sigma_{th})\cos\theta^2) \tag{2.13}$$

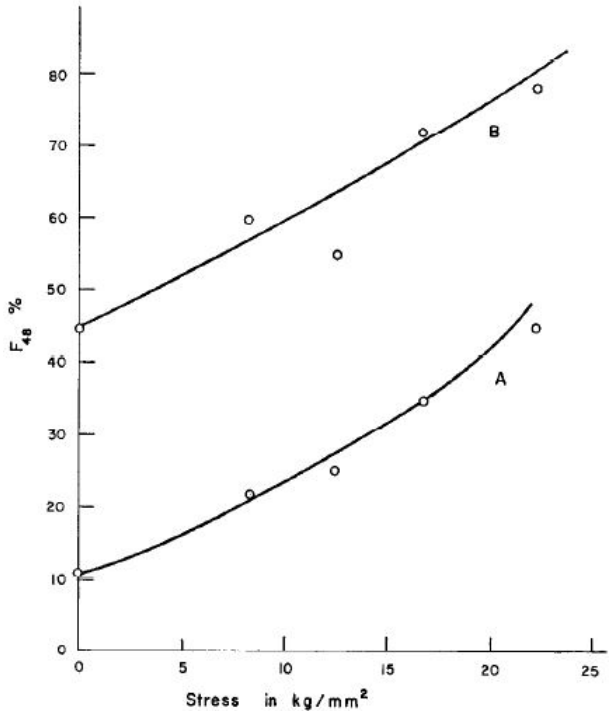

Figure 2.9: Percentage of reoriented hydride in Zircaloy. The solid line is calculated from Eq. (2.11) [16] and is compared with the experimental data which is reported by Marshall [17]. A and B are different tubes which are designed in [17]; A has higher R_w to R_D ratio.

where R_0, β and α are constants. σ_{th} is the threshold stress for hydride reorientation. The deformation of Zircaloy matrix prior to hydriding also has effect on hydride orientation; in general hydride plates precipitates parallel to the Zircaloy metal flowed direction during deformation. Different from the above model, Bai et al. [78] applied the critical nucleation energy of hydride. Bai et al.'s model was later modified by Chu et al. [12] by using Pul's [79] thermodynamic model on the critical nucleation energy of hydride while stressed externally. A model of radial hydride fraction which also has exponential behavior with the magnitude of the external stress is then developed:

$$n = \frac{1}{1 + 49exp(-\frac{Bv_0^*\sigma}{kT})} \tag{2.14}$$

where n is the percentage of radial hydride, v_0^* is the critical volume of hydride nucleus, B is the constant and σ is the external hoop stress (positive when tensile). The experimental results are in good agreement with the model of Bai et al.. The hydride reorientation σ_{th} for recrystallized Zry-4 bar at 400°C was observed and calculated at ∼95 MPa. The most recent model of stress-induced hydride reorientation was proposed by Massih and Jernkvist [80], who developed a model for precipitation orientation of plate-shape second phase particle in metal under stressed. The model was based on kinetics diffusion theory and classic nucleation theory, and can be used to compute the fraction of reorientation as the function of applied stress, temperature and time. However, the comparison between the experimental result and this model has not been made.

CHAPTER 3

EXPERIMENTAL PROCEDURES

3.1 Material

A Zry-4 sheet was obtained from ATI Specialty Alloys and Components with 25.4 mm for the width, 101.6 mm for the length and 1.5 mm for the thickness. The chemical composition of this material is very similar to ASTM Standards B353-12 [1] for fuel cladding material (UNS R60804) which is summarized in Table 1.1. Basal pole figure analysis was performed to identify the orientation of this material, where basal poles are expected to align perpendicular to the rolling direction. After the orientation was identified, four typical dog-bone tensile specimens were machined from the Zry-4 sheet by using electric discharge machining (EDM) to avoid generating residual stress in the samples. Fig. 3.1 shows the typical basal pole figure and the corresponding direction to dog-bone specimens. The (002) zirconium basal pole figure in Fig. 3.1 is a typical basal pole figure for CWSR Zry-4 plate, where zero intensity is observed in the RD and two poles are tilted ±30 to ±40 degree from the ND [24,34]. Dog-bone specimens were machined with the gauge length parallel to the RD and perpendicular to the TD from the Zry-4 sheet (the initial design is to machine tensile specimens which can be pulled along the TD, since the TD in the plate sample corresponds to the hoop direction in the tube samples. However, the pole figure analysis software has different zero angle reference than the X-ray instrument, which results in misinterpretation of the sample orientation. This issue was not resolved until the whole experiment was done, so in this work all samples were pulled along the RD). An isosceles triangle notch was machined on the surface of the gauge part with 500 μm for two sides of the notch and 250 μm for the bottom on one of the samples. Four samples were then labeled as Zry4_24 to Zry4_27 and loaded with different hydrogen content. Samples characteristic are briefly summarized in

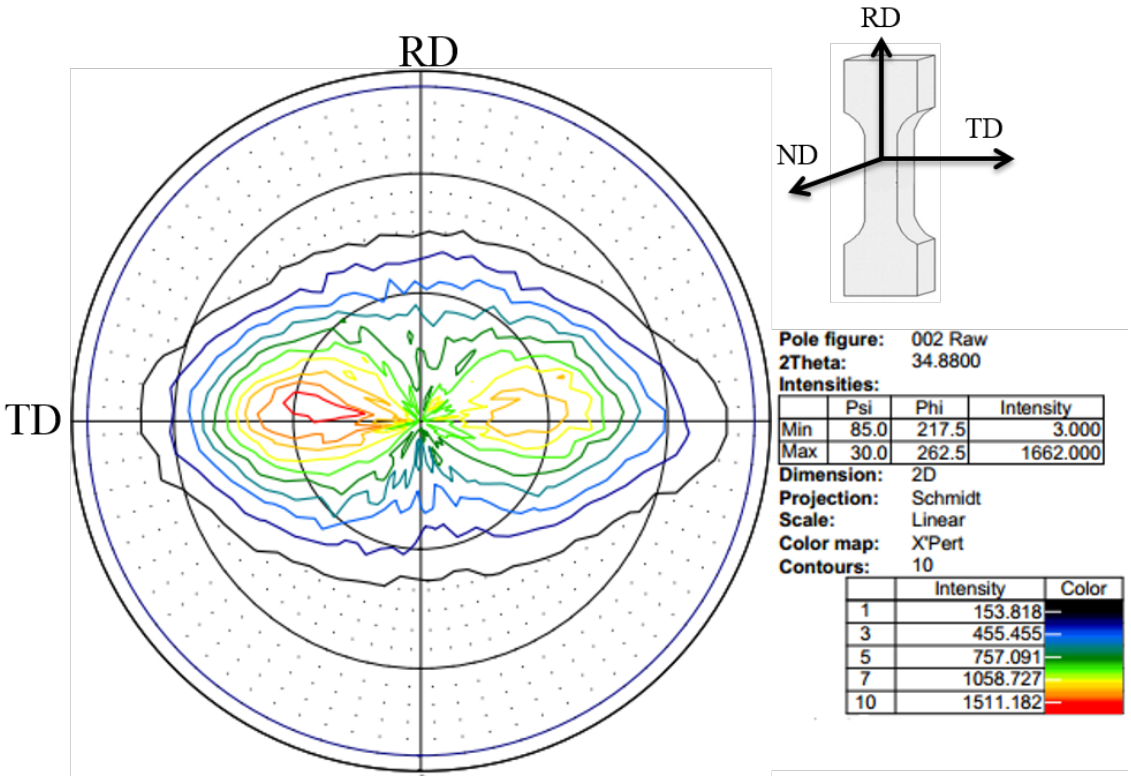

Figure 3.1: Basal pole figure for the Zry-4 plate used in this study (S25). RD = rolling direction and TD = transverse direction. The normal direction is perpendicular to the page. The dog-bone specimens were machined with the RD parallel to the gauge length.

Table 3.1. The hydrogen loading procedures will be discussed in the following section.

Table 3.1: Summary of specimen characteristics.

Label	**hydrogen content (wppm)**	**Mass (g)**
0††	0	0.98
24	492*	1.715
25	977	1.519
26†	492*	1.669
27	98	1.7351

All material used in this study are CWSR Zircaloy-4 plate.
*Specimen 24 and 26 were hydrided simultaneously.
†Specimen 26 has notch near the surface of the gauge length.
††Speciemn 0 is a small square shape sample used as a non-hydrided reference.

3.2 Hydrogen loading

The object of loading technique conducted here is to intentionally create a hydride blster/rim structure. The hydride blster/rim structure is a layer with high density of hydride formed near the surface of specimens. Hydride blister/rim structure is commonly observed on fuel cladding after being used in service in nuclear reactors, which is caused by a temperature gradient between the water side and the fuel side of the cladding [24]. In order to produce hydride blister/rim structure a thin Ni layer ($\sim$0.2μm) was coated on one surface of tensile specimens with sputter coating system [81]. Samples were carefully polished before the coating to a provide smooth surface for Ni adhesion. Polishing procedures started with 600 paper until samples were smooth, then 9µm diamond solution, 3µm diamond solution and 0.05 µm Syton® HT-50 silicon dioxide solution were used. Hydrogen charging was then performed by using Sievert-type apparatus gas loading system [82] at 400°C. The 2-D diagram of the system is shown in Fig. 3.2. Hydrogen loading was performed under a base vacuum of 10^{-8} torr to minimize the formation of oxide and nitride in specimens; the vacuum was achieved by operating a mechanical and a tubo pump simultaneously for over 12 hours. During the loading, hydrogen was slowly induced into the system but was isolated from the sample (see Fig. 3.2 while valve 2 and valve 3 were closed) until desired amount of pressure was achieved.

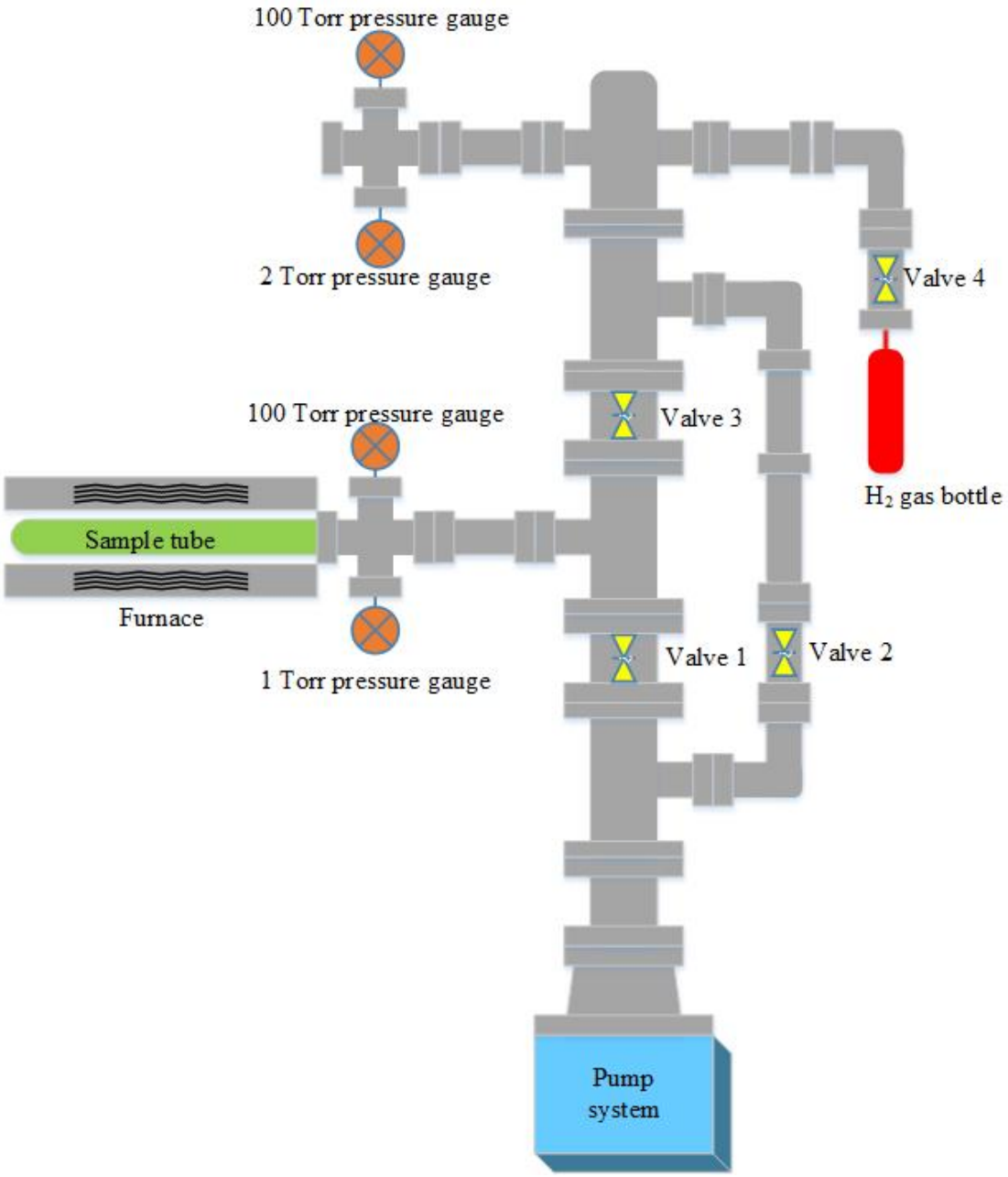

Figure 3.2: 2-D schematic of Sievert-type apparatus gas charging system which was used in this study.

It should be noted here that the hydrogen partial pressure dropped quickly in the first few seconds after the sample was exposed to the hydrogen, and was difficult to record. In order to solve this issue, the volume of gas part of the system and the volume of sample part of the system were measured. The pressure ratio between the two volumes was calculated by using the ideal gas law. The initial hydrogen partial pressure (the hydrogen partial pressure before the sample was exposed) was calculated by using the pressure ratio based on the desired hydrogen concentration in each sample. After a quick drop the hydrogen partial pressure then slowly decreased until the equilibrium pressure at the loading temperature (400°C) was reached. Specimens were then slowly cooled down with rate of 1 $^{\circ}\mathrm{C\,min^{-1}}$ in the hydrogen atmosphere to avoid hydrogen escaping from the samples during the cooling. The charging was done in stress-free condition to avoid the formation of the radial hydride. The final hydrogen concentration was calculated by applying the ideal gas law:

$$n_{tot} = \frac{\delta P V}{RT} \tag{3.1}$$

where δP is the total change of hydrogen partial pressure, V is the total volume of the system and n_{tot} is the total mole of hydrogen in samples which was used to calculate the global hydrogen concentration in samples. Fig. 3.3 shows the result of hydrogen charging curve. The hydrogen partial pressure decreases exponentially with the charging time and slowly reaches the equilibrium pressure, which is ∼11 mtorr at 400 °C [83]. The effect of Ni layer on hydrogen transportation kinetics is also shown in Fig. 3.3, where the presence of Ni layer significantly enhanced the hydrogen charging kinetics. After the charging was performed, the Ni layer was then removed by using Syton® solution again to avoid hydrogen release. The hydride distribution was investigated by the optical metallography and conventional x-ray diffraction. In order to reveal the hydride, a sample was cut from the cross section surface and was etched for 1 minute by submerging in an acid solution which was composed of 45% deionized water, 45% nitric acid and 10% hydrofluoric acid (48% concentration). The optical result is shown in Fig. 3.4(a). The hydride blister/rim structure with the thickness of ∼20 µm to 150 µm (for hydrogen content ∼ 3000 wppm) was observed near the free surface. A hydride fraction was also observed to decrease from the surface to the center of

the specimens. Conventional x-ray diffraction test was performed on the surface plane and cross section plane of the sample by utilizing the Philips Xpert#2 XRD system with 0.154 nm Cu k-α x-ray. Fig. 3.4(b) shows a result of typical ω-2θ absolute scan on two planes. For cross section plane the zirconium phase was observed as the major phase. However, the minor hydride phase became dominant on surface plane, which indicated the presence of a hydride blister/rim structure near the sample surface.

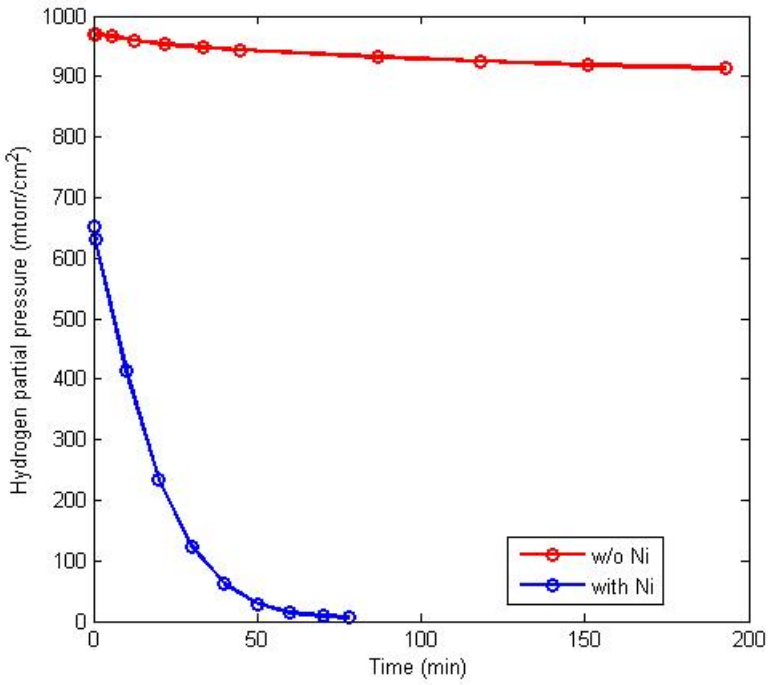

Figure 3.3: Hydrogen charging kinetics of samples 1) data without the Ni layer are shown as the red open circle and 2) data with Ni layer and are shown as blue open circle. It needs to be noted here that for sample without Ni the charing was performed at 500 °C, and for sample with Ni the charing was performed at 400 °C. The transportation rate of hydrogen for sample with a Ni layer is faster even at the lower temperature.

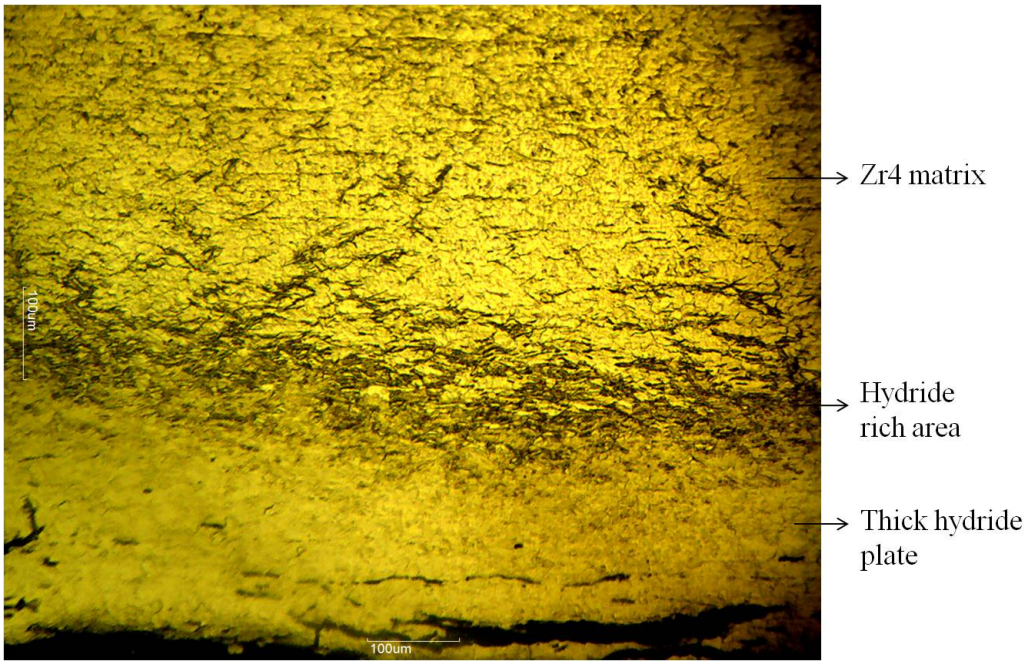

(a)

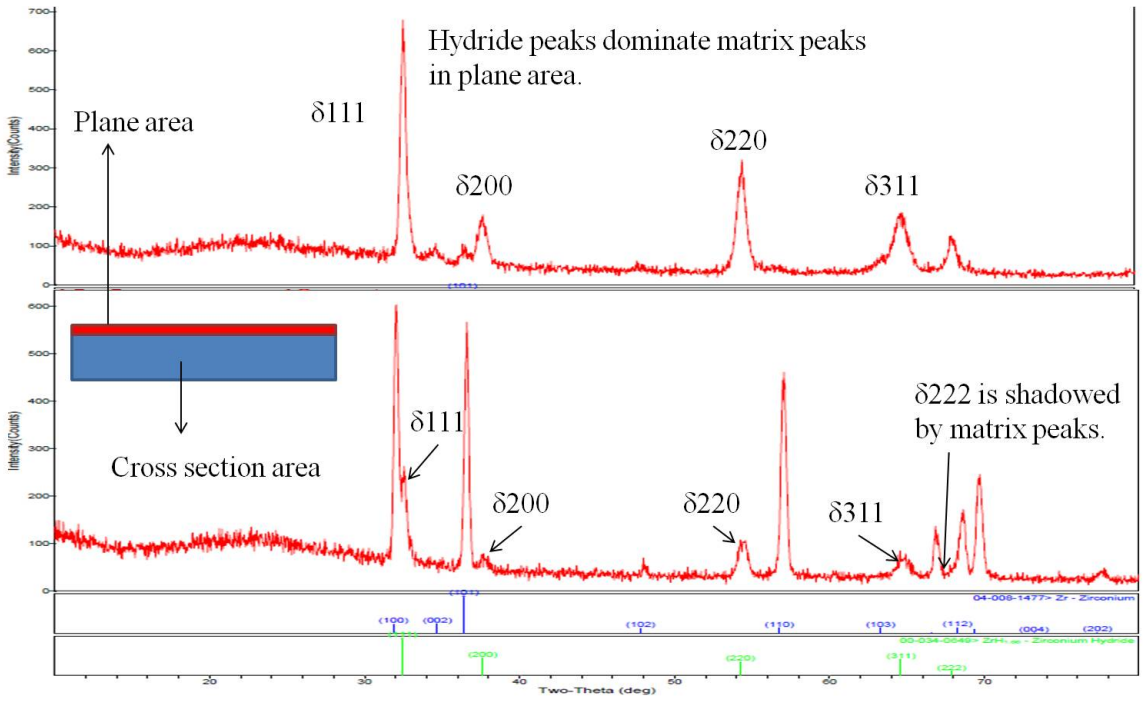

(b)

Figure 3.4: The observation of the hydride blister/rim structure by (a) The optical picture and (b) the x-ray diffraction scanned on cross section plane and surface plane of the specimen. Red layer indicated where the Ni was coated on.

3.3 High energy synchrotron x-ray diffraction

Synchrotron x-ray diffraction experiment was performed at 1-ID Beamline of Advanced Photon Source (APS) at Argonne National Laboratory (ANL) with the purpose to study the mechanical response of hydride phase with the blister/rim structure in CWSR Zry-4 sheet while the external tensile stress is applied. Fig. 3.5 indicates the location of the 1-ID Beamline at APS.

X-ray diffraction was conducted in transmission geometry with X-ray energy of 86 keV, wavelength of 0.144 Å and beam size of 150 µm × 150 µm. High resolution quad GE a-Si detectors (4 panels Hydra detector) with 2048 × 2048 pixels per detector. The MTS® load frame and clamp shell furnace was installed for the application of *in-situ* mechanical-thermal test. The high intensity x-ray source enables quantification of minor hydride phase in Zry-4 matrix under different applied stress and temperature. Because the diffraction data is obtained in transmission geometry, a full Debye-Scherrer ring is obtained. The information can be obtained by integrating the Debye-Scherrer ring over the specific angle which is related to the macroscopic orientation geometry of the sample to the detector. The test geometry of this study is illustrated in Fig. 3.6. Generally for uniaxial loading test, the most interesting angles are directions which are parallel (RD) and perpendicular (TD) to the stress direction. Since these two give information of the maximum effect of the load and the maximum Poisson effect due to the load.

For samples without a notch, the diffraction data was recorded by 1 successive scan with 10 seconds exposure. In order to study and also minimize the difference at different positions on the gauge length of the samples, 12 scans were taken in every measurement which is shown in Fig. 3.7(a). For the sample with a notch, 31 scans were taken in every measurement with 30 scans around the notch tip and 1 scan on location away from the notch to study the far field behavior. In this geometry, two spots hit the notch which will be taken out later (see Fig. 3.7(b)).

The *in-situ* mechanical-thermal procedures is summarized in Table 4.1 and is shown in Fig. 3.8. The MTS® load frame with the limitation of 10k Newton force and clamp shell furnace were used. A K-type thermal couple was mounted on the surface of the gauge length

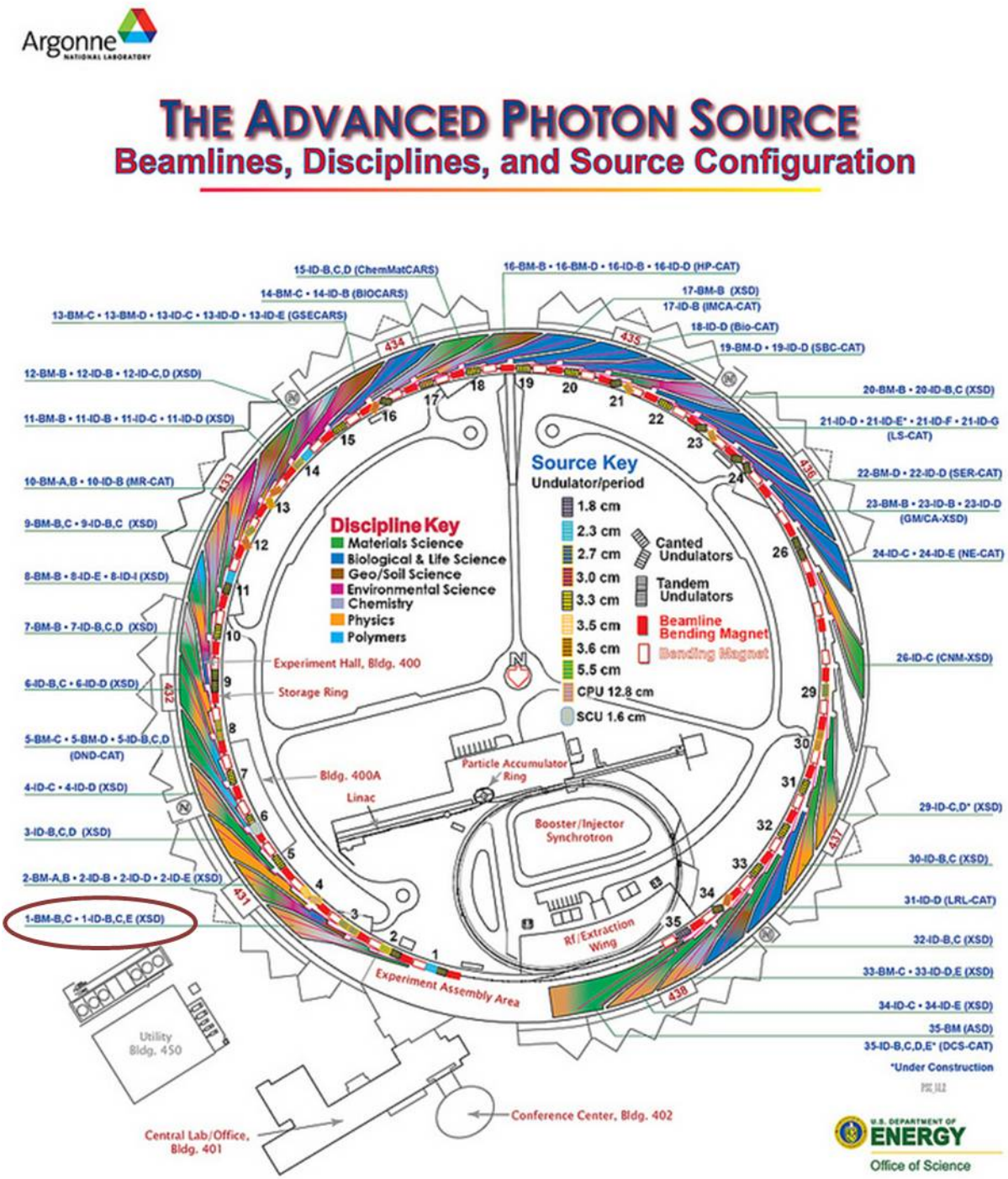

Figure 3.5: Schematic shows the location of 1-ID Beamline at Advanced Photon Source, which is circled by red ellipsoid (taken from courtesy of Argonne National Laboratory).

and was used as the control thermal couple. The control thermal couple was wrapped at the bottom of the gauge length to avoid interfering with the X-ray beam. Although a

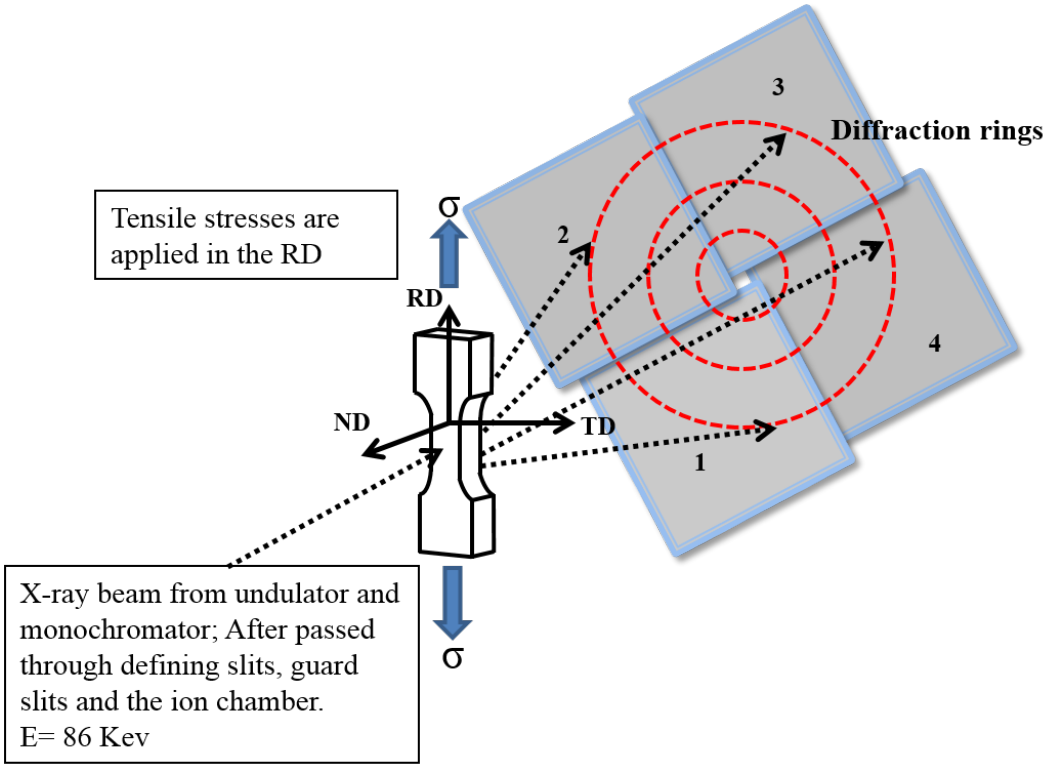

Figure 3.6: Schematic shows the experiment geometry.

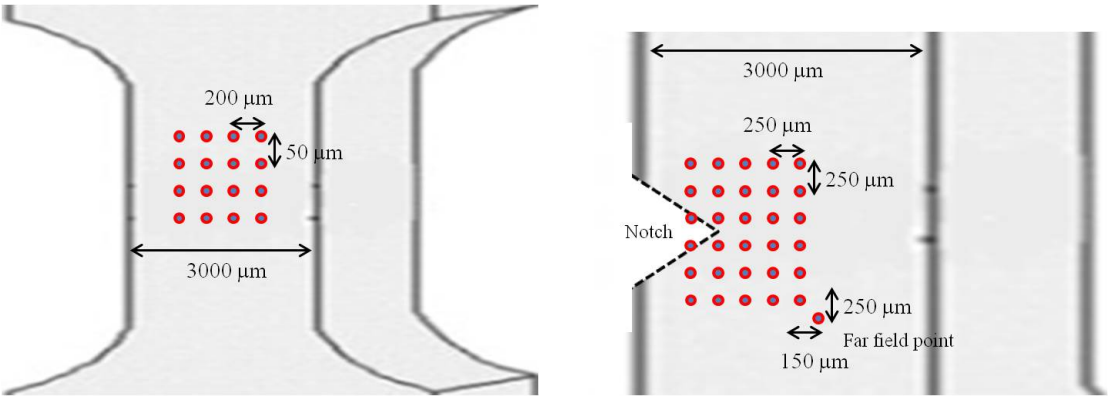

(a) Sample without the notch

(b) Sample with the notch

Figure 3.7: Schematic shows the measurement of x-ray on different spots on the gauge length of the dog-bone samples for every measurement.

temperature gradient between the thermal couple and the X-ray measured area existed, it was observed that the thermal gradient was not greater than 20°C at the testing temperature (200 °C). Samples were first measured at the room temperature with 10 N load. Samples were than heated to 200 °C with the load increased incrementally to 700 N, which generated

$\sim$ 200 MPa tensile stress on samples in this study (see Table 4.1 for the exact stress on each sample). Samples were than held at 200 °C) temperature and the maximum stress for 4 to 8 hours in order to simulate post-use storage environment.

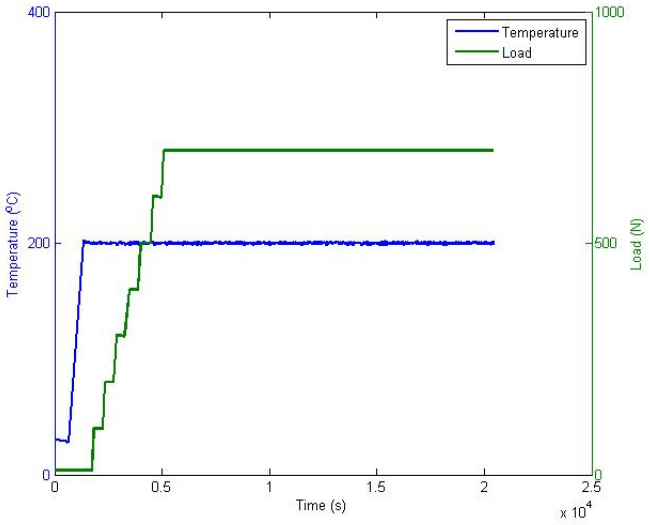

Figure 3.8: An example of *in-situ* mechanical-thermal test procedures for all samples in this study. Load was increased incrementally of 100 N for every step (held for 1 hour per step before increased to the next load). The temperature is held at 200 °C.

CHAPTER 4

RESULTS AND DISCUSSION

4.1 Hydride phase identification

Summary of the hydrogen content and the *in-situ* mechanical-thermal procedures for each sample is listed in Table 4.1. Raw X-ray diffraction data was analyzed by Matlab® routine [84], including the background substraction and diffraction ring integration. Since the data was recorded by four different panels, the analysis procedure was performed separately for each panel. The center of each panel was calibrated by using cerium oxide X-ray diffraction pattern with FIT2D 1 and 2 dimensional data analysis program [85]. The tilt angle of each panel was measured by an electronic goniometer. This information is required as input inro the Matlab® routine for correct analysis.

The first step was to identify the hydride and zirconium diffraction peaks with the assistance of powder diffraction (PDF) cards. Fig. 4.1(a) shows an example of the typical Debye-Sherrer ring of each panel for sample with 977 wppm hydrogen content; each panel shows only one quarter of the ring. Fig. 4.1(b) shows the transformed image of the ring

Table 4.1: Summary of thermal and mechanical treatment on different specimens.

Label	**hydrogen content (wppm)**	**Testing temperature (°C)**	**Stresses (MPa)**	**Holding time at σ_{max} (hr)**
0	0	25	None	None
24	492*	200	3 to 200	3.5
25	977	200	3 to 218	4.5
26†	492*	200	3 to 200	2.5
27	98	200	3 to 190	4

All material used in this study are CWSR Zircaloy-4 plate.
*Specimen 24 and 26 were hydrided simultaneously.
†Specimen 26 has notch near the surface of the gauge length.

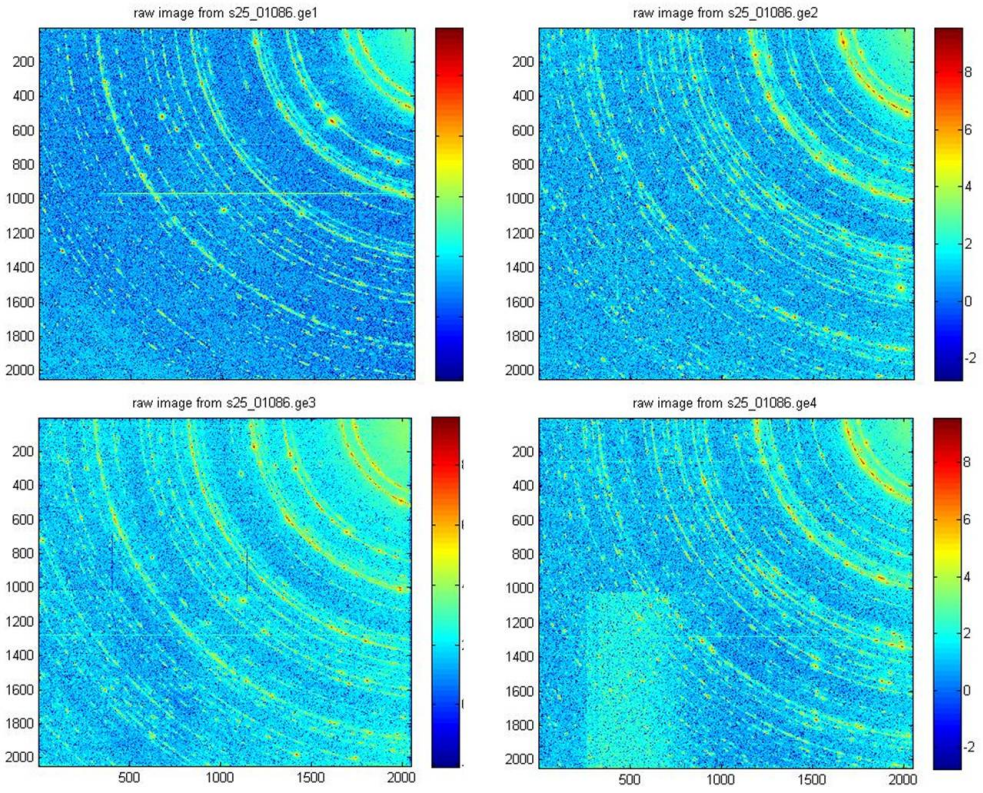

(a)

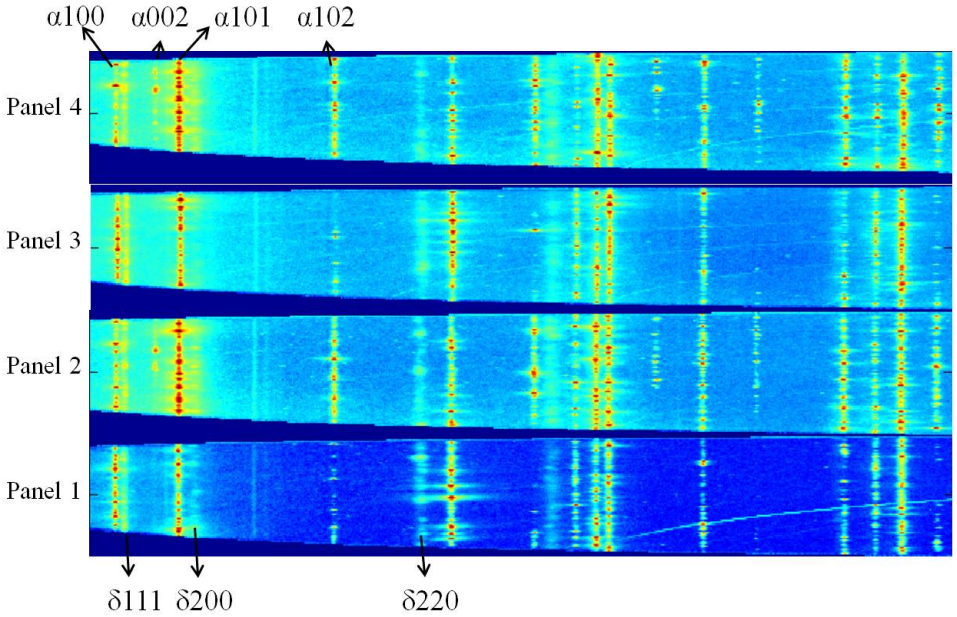

(b)

Figure 4.1: Typical diffraction pattern of (a) Dybe-Sherrer ring (b) transformed images of the ring for sample with hydrogen content of 977 wppm. The title (ge1 to ge4) indicates number of the panels from 1 to 4. Several α zirconium matrix and δ hydride peaks are identified in the transformed images.

in each panel. The highly textured characteristic of zirconium can be observed from the transformed images. Two common orientation relationships between the δ hydride and α zirconium phase can also be observed in Fig. 4.2, which are

$$(111)_\delta//(10\bar{1}0)_\alpha \text{ and } (111)_\delta//(0002)_\alpha$$

An example of the typical diffraction intensity versus d-spacing diagram for sample with 977 wppm hydrogen is generated by integrating over the entire Dybe-Sherrer ring, which is shown in Fig.4.3. Four δ zirconium hydride peaks ((111), (200), (220) and (311)) are clearly identified, where (111) reflection has the strongest intensity. Peaks of the second phase particles (SPPs) in Zry-4, which is also known as χ phase or hexagonal C14 laves phase [86] with the formula of Zr_2Fe_3Cr, are also revealed by the high energy synchrotron x-ray beam. The peak position of the χ phase observed in this study is in good agreement with an early observation by Erwin et al. [86]. For α zirconium phase the reflection of $(10\bar{1}1)$ pyramidal plane has the strongest diffraction intensity. Fig. 4.4 shows the comparison of intensity versus lattice spacing d among samples with different hydrogen content. For each diffraction

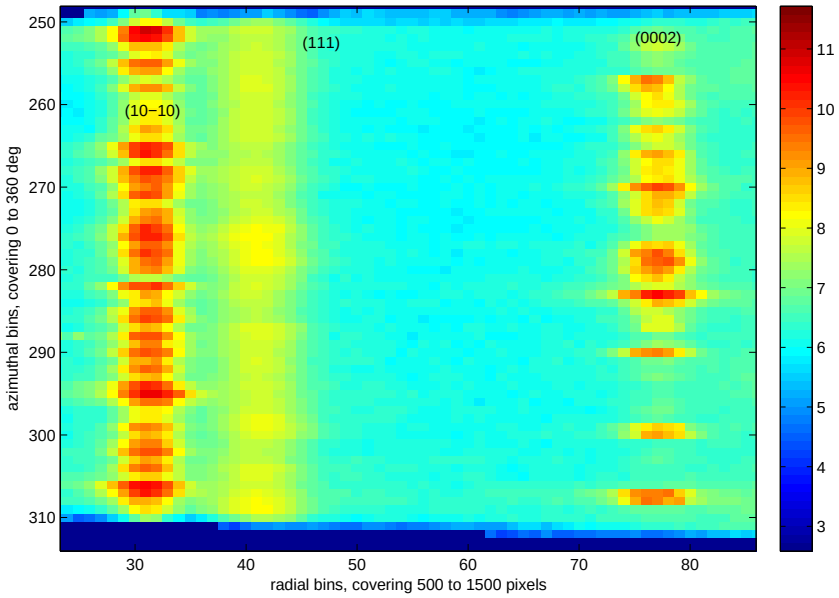

Figure 4.2: A zoom-in version of transformed X-ray images.

diagram the integrated intensity was normalized by the strongest zirconium peak (α (101)) to minimize the instrument and background influence. It is clear that the diffraction intensity of hydride peaks increase with increases hydrogen content in the samples.

The f.c.c δ is the only zirconium hydride phase observed in this study. The γ and ϵ phase were not observed in the range of hydrogen content (98-977 wppm) tested in this study. This observation is in contrast with some previous studies which the γ phase was observed in materials with hydrogen content as low as 230 wppm [30, 49], but is in good agreement with other studies that observed the δ hydride is the only dominant phase when material is cooled with rate less than 10 °C min^{-1} after loaded with hydrogen [44, 47].

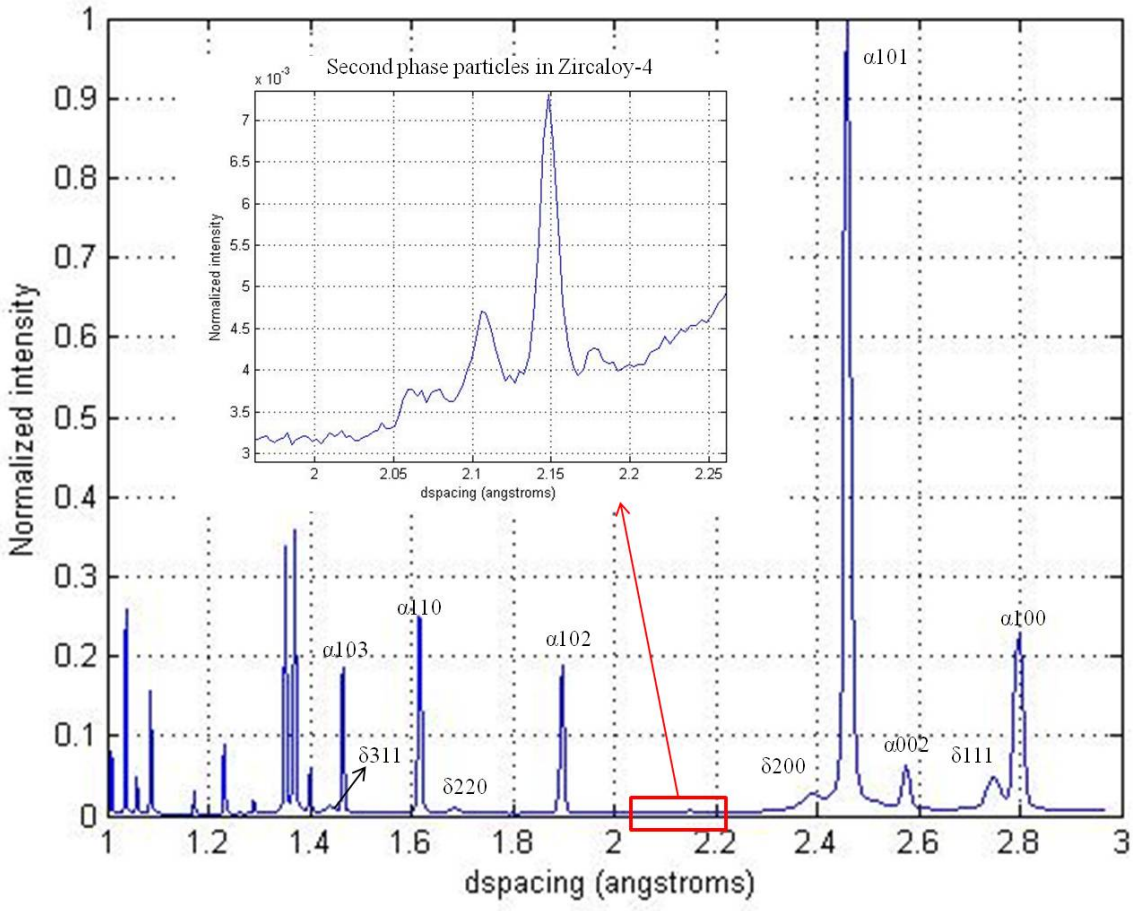

Figure 4.3: A diagram of the normalized intensity versus d-spacing for sample with 977 wppm hydrogen. The second phase particles (SPPs) were also revealed by the high energy X-ray beam, which was pointed out by the red rectangular.

Further analysis focused on peak characteristics such as the integrated intensity (peak area), FWHM and peak position. The shift of peak position is used to calculate the evolution of lattice strains while externally stressed [15]. The variation of FWHM indicates the presence of non-uniform strain which may be caused by the precipitation of new hydride plates [13, 60]. The integrated hydride peak intensity is used to study the dissolution and precipitation kinetics of the hydride phase, and the hydride reorientation behavior during the *in-situ* test. In this study, the single peak analysis is limited on four matrix peaks ((100),(101),(102) and (110)) and two hydride peaks ((111) and (220)). Strong texture characteristic of zirconium basal peak (002) makes it unsuitable for single peak analysis. Peaks with good statistics are preferable. For sample with low hydrogen concentration the fitting error is expected to be large. For some analysis result, the weak (220) hydride peak may be abandoned in the case of large fitting error.

The peak fitting was performed with Matlab® routine [84] after the intensity ring was integrated azimuthally over a specific range of angles. This study is interested in the peak variation in the RD and TD, which are parallel and perpendicular to the applied stress, respectively. The integration is performed in these directions with angles of 10° (±5°), as

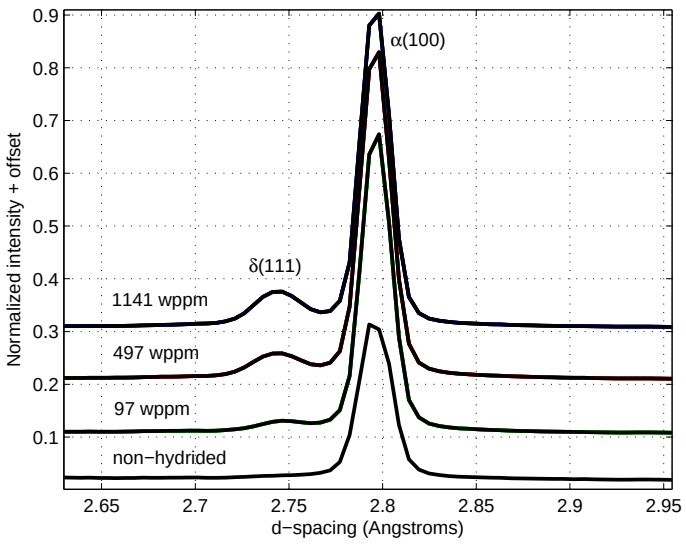

Figure 4.4: Comparison of diffraction diagram among samples with different hydrogen content. Intensities are normalized by (101) zirconium peak and separated by adding the offset. All the data shown here were recorded at RT.

schematically shown in Fig. 4.5. Peaks are fitted separately for each panel. Since the axis of each panel was tilted 62° from the level, the calibration on orientation of panels are needed before peak analysis. The calibration code is builded in Matlab® routine with the principal angle for each panel at 270°, i.e., 270° on panel 1 and panel 3 is along the RD but for panel 2 and panel 4 it is along the TD (see Fig. 4.5). Fig. 4.6(a) and Fig. 4.6(b) are examples of single peak fitting of two hydride peaks for sample with 977 wppm hydrogen. The peak profile used in this analysis is pseudo-voight function, which is a convolution of Gaussian and Lorentzian profile. The fitting results (peak position, intensity and FWHM) are output as text files for further analysis. The background is linearly fitted and subtracted each time before the fitting. The peak position and FWHM are first presented as radial position, which is the distance from the center of the detector to the outer boundary of the detector. The radial position can later be converted into the d-spacing or 2θ. The integrated peak intensity,

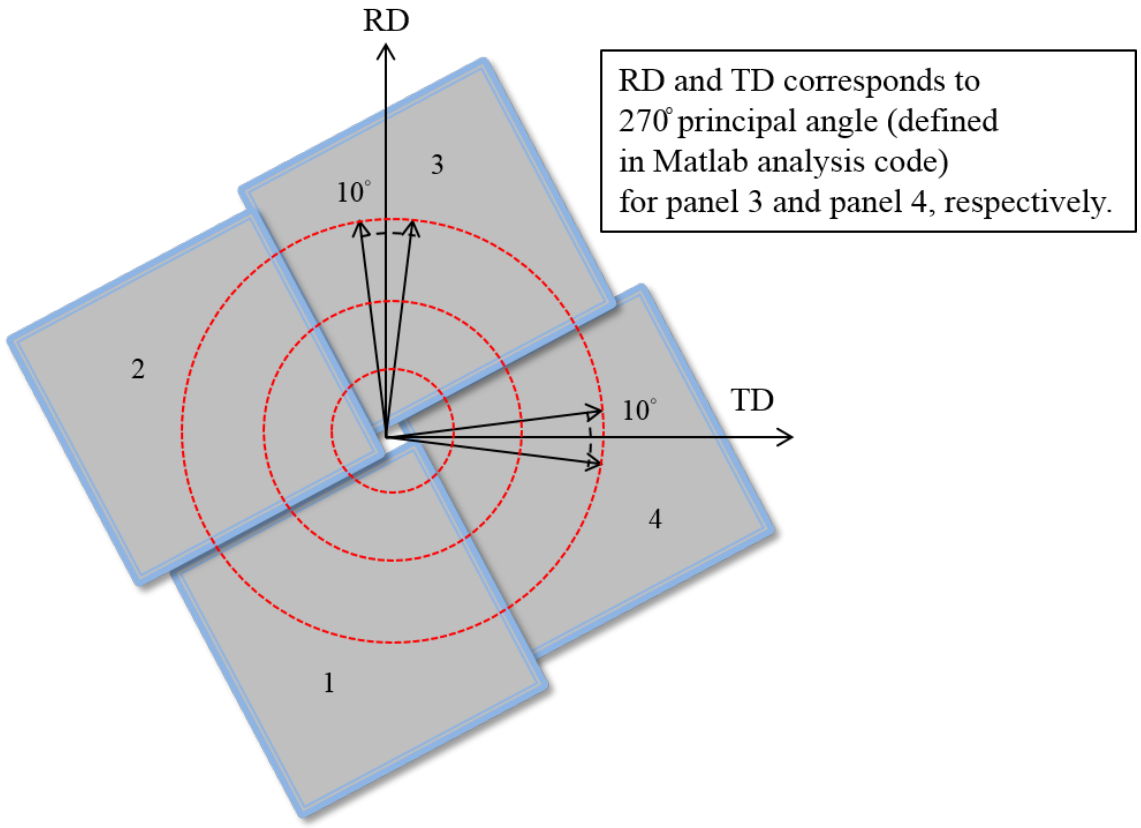

Figure 4.5: Schematic shows the integration direction on the Dybe-Sherrer ring performed in this study. Each panel is labeled with a number.

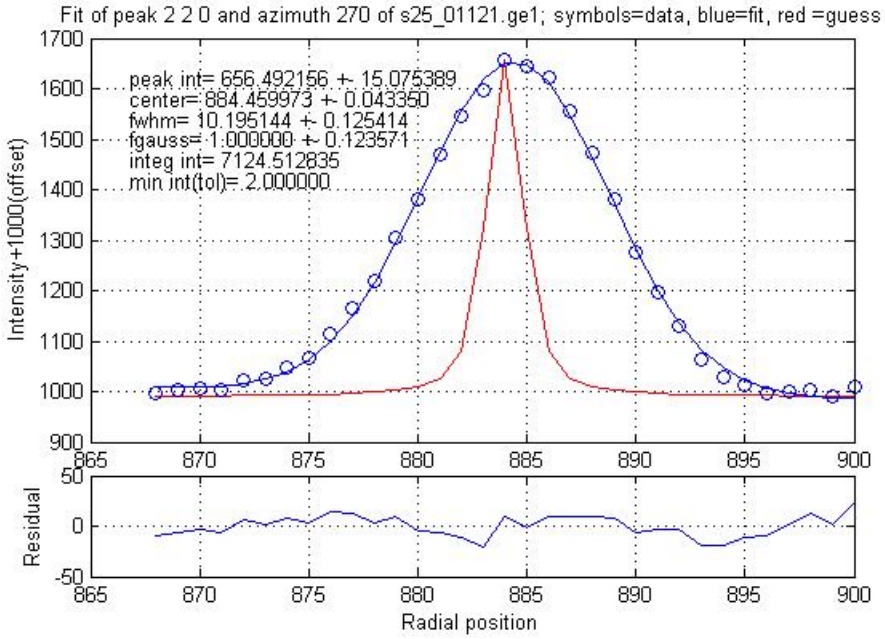

(a)

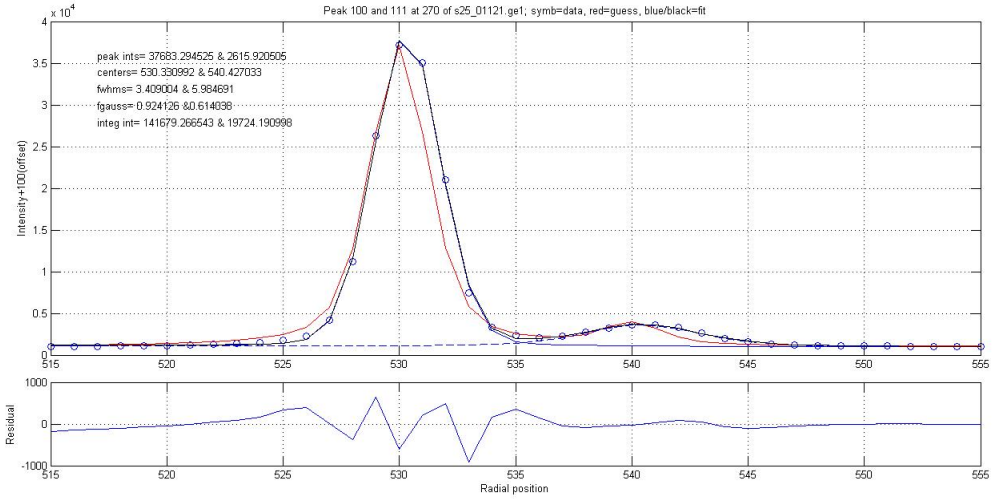

(b)

Figure 4.6: Peak fitting of two hydride peaks performed by Matlab® routine (a) δ (220) (b) δ (111) and α (100). Circles are data points, red line is the first guess and blue line is the fitting curve. For multiple peaks fitting, blue line is the fitting of each peaks and black line is the total fitting curve. Fitting result is listed on the upper left corner of each figure.

which is the area under the peak and above the background line, is a better way to represent the diffraction intensity of the phase than peak intensity. For most of the interested peaks in this study single peak fitting is enough to represent the peak profile. However, the δ hydride (111) peak is close to the α (100) zirconium peak which the peak profile was affected by the long tail of α (100) peak. Multiple-peak fitting was then performed to fit δ hydride (111) and α (100) zirconium peak simultaneously. Single peak fitting for zirconium matrix peaks was performed similarly as hydride peaks, and are not shown in here.

The peak fitting results of the four α zirconium peaks and two δ hydride peaks for four samples at RT are summarized in Table 4.2 (RD) and Table 4.3 (TD). Diffraction intensity of hydride phase increases with increases hydrogen content in samples. The diffraction intensity of each phase was represented by the normalized integrated intensity. It is worth noting here that for each peak the integrated intensity was normalized by the summation of every intensity recorded in the Debye Sherrer ring. The δ (111) phase is the strongest hydride peak in both the TD and RD. However, for matrix the strongest peak is α (101) in TD and can be α (101) or α (100) in RD. The range of the hydrogen content tested in this study has little effect on the d-spacing of the zirconium and zirconium hydride lattices. Similar results were also reported by Daum [87], who loaded hydrogen into a CWSR Zry-4 tube with hydrogen content range of 250 to 2950 wppm and observed the peak positions of zirconium matrix remained unchanged. As the hydrogen content increases, the more the lattice spacing of δ hydride phase decreases. However, this difference is also marginal and is within the error of fitting.

Table 4.2: Summary of peak fitting results in RD at RT.

Phase (hkl)	**Sample**	**D-spacing (Å)**	**FWHM (Radial spacing)**	**Normalized intensity ($\times 10^{-3}$)**
δ(111)	PDF (00-034-0649)	2.76	...	...
	98 wppm	2.7472	6.239	3.123
	492 wppm w/notch	2.7446	6.232	9.511
	492 wppm	2.7425	6.207	8.934
	977 wppm	2.7426	5.964	12.51
δ(220)	PDF (00-034-0649)	1.6903	...	...
	98 wppm	...	...	...
	492 wppm w/notch	1.6811	10.04	2.437
	492 wppm	1.68	10.791	2.906
	977 wppm	1.6803	10.46	5.359
α(100)	PDF (04-008-1477)	2.8077	...	...
	Non-hydrided	2.7944	3.504	68.51
	98 wppm	2.795	3.408	67.22
	492 wppm w/notch	2.7955	3.372	85.58
	492 wppm	2.7947	3.378	69.85
	977 wppm	2.7945	3.379	89.78
α(101)	PDF (04-008-1477)	2.4672	...	...
	Non-hydrided	2.4565	3.711	51.72
	98 wppm	2.458	3.585	84.77
	492 wppm w/notch	2.4581	3.527	79.47
	492 wppm	2.4571	3.51	92.35
	977 wppm	2.457	3.427	83.10
α(102)	PDF (04-008-1477)	1.9015	...	...
	Non-hydrided	1.8954	3.592	8.649
	98 wppm	1.8959	3.087	0.939
	492 wppm w/notch	1.8958	3.22	2.110
	492 wppm	1.896	3.73	2.224
	977 wppm	1.8957	3.45	4.407
α(110)	PDF (04-008-1477)	1.621	...	...
	Non-hydrided	1.615	3.922	41.97
	98 wppm	1.616	3.668	74.50
	492 wppm w/notch	1.6164	3.873	87.67
	492 wppm	1.6158	3.784	66.06
	977 wppm	1.6159	3.827	89.33

Peak δ (220) is not observed in sample with 98 wppm hydrogen content due to the low concentration.

Table 4.3: Summary of peak fitting results in TD at RT.

Phase (hkl)	**Sample**	**D-spacing (Å)**	**FWHM (Radial spacing)**	**Normalized intensity ($\times 10^{-3}$)**
δ(111)	PDF (00-034-0649)	2.76	...	...
	98 Wppm	2.7457	5.656	2.038
	492 Wppm w/notch	2.7442	6	6.892
	492 Wppm	2.7444	6.141	6.231
	977 Wppm	2.7445	6.17	9.976
δ(220)	PDF (00-034-0649)	1.6903	...	...
	98 Wppm	...	...	...
	492 Wppm w/notch	1.6833	8.602	0.894
	492 Wppm	1.6828	9.494	1.602
	977 Wppm	1.6825	9.041	1.282
α(100)	PDF (04-008-1477)	2.8077	...	
	Non-hydrided	2.7938	3.564	10.19
	98 Wppm	2.7934	3.475	16.60
	492 Wppm w/notch	2.7937	3.343	24.30
	492 Wppm	2.7937	3.405	26.57
	977 Wppm	2.7938	3.417	34.39
α(101)	PDF (04-008-1477)	2.4672	...	...
	Non-hydrided	2.4568	3.574	103.9
	98 Wppm	2.4564	3.496	103.5
	492 Wppm w/notch	2.4564	3.479	120.0
	492 Wppm	2.4561	3.54	116.9
	977 Wppm	2.4562	3.556	133.7
α(102)	PDF (04-008-1477)	1.9015	...	...
	Non-hydrided	1.8953	3.994	6.802
	98 Wppm	1.8949	3.495	19.03
	492 Wppm w/notch	1.8949	3.457	22.21
	492 Wppm	1.8948	3.407	17.90
	977 Wppm	1.8947	3.491	22.35
α(110)	PDF (04-008-1477)	1.621	...	...
	Non-hydrided	1.6152	3.81	33.41
	98 Wppm	1.6153	3.52	16.02
	492 Wppm w/notch	1.6155	3.834	27.23
	492 Wppm	1.6153	3.849	30.05
	977 Wppm	1.6151	3.85	19.41

Hydride peak δ (220) is not observed in sample with 98 Wppm hydrogen content due to low hydrogen concentration.

4.2 Evolution of lattice strain as the function of the applied tensile stress

The lattice strain of the hydride and matrix peaks are calculated based on the shift of peaks while external tensile stress is applied. Fig. 4.7(a) and Fig. 4.7(b) show examples of the change of d-spacings of δ (111) and (220) hydride for sample with 977 wppm hydrogen content during the tensile test. The room temperature data is excluded in these figures; all data were recorded at 200 °C. Notice that δ (220) has smaller fitting error than δ (111) even though the diffraction intensity is weaker for (220) reflection. This indicates that multiple peak fitting generates larger fitting error than single peak fitting. For both δ (111) and δ (220) peaks, initial d-spacings in the RD (or transverse-normal plane of the sample) is less than d-spacing in the TD (or rolling-normal plane). This indicates that the initial stress on the hydride is higher in the RD than the TD. The observation is in consistence with [15], which suggested that the d_{tran} should be larger than d_{rol} for circumferential hydride, since circumferential hydride precipitates much longer along the RD than in the TD. Thus higher compressive stress is generated along the RD due to the larger volume difference between hydride particle and the zirconium matrix (see Fig. 2.8, where hoop direction in tube material corresponds to the TD in sheet material, and axial direction corresponds to the RD). Similar results were observed on variation of d-spacing in matrix phase as well. Examples for matrix are shown in Fig. 4.8(a) to Fig. 4.9(d). For zirconium matrix, initial d-spacing in the RD are larger than that in the TD, which is caused by the higher initial tensile stress on matrix plane along the RD. This corresponds to the higher compressive stress on hydride particles along the RD. Since the stresses on the two phases are from the misfit of the volume, higher compressive stress on hydride phase would generate higher tensile stress on the zirconium matrix phase, and vise versa.

The lattice strains of the two phases are then calculated by

$$\varepsilon_{\text{lattice}} = \frac{d_{\sigma}^{200^{\circ}\text{C}} - d_{0}^{200^{\circ}\text{C}}}{d_{0}^{200^{\circ}\text{C}}} \tag{4.1}$$

where $d_{\sigma}^{200^{\circ}\text{C}}$ is the plane spacing at 200 °C with stress σ, and $d_{0}^{200^{\circ}\text{C}}$ is the plane spacing at 200

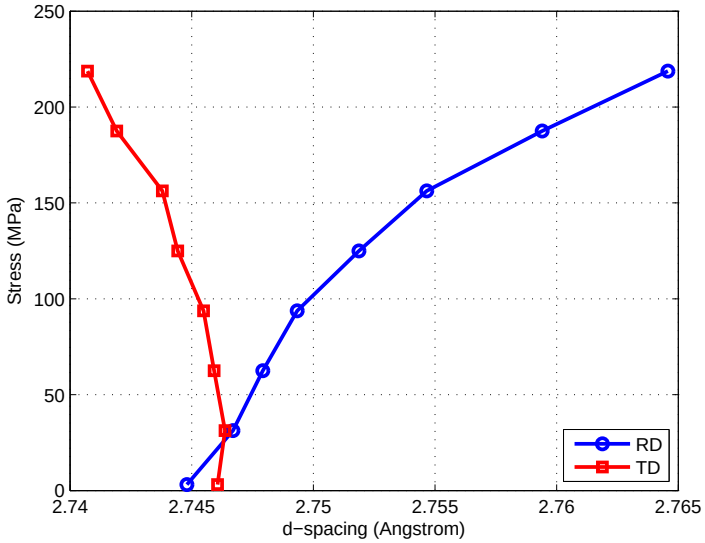

(a) δ (111) w/ 977 wppm H_2

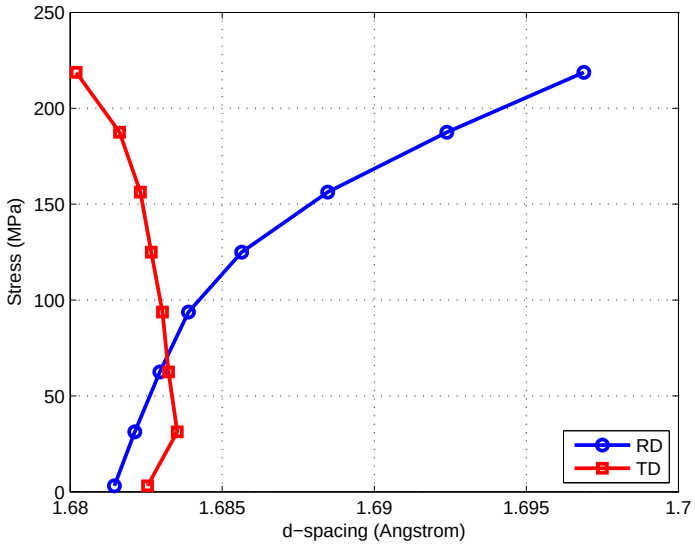

(b) δ (220) w/ 977 wppm H_2

Figure 4.7: Variation of hydride plane spacing while the external tensile stress was applied in the RD. (a) δ (111) (b) δ (220) plane. The blue line is the d-spacing in the RD and the red line is in the TD. Data were recorded at 200 °C.

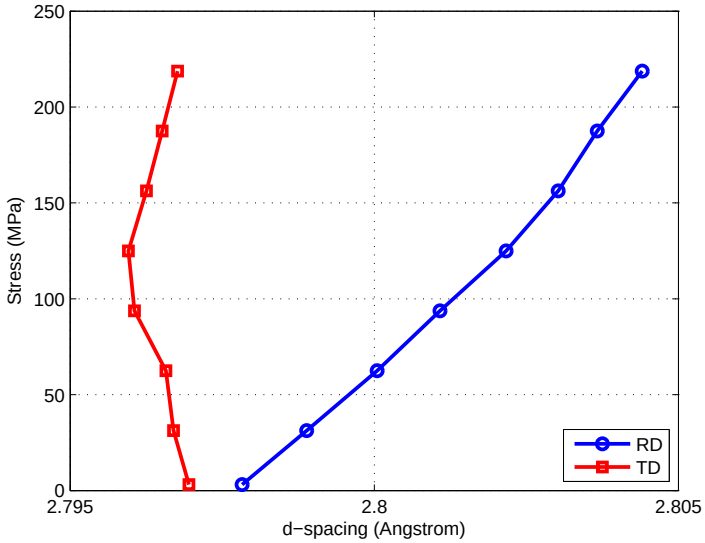

(a) α (100) w/ 977 wppm H_2

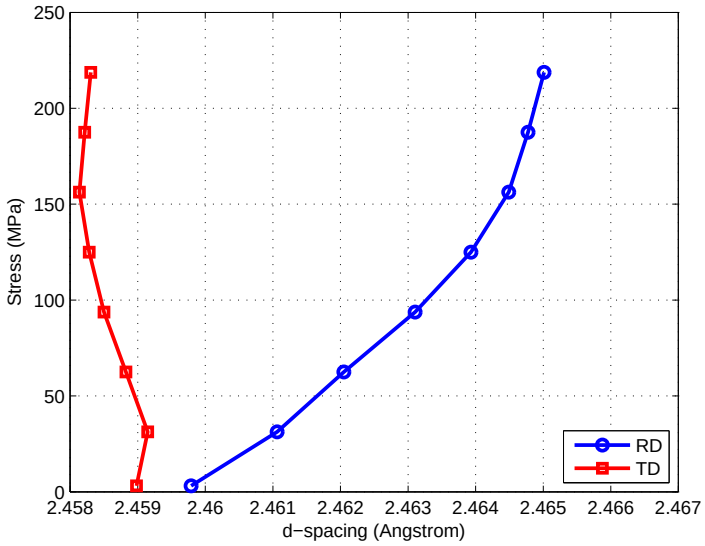

(b) α (101) w/ 977 wppm H_2

Figure 4.8: Variation of zirconium plane spacing while the external tensile stress was applied in the RD. (a) α (100) (b) α (101) (c) α (102) and (d) α (110) plane. The blue line is the d-spacing in RD and the red line is in the TD. Data were recorded at 200 °C.

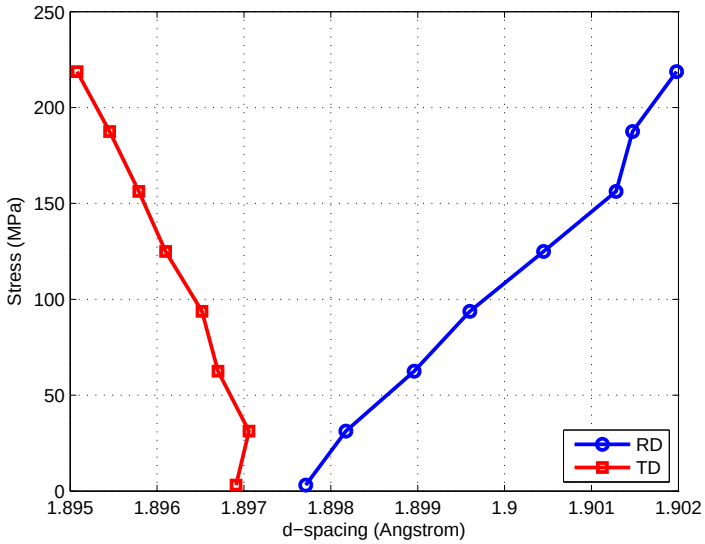

(c) α (102) w/ 977 wppm H_2

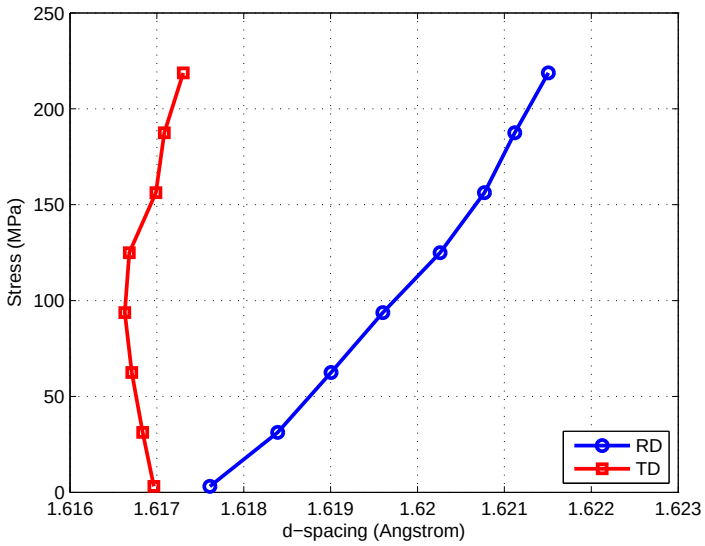

(d) α (110) w/ 977 wppm H_2

Figure 4.8 (cont.)

°C without stress. For both α zirconium and δ hydride phase, $d_0^{200°C}$ is used as the reference for lattice strain calculation, based on an assumption that all phases underwent uniform thermal expansion and thermal expansion dose not contribute significantly to the stress of each phase. The $d_0^{200°C}$ value of each phase is determined by performing two linear fittings on the d-spacing data in the linear region of two directions, and is determined as the intersection of the two linear functions. Since the d-spacing varied linearly with the stress in the linear region, the intersection of the two linear functions represents the stress free d-spacing of the two directions and is taken as $d_0^{200°C}$. Examples of $d_0^{200°C}$ determination for δ (111) hydride and α (100) zirconium peak are shown in Fig. 4.9(a) and Fig. 4.9(b), respectively. Fittings are performed by linear best fit of least square method. The corresponding stress at $d_0^{200°C}$ is also determined.

For δ (111) plane, the $d_0^{200°C}$ is higher than the initial value of d in the RD but smaller than the initial value of d in the TD. The opposite behavior is observed on the matrix plane. The residual stress on the lattice planses can also be quantified as the corresponding stress at the intersection of the two linear functions and times a negative sign, since the corresponding stress is the stress magnitude that needs to be applied to bring the d-spacing back to the stress free value. However, this quantification is only valid in the RD, since in the TD the d-spacing is affected by the Possion's response; also, this is only valid under assumption that hydride is compressed and zirconium is stretched initially, by knowing a fact that 17% more volume can be induced by hydride precipitation [30]. A summary of the residual stress and the $d_0^{200°C}$ of the two phases for all samples are listed in Table 4.4. The residual compressive stress on the hydride phase increases with increases amount of hydrogen, however the residual tensile stress on the zirconium phase decreases or remains unchanged with increases amount of hydrogen. The sample with a notch is observed to have the lowest compressive stress on the hydride phase but the highest tensile stress on the zirconium phase. This indicates that the notch releases the compressive stress on the hydride phase but generates more tensile stress on the matrix lattice. δ (220) is observed to have higher residual compressive stress than δ (111). However, the residual tensile stresses among matrix peaks do not vary too much.

The lattice strain of the four α zirconium peaks is averaged to minimize the elastic and

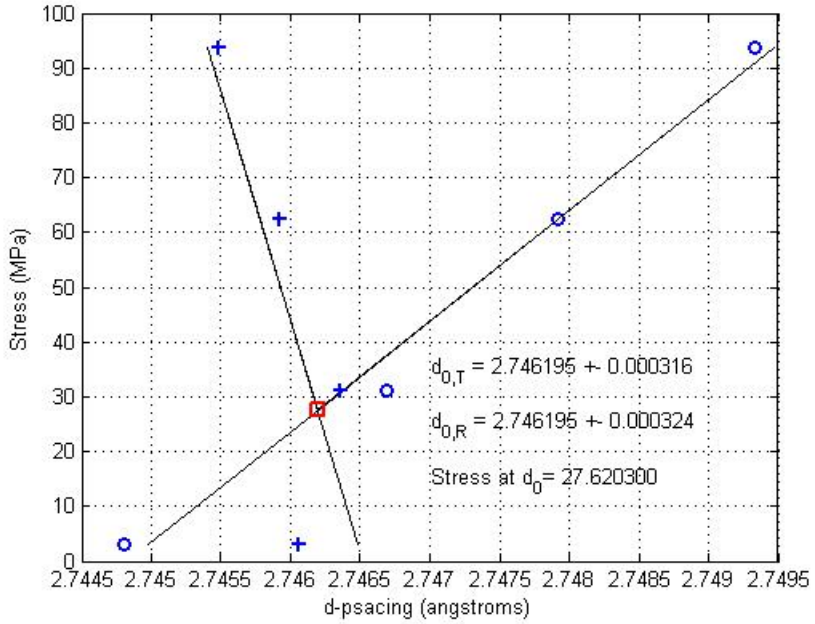

(a) δ (111) w/ 977 wppm H_2

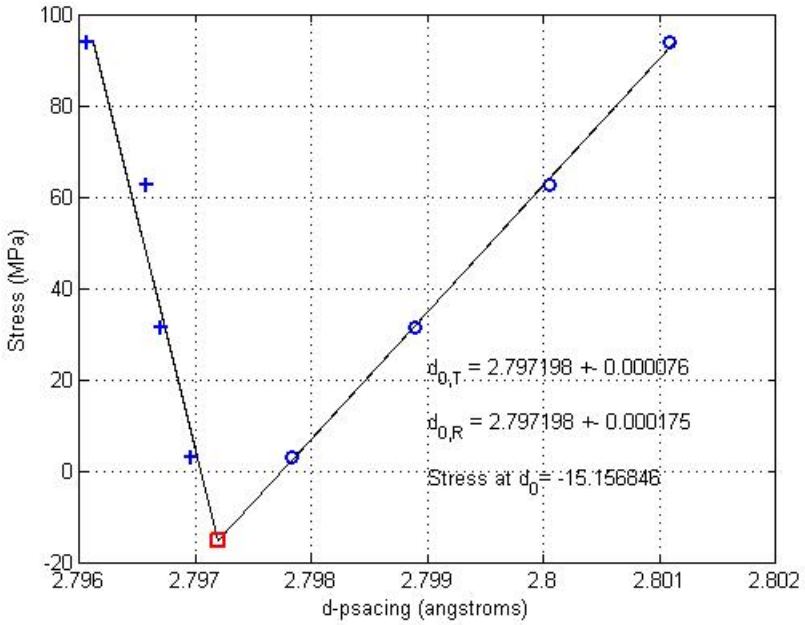

(b) α (100) w/ 977 wppm H_2

Figure 4.9: Determination of the reference plane spacing of (a) δ (111) (b) α (100) plane. The blue cross and circles are data points of d-spacing in the RD and TD in the linear region. Two black lines are linear fitting curve and the red square is the intersection of the two linear functions.

Table 4.4: Summary of the $d_0^{200°C}$ fitting results.

Phase (hkl)	**Sample**	**D_0 at 200°C (Å)**	**Residual stress on the lattice (MPa)**
δ(111)	PDF (00-034-0649)	2.76	...
	98 wppm	2.749	-1.09
	492 wppm w/notch	2.7463	-13.98
	492 wppm	2.7458	-27.96
	977 wppm	2.7462	-27.63
δ(220)	PDF (00-034-0649)	1.6903	...
	98 wppm	...	...
	492 wppm w/notch	1.6840	-43.2
	492 wppm	1.6838	-66.49
	977 wppm	1.6830	-61.79
α(100)	PDF (04-008-1477)	2.8077	...
	98 wppm	2.7967	23.51
	492 wppm w/notch	2.7974	28.11
	492 wppm	2.7971	16.85
	977 wppm	2.7972	15.16
α(101)	PDF (04-008-1477)	2.4672	...
	98 wppm	2.4598	28.50
	492 wppm w/notch	2.4597	31.62
	492 wppm	2.4595	12.22
	977 wppm	2.4594	11.51
α(102)	PDF (04-008-1477)	1.9015	...
	98 wppm	1.8976	10.08
	492 wppm w/notch	1.8977	20.55
	492 wppm	1.8976	7.03
	977 wppm	1.8972	15.93
α(110)	PDF (04-008-1477)	1.621	...
	98 wppm	1.6173	25.08
	492 wppm w/notch	1.6173	35.27
	492 wppm	1.6172	16.05
	977 wppm	1.6171	25.07

Hydride peak δ (220) is not observed in sample with 98 wppm hydrogen content due to low hydrogen concentration.

plastic anisotropic effect [14]. Comparisons of lattice strain between the matrix and hydride are plotted in Fig. 4.10(a) to Fig. 4.11(d). The (111) hydride peak in the sample with 98 wppm hydrogen concentration shows relatively high lattice strain; however this is caused by large peak fitting error on hydride peak in this sample due to the low hydrogen concentration. Longer x-ray exposure time was not applied to increase the statistics of diffraction intensity of the hydride phase. For both hydride and matrix phase in all samples, two regions are observed from the lattice strain evolution curve in the RD, which are identified as Regime I) initial linear region and Regime II) second linear region with different slope. Similar observation on (111) hydride were reported by Kerr et al. [14]. They also observed the third Regime, which was the saturation of lattice strain after the Regime II. Since in this study the applied stress is much lower (maximum applied stress is ∼200 MPa lower than the [14]), the strain saturation region is not observed.

The transition from Regime I to Regime II is caused by the transfer of load from softer zirconium matrix to harder δ hydride phase [14]. The slope of lattice strain of hydride is observed to decrease in Regime II, which implies more strain is carried by the hydride phase at the same applied stress, while in matrix the slope increases in Regime II which implies less strain is carried by the matrix at the same applied stress. This load transfer can be further quantified by using von Mises equivalent stress equation [88, 89], which will be discussed in the next section. The stress at the transition point is ∼90 MPa for hydrides and is ∼140 MPa for zirconium matrix regardless of the hydrogen content. This observation is much smaller than the value reported by Kerr et al. [14], who observed 267.3 MPa transition stress for δ (111) hydride at the room temperature. The difference may be due to the different test temperature and hydride distribution (hydride distributed uniformly in [14]) between the two studies.

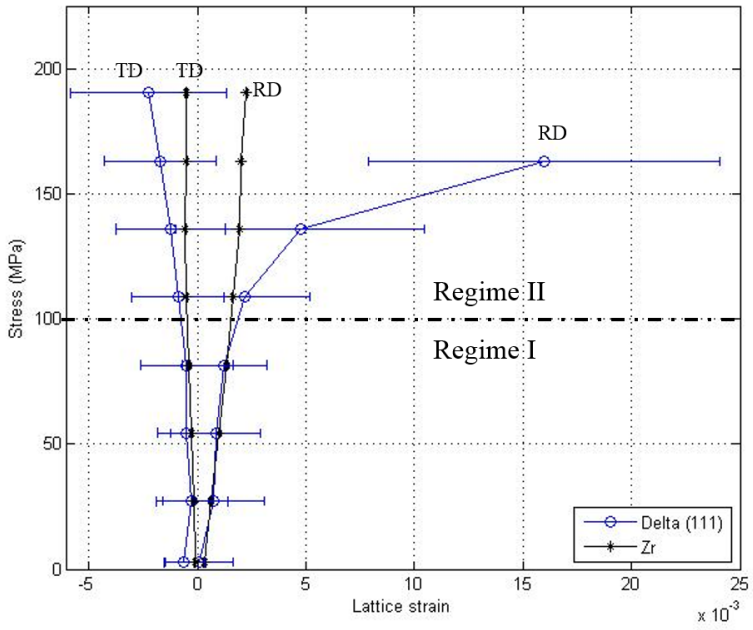

(a) Sample w/ 98 wppm H_2

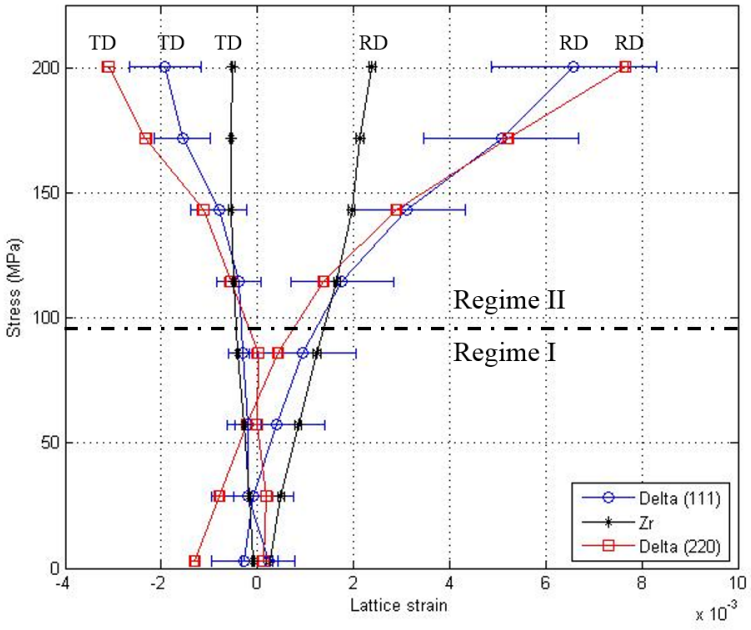

(b) Sample w/ 492 wppm H_2

Figure 4.10: Lattice strain versus applied tensile stress of sample (a) w/ 98 wppm H_2 (b) w/ 492 wppm H_2 (c) w/ 492 wppm H_2 and the notch and (d) w/ 977 wppm H_2. All data were recorded at testing temperature of 200 °C. Hydride δ (220) peak is not observed in the sample with low H_2 content.

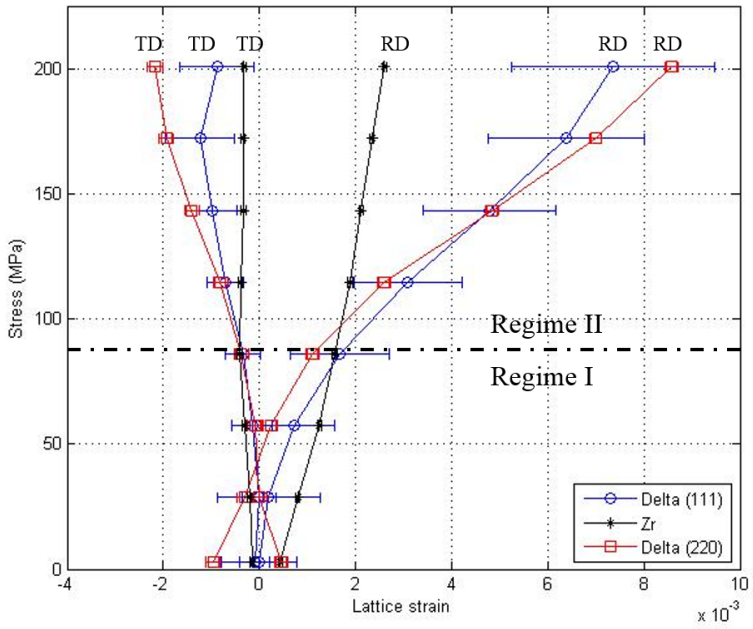

(c) Sample w/ 492 wppm H_2 and the notch

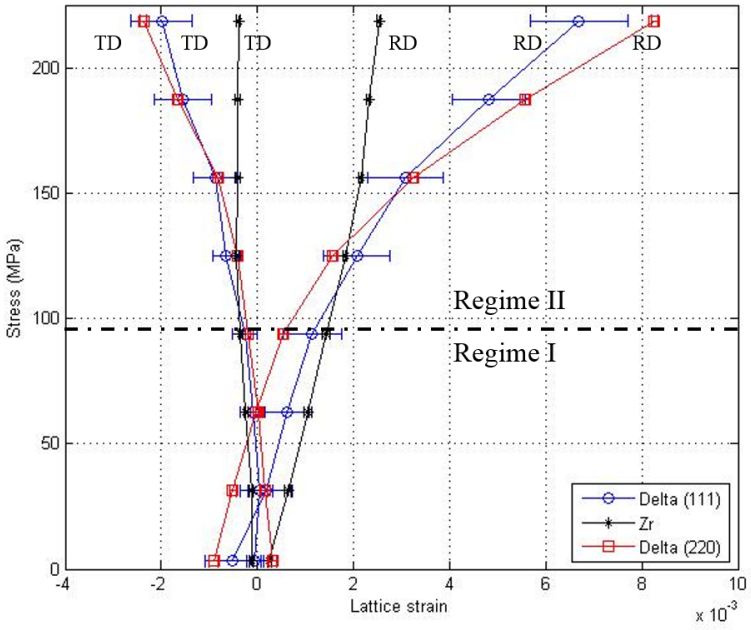

(d) Sample w/ 977 wppm H_2

Figure 4.10 (cont.)

4.3 Load partitioning between the hydride and zirconium phases

The transition from Regime I to Regime II is caused by the effect of load partitioning between the zirconium and hydride phase, which can be quantified by using von Mises equivalent stress equation [90]

$$\sigma_{eff} = \sqrt{\frac{(\sigma_{11} - \sigma_{22})^2 + (\sigma_{22} - \sigma_{33})^2 + (\sigma_{33} - \sigma_{11})^2}{2}} \tag{4.2}$$

where σ_{11}, σ_{22} and σ_{33} are three principal stresses. In this study, σ_{11} corresponds to the stress in the RD, σ_{22} is in the TD and σ_{33} is in the ND, which is calculated from the lattice strain in three directions (ϵ_{11}, ϵ_{22} and ϵ_{33}). In uniaxial tensile test σ_{22} and σ_{33} are generated by the Poisson's response and are equal to each other if the material is isotropic. This is assumed to be valid here. Three principal stresses are calculated by the following equations:

$$\sigma_{11} = \frac{E_{11}}{1+\nu}\epsilon_{11} + \frac{\nu E_{11}}{(1+\nu)(1-2\nu)}(\epsilon_{11} + \epsilon_{22} + \epsilon_{33}) \tag{4.3a}$$

$$\sigma_{22} = \sigma_{33} = \frac{E_{22}}{1+\nu}\epsilon_{22} + \frac{\nu E_{22}}{(1+\nu)(1-2\nu)}(\epsilon_{11} + \epsilon_{22} + \epsilon_{33}) \tag{4.3b}$$

where E is the elastic modulus and ν is Poisson's ratio. E_{11} and E_{22} are the elastic modulus in the RD and the TD, which are obtained by linear fitting on lattice strain curves in Regime I. ν is calculated from the ratio of E_{11} and $|E_{22}|$. The results of E and ν are summarized in Table 4.5.

The elastic modulus of α zirconium at 200 °C measured in this study is in good agreement with published values by Armstrong and Brown [91]. The calculated Poisson's ratio of α zirconium for all samples is also in good agreement with published result [34]. Both the elastic modulus and the calculated Poisson's ratio of hydride are in the reasonable range [23]. These comparisons indicate that the fitting results in Table.4.5 are valid.

Effective internal stresses (von Mises stresses) on each phase are then calculated by using Eq. (4.2) and Eq. (4.3). The calculated von Mises stresses of the two phases are plotted as the function of the applied stress in Fig. 4.11 to Fig. 4.13.

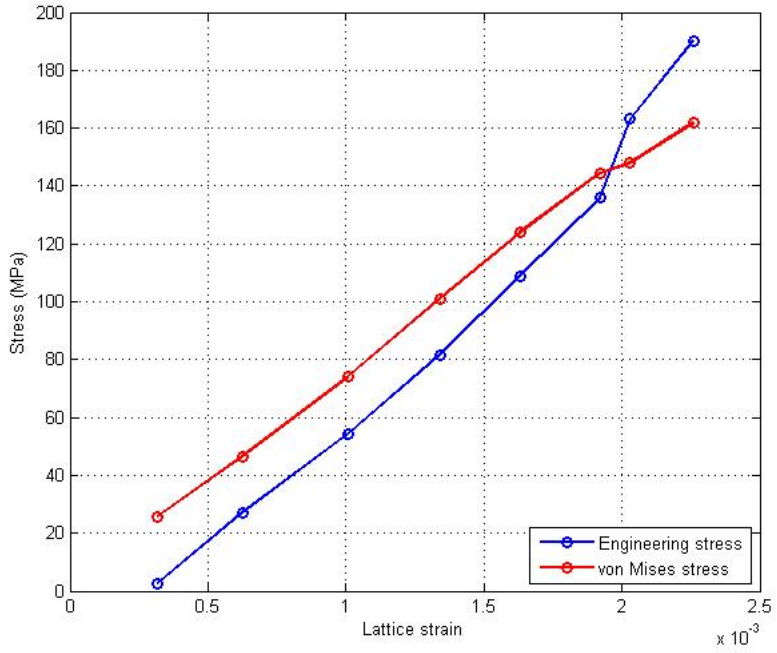

(a) α Zirconium. Sample with 98 wppm H_2

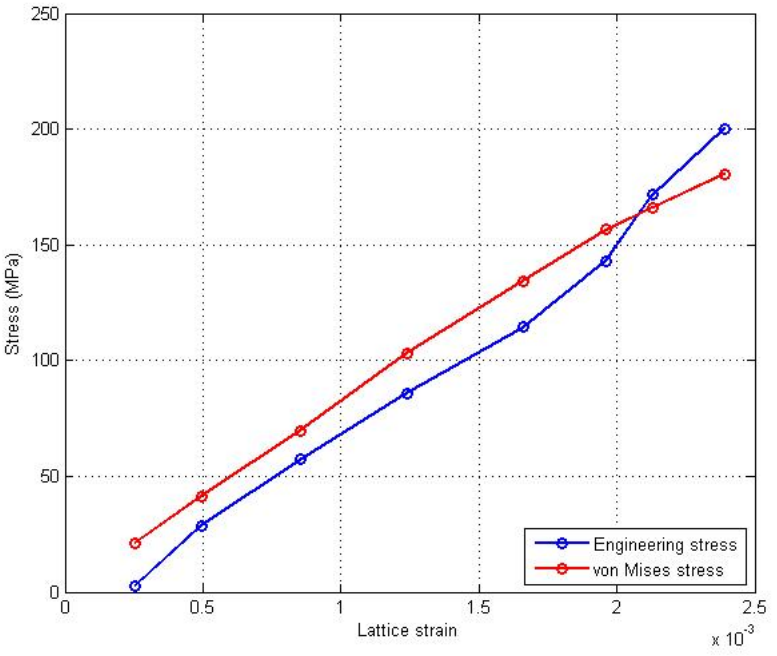

(b) α Zirconium. Sample with 492 wppm H_2

Figure 4.11: Comparison between von Mises and engineering stress as the function of lattice strain of α Zirconium phase for sample (a) with 98 wppm H_2 (b) with 492 wppm H_2 (c) with 492 wppm H_2 and the notch and (d) with 977 wppm H_2. All data were recorded at 200 °C. Red line is the von Mises stress and blue line is engineering stress.

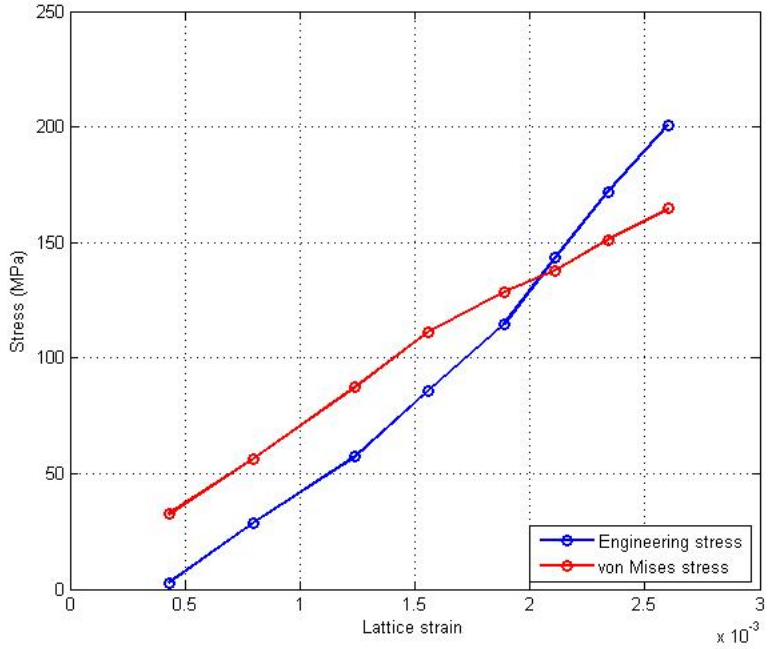

(c) α Zirconium. Sample with 492 wppm H_2 and the notch

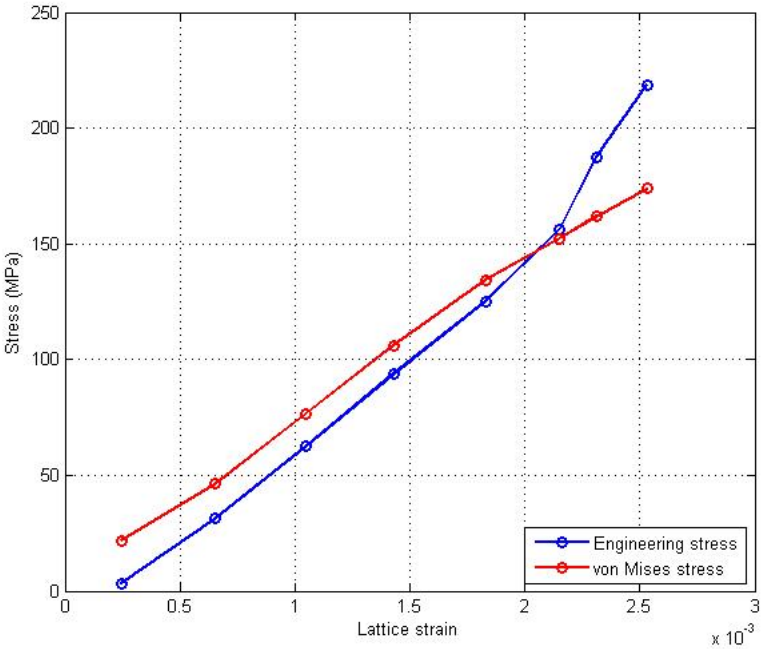

(d) α Zirconium. Sample with 977 wppm H_2

Figure 4.11 (cont.)

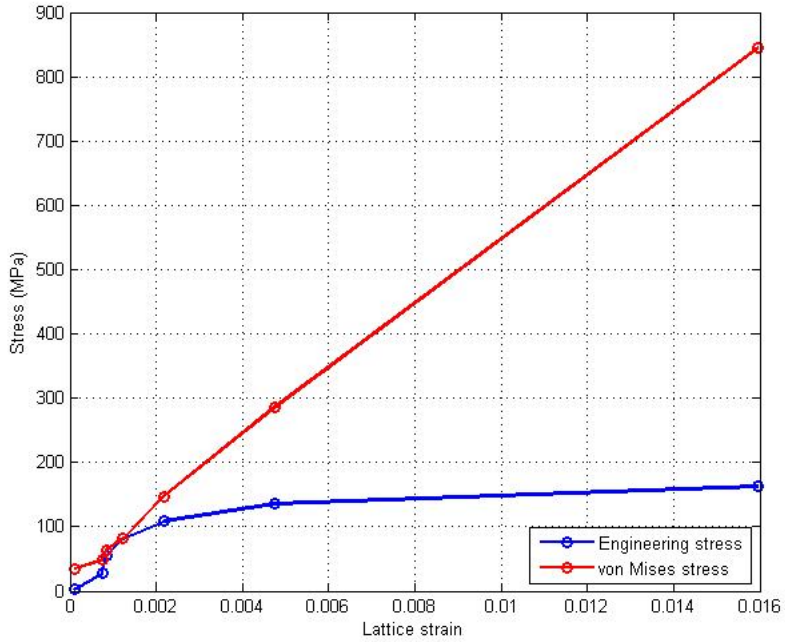

(a) δ (111). Sample with 98 wppm H_2

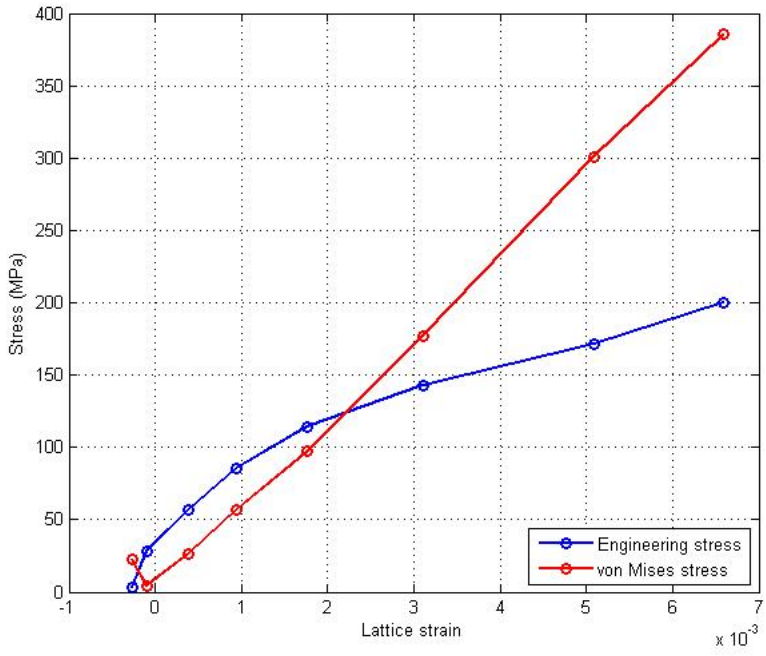

(b) δ (111). Sample with 492 wppm H_2

Figure 4.12: Comparison between von Mises and engineering stress as the function of lattice strain of δ (111) plane for sample (a) with 98 wppm H_2 (b) with 492 wppm H_2 (c) with 492 wppm H_2 and the notch and (d) with 977 wppm H_2. All data were recorded at 200 °C. Red line is the von Mises stress and blue line is engineering stress.

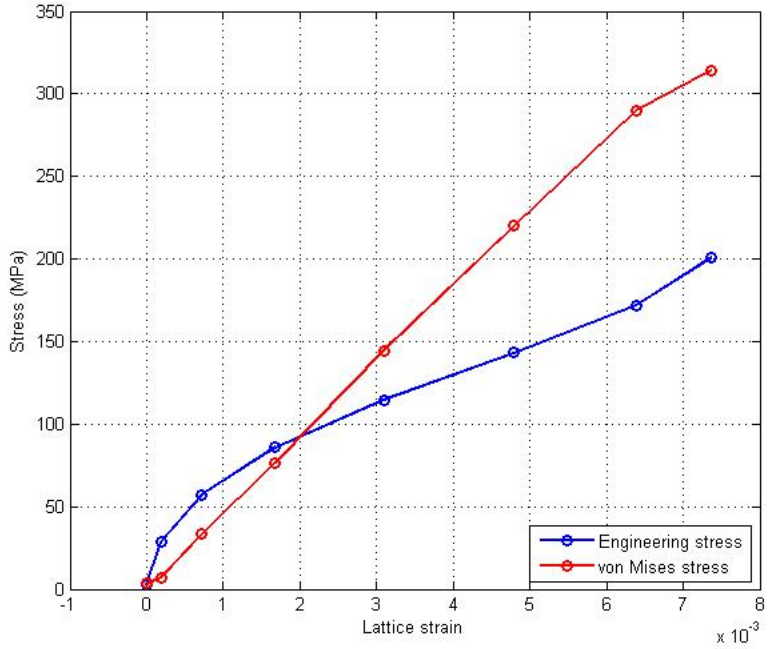

(c) δ (111). Sample with 492 wppm H_2 and the notch

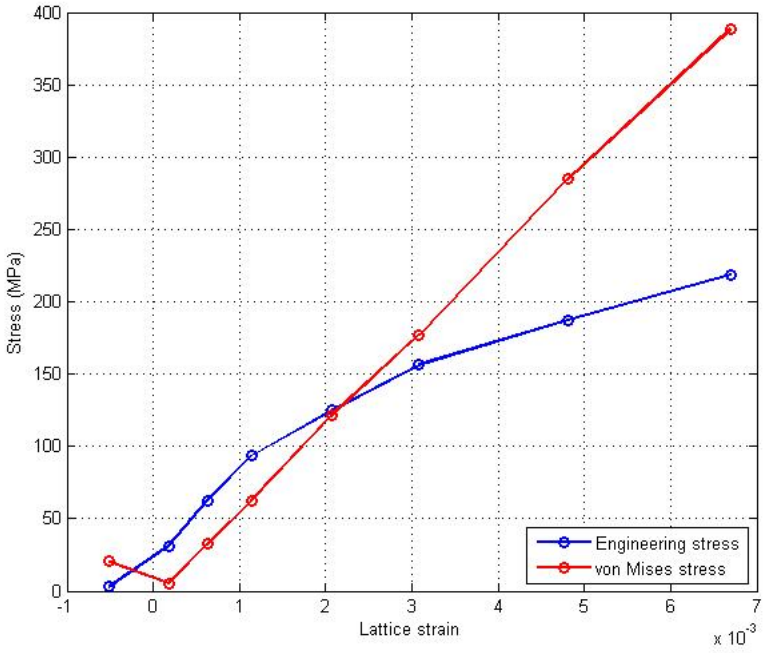

(d) δ (111). Sample with 977 wppm H_2

Figure 4.12 (cont.)

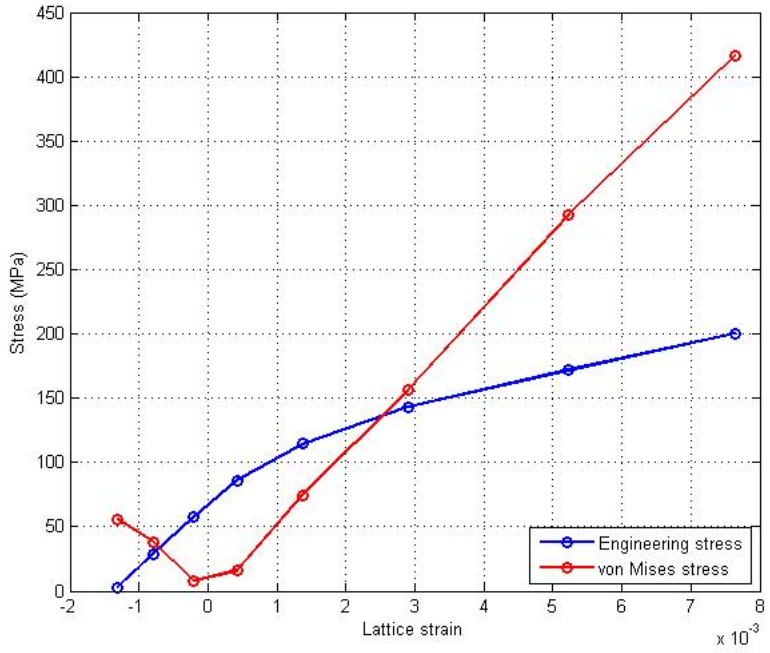

(a) δ (220). Sample with 492 wppm H_2

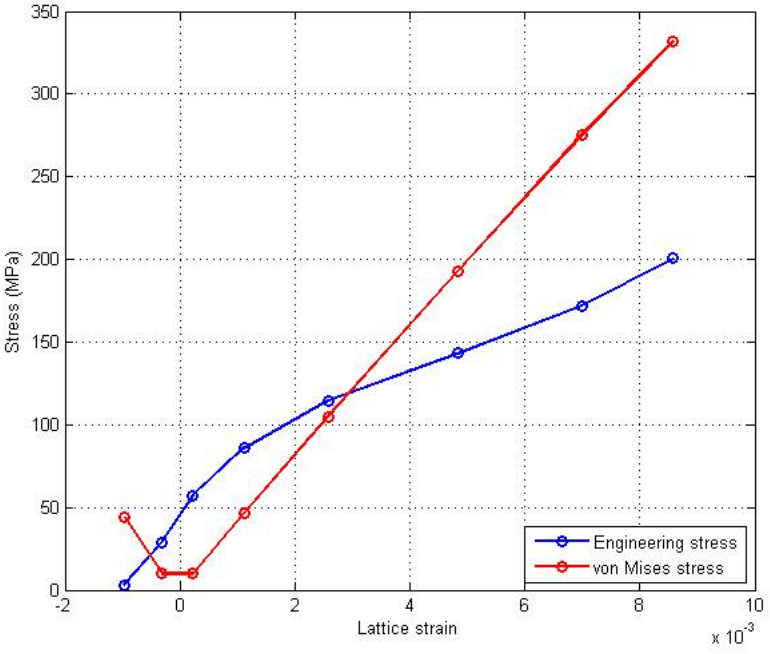

(b) δ (220). Sample with 492 wppm H_2 and the notch

Figure 4.13: Comparison between von Mises and engineering stress as the function of lattice strain of δ (220) plane for sample (a) with 492 wppm H_2 (b) with 492 wppm H_2 and the notch and (c) with 977 wppm H_2. All data were recorded at 200 °C. Red line is the von Mises stress and blue line is engineering stress.

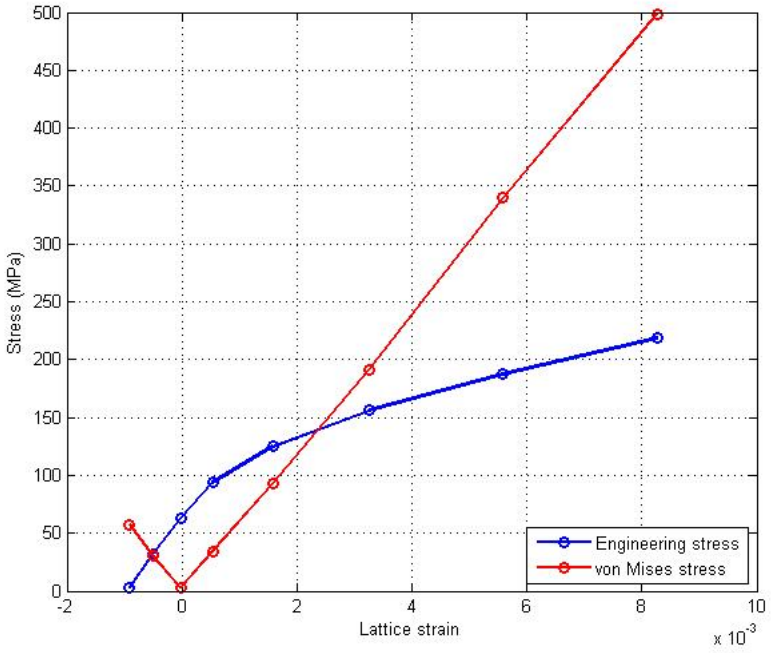

(c) δ (220). Sample with 977 wppm H_2

Figure 4.13 (cont.)

Table 4.5: Summary of fitting results of E and ν.

Phase (hkl)	**Sample**	E_{11} **(GPa)**	$\lvert E_{22}\rvert$ **(GPa)**	**Poisson's ratio**
δ(111)	98 wppm	68.94±15.67	162.11±108.44	0.44±1.25
	492 wppm w/notch	45.91±9.20	168.41±7.71	0.21±0.34
	492 wppm	64.44±8.82	145.52±21.45	0.42±0.79
	977 wppm	55.51±4.56	194.94±0.69	0.24±0.61
δ(220)	98 wppm	...	...	...
	492 wppm w/notch	40.64±2.73	99.88±19.10	0.32±0.22
	492 wppm	48.04±0.93	283.26±182.87	0.24±0.15
	977 wppm	62.45±0.23	182.46±14.57	0.33±0.06
α Zr	98 wppm	76.11±1.82	286.83±36.47	0.30±0.04
	492 wppm w/notch	71.99±3.41	302.97±22.94	0.28±0.03
	492 wppm	82.91±4.76	246.60±20.52	0.33±0.05
	977 wppm	76.58±2.16	276.45±3.96	0.29±0.06

Hydride peak δ (220) is not observed in sample with 98 wppm hydrogen content due to the low hydrogen concentration.

For α zirconium phase in Regime I, the Von mises is higher than the engineering stress and increase with the slope as for the engineering stress. After the engineering stress reaches the transition point of Regime I to Regime II ($\sim$140 to 150 MPa except for the sample with a notch), the slope of the internal stress decreases and the value becomes lower than the engineering stress. However, different behavior is observed in hydride planes. The internal stress on hydride phase first decreases as engineering stress increases, which is because the applied tensile stress relieves the residual compressive stress on the hydride phase. The internal stress then increases with the same slope as in the engineering stress after all compressive stress is relieved. Different from the zirconium phase, the internal stress on hydride in Regime I is lower than the engineering stress. After engineering stress reaches the transition point ($\sim$ 90 MPa except for the sample with a notch), the slope of the engineering stress decreases but the internal stress continues to increase linearly, which results in higher internal stress than engineering stress in Regime II. All these observations indicate that the load on zirconium phase is transferred to harder hydride phase [14]. This phenomenon has also been observed in steel, where load is transferred from soft α Fe matrix to stronger second phase particle [88, 89] when the applied stress is larger than the yield strength of the matrix, thus strengthens the matrix. The transition point of load transfer is $\sim$140 MPa for zirconium, which is close the yield strength of zirconium at 200 °C. However, the transition point for hydride is observed lower than yield strength of zirconium, which is $\sim$90 MPa observed in this study. Similar result was also observed by Kerr et al. [14], where the observed transition point for hydride was 267.3 MPa, which was lower than the yield strength of zirconium at the room temperature.

Among the two hydride planes, δ (220) has the highest internal stress which is $\sim$220 MPa higher than the engineering stress at the maximum applied stress in this study. The difference between the internal stress on the hydride and on the matrix phase is calculated as

$$\triangle\sigma_{\text{internal}} = \sigma_{\text{internal}}^{\text{hydride}} - \sigma_{\text{internal}}^{\text{matrix}} \tag{4.4}$$

and the result is summarized in Table 4.6. For both δ (111) and (220) hydride plane, the difference of internal stress between the hydride and the matrix increases as hydrogen content

increases, and this effect is more significant for (220) hydride plane. This implies more load is transferred from matrix to hydride when more hydride precipitates in the material. For the sample with a notch, this difference is smaller than the sample with the same hydrogen concentration. A possible explanation is that the internal stress on the hydride is relieved by crack propagation in front of the notch tip. The relief of the internal stress is also observed in Fig. 4.13(c).

Table 4.6: Summary of $\triangle\sigma_{\text{internal}}$.

Phase (hkl)	**Sample**	$\triangle\sigma_{internal}$ **(MPa)**
$\delta(111)$	98 wppm	680.3
	492 wppm w/notch	149.25
	492 wppm	204.82
	977 wppm	214.38
$\delta(220)$	98 wppm	...
	492 wppm w/notch	167.01
	492 wppm	235.93
	977 wppm	324.93

A large $\triangle\sigma_{internal}$ value for sample with 98 wppm hydrogen is not reliable due to the large peak fitting error.

4.4 Evolution of the FWHM and intensity of diffraction peaks

The evolution of FWHM of the (220) hydride peak is shown in Fig. 4.14. The evolution of normalized integrated intensity of the (220) hydride peak is also shown in Fig. 4.15. For δ hydride phase, only (220) plane is shown since the fitting error of FWHM and intensity for (111) plane is too large, masking the evolution trend. The unit of FWHM used here is radial position. Note that the testing step along the x axis, which is shown in the figures, is not a real time scale. In real time scale the time spent in stress-increased region is much shorter than the time spent in stress-held region (see Fig. 3.8). Since the object is to investigate the evolution of FWHM during the test, the unitless testing step is used in the figures for clarity.

The FWHM of diffraction peaks are affected by strain broadening and particle size broadening [92]. The signature of variation of fwhm for δ hydride (111) plane was reported by Colas et al. [13, 60], who observed the fwhm of δ (111) peak increased in applied stress direction but remained unchanged in the direction perpendicular to the stress. However, the different trend for δ (220) is observed in this study. For samples without a notch, the fwhm for δ (220) in stress applied direction (RD) decreases as the stress increases, while the FWHM increases in the direction perpendicular to the stress (TD). The decreases of fwhm in RD is due to the combination effect of strain relief (relief of the residual stress) and the change of hydride particle morphology. The external tensile stress relieves the nonuniform strain which is generated by hydride precipitation. The effect of particle size can be seen on sample with a notch. In this sample the FWHM in the RD remained unchanged while nonuniform strain is created around the notch, which implies that the effect of particle size balances out the effect of the strain broadening. The observation also implies that the hydride particle size might increase in the RD during the test, which is a possible sign of hydride reorientation, since from Scherrer equation the increase of particle size will decrease the breadth of the peak profile [92, 93]. For all samples the fwhm of δ (220) plane increases in the TD. The increases of FWHM is possibly due to the combination effect of strain broadening (due to the highly texture and anisotropic characteristic of the zirconium matrix) and particle size broadening (decreases of particle size will increase the FWHM).

Williamson-Hall equation [94] or modified Williamson-Hall equation [95] is commonly used to quantitatively separate the contribution of the two broadening mechanisms. However, at least 5 peaks are needed in order to perform Williamson-Hall analysis accurately, which is not the case in this study since only two hydride peaks were identified.

For all samples, the normalized intensity of δ (220) peak slightly decreases in the RD but remains unchanged in the TD. The decreased of intensity is caused by hydride dissolution at 200 °C. The unchanged hydride normalized intensity in the TD is probably caused by change of hydride morphology, which balances the dissolution effect. For sample with 977 wppm hydrogen, the normalized intensity in the TD even increases, which might imply that sample with higher hydrogen content is more susceptible to stress-induced change of hydride morphology. However, it was observed by Une et al. [96] that the reoriented hydride (radial hydride) has very similar orientation relationship with the matrix as the initial hydride (circumferential hydride). The observation then implies that using individual hydride lattice plane to study the hydride reorientation is difficult or might be unreliable. Thus it is better to study the phase macroscopic representative behavior by using Rietveld refinement, which is out of scope of this thesis but will be included in the future work.

It should be noted that the FWHM and intensity of zirconium peaks were also fitted. The FWHM of zirconium peaks slightly decreases (much less than the variation of FWHM of hydride peaks) in both the TD and RD when stress is increased. The integrated intensity of zirconium peaks remains unchanged over the whole testing period. This suggests that the zirconium matrix is relative stable and have minor or zero effect on the observed behavior of the peak characteristic of hydride peaks.

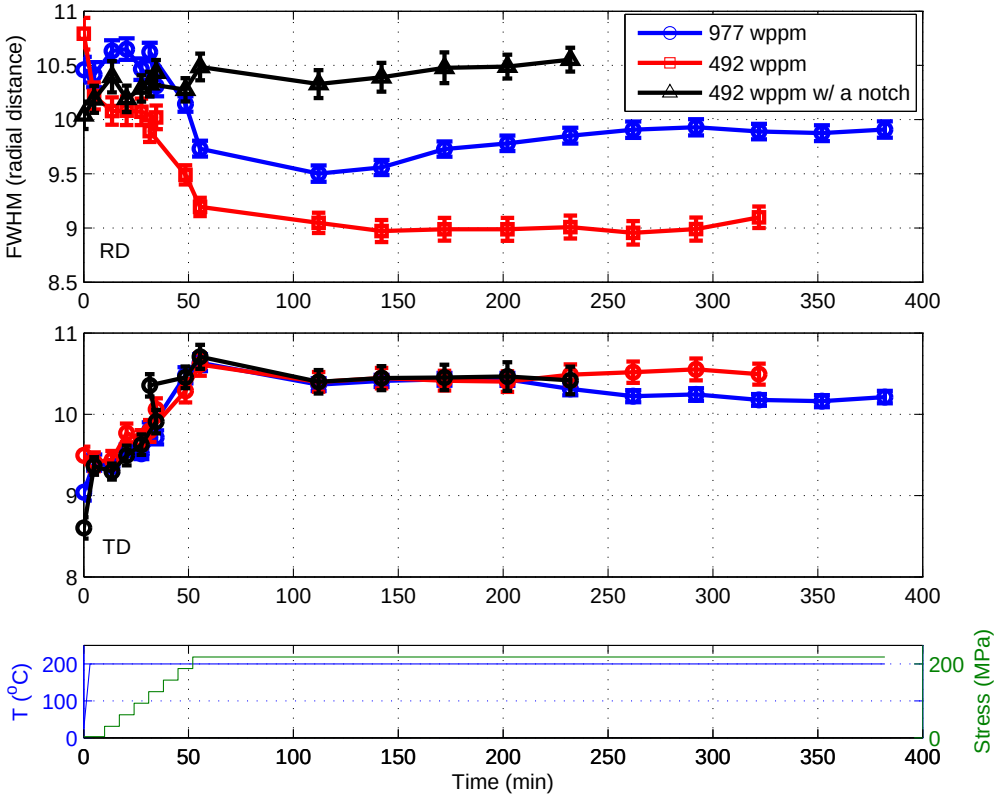

Figure 4.14: Evolution of FWHM of δ (220) hydride plane in the TD and RD during the *in-situ* test. A subfigures show the corresponding test environment. Stress is applied in the RD.

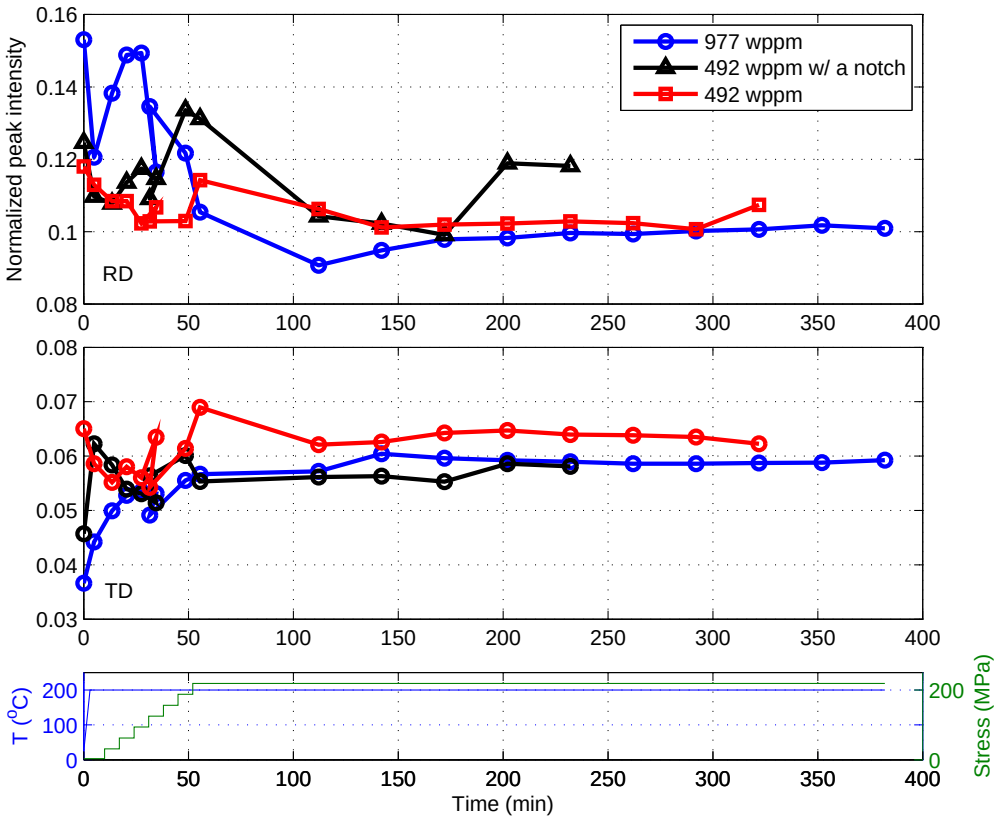

Figure 4.15: Evolution of normalized integrated intensity of δ (220) hydride plane in the TD and RD during the *in-situ* test. A subfigure shows the corresponding test environment. Stress is applied in the RD.

CHAPTER 5

CONCLUSION

High energy synchrotron x-ray diffraction was used to study and characterize the mechanical response of hydride phase in a CWSR Zry-4 plate with hydride blister/rim distribution while external tensile stress is applied. The purpose is to understand the effects of hydride blister/rim structure and different hydrogen concentrations on the mechanical behavior of both hydride and zirconium phase. The following are general conclusions based on the observation and analysis in this study:

1. For hydrogen concentration of $\leq$ 977 wppm and a cooling rate of 1 $^{\circ}\mathrm{C\,min^{-1}}$, the f.c.c δ hydride is the only hydride phase identified by the synchrotron x-ray diffraction. The precipitation of SPPs (hexagonal C14 laves phase) in Zry-4 is also identified.

2. After the precipitation of hydride in zirconium matrix, the volume difference of unit cell between the two phases results in compressive stress on the hydride phase and tensile stress on the zirconium matrix. The magnitude of the stress is observed increases with increases amount of hydrogen in the material. The induced stress after hydride precipitation can be quantified, which is -27.8 MPa on δ (111) hydride, -64.14 MPa on δ (220) hydride and 15 MPa on α zirconium for sample with 977 wppm hydrogen. For sample with a notch, the compressive stress on hydride decreases and the tensile stress on zirconium increases.

3. When external tensile stress is applied in the RD, the lattice strain of hydride is higher than the lattice strain of zirconium matrix. The difference is about a factor of three for all samples at the highest applied stress in this study.

4. Two regions are observed in lattice strain evolution for both hydride and matrix phase. The load partitioning between the two phases is responsible for the transition. The

transition point is approximate 90 MPa for the hydride and is approximate 140 MPa for the zirconium matrix phase. These transition points are lower than published values from a study where hydride phase was distributed uniformly. This may imply the presence of hydride blister/rim structure decreases the ability of zirconium matrix to sustain load, transferring load to the hydride phase at lower stress. However, these two studies were preformed at different temperature and a consistence work need to be carried out to verify the conclusion.

5. The effective von Mises stress on the hydride and zirconium phases can be quantified. It is observed that the internal stress on the hydride phase increases with increases hydrogen content, and the highest internal stress is observed on δ (220) plane. From the effective von Mises stress it can be observed that zirconium matrix carries most of load until reaches the yield point. The load then is transferred from zirconium to hydride. This load partitioning is a strengthening mechanism for some alloyed steels, but it will cause early fracture of the brittle hydride phase in Zry-4.

6. The FWHM evolution of δ (220) peak during the test is observed, where the fwhm in the applied stress direction increases and decreases in the direction perpendicular to the stress axis. The peak intensity of δ (220) plane in the applied stress direction also decreases. The observed FWHM evolution is in contrast with previous literature where FWHM increases in direction perpendicular to the stress but remained unchanged in direction parallel to the stress axis while hydride reorientation occurred. This result may indicate hydride reorientation did not occur in this work, since the presence of hydride blister/rim structure impedes the dissolution and reprecipitation of hydride.

More diffraction based study on hydride-zirconium phase will be performed based on the current results, which will be discussed in the next chapter.

CHAPTER 6

FUTURE WORK

Future studies of the hydride phase in Zircaloy cladding should provide a better understanding of the precipitation of hydride phase and susceptibility to the delayed hydride cracking in the conditions relevant to the environment of long term storage of used nuclear fuel. Based on the observed results in this study, several tasks could be performed:

1. *In-situ* thermal cycle testing by utilizing synchrotron x-ray or neutron diffraction under applied load. It has been demonstrated that thermal cycles have more pronounced effect on hydride reorientation than isothermal treatment, and thermal cycling is an unavoidable process (vacuum drying) before the UNF is transported from the storage pool to dry cask. However, until now, all tests have been done on samples which have uniformly distributed hydrides. It is more important to investigate the hydride reorientation behavior for samples which have hydride blister/rim structures near the surface. Beam 1-ID at Advanced Photon Source at Argonne National Lab has ability to perform x-ray diffraction data collection with less than 10s for each data and is suitable to study the reorientation kinetics and determines the threshold stress for reorientation. The size and the shape of the hydride particle can also be studied by small angle x-ray scattering.

2. Post-irradiation with heavy ions can be done by performing with an accelerator. The effect of irradiation fluence, temperature and hydrogen content on the microstructure of hydride could be investigated with TEM. *In-situ* TEM test can also be performed at IVEM-Tandem Accelerator Facility at ANL; the real time evolution of microstructure, such as nucleation or dissolution of hydrides during proton bombardment could be studied.

3. After the clear understanding of precipitation of hydride phase in Zircaloy cladding is established, DHC behavior could be further studied. The crack growth rate of DHC can be characterized by using compact (CT) specimen, wedge-open-loading (WOL) specimen or arc-shaped specimen. Tests could be performed at different temperature, stress and post-irradation condition. The effect of hydride reorientation and post-irradiation on the crack growth rate could be determined, which has not been addressed well in current models. In addition, the effect of hydride distribution (rim or uniform or blister) will also be studied, which has not been covered in current studies or models as well. The DHC could be studied based on the dependence of crack growth rate on the stress intensity factor (K), which is a typical characterization method for DHC.

4. Theoretical development and modeling efforts will be performed to incorporate the data obtained from the proposed studies, including modification of the current models. Models (Ex: fuel performance codes) and theories will help to predict the effect of DHC on cladding integrity during the dry storage and estimate the life of dry cask storage. In addition, the current regulation can be reviewed or modified based on the newly developed models.

REFERENCES

[1] *ASTM Standard B353-12, Specification for Wrought Zirconium and Zirconium Alloy Seamless and Welded Tubes for Nuclear Service (Except Nuclear Fuel Cladding)*, ASTM International, West Conshohocken, PA Std., 2012. [Online]. Available: www.astm.org

[2] Y. S. Kim, "Driving force for delayed hydride cracking of zirconium alloys," *Metals and Materials International*, vol. 11, no. 1, pp. 29–38, 2005.

[3] R. Dutton, K. Nuttall, M. Puls, and L. Simpson, "Mechanisms of hydrogen induced delayed cracking in hydride forming materials," *Metallurgical Transactions A*, vol. 8, no. 10, pp. 1553–1562, 1977.

[4] M. Puls, "Elastic and plastic accommodation effects on metal-hydride solubility," *Acta Metallurgica*, vol. 32, no. 8, pp. 1259 – 1269, 1984. [Online]. Available: http://www.sciencedirect.com/science/article/pii/0001616084901330

[5] J. Kearns, "Terminal solubility and partitioning of hydrogen in the alpha phase of zirconium, zircaloy-2 and zircaloy-4," *Journal of Nuclear Materials*, vol. 22, no. 3, pp. 292 – 303, 1967. [Online]. Available: http://www.sciencedirect.com/science/article/pii/0022311567900475

[6] J. Abriata, J. Bolcich, and D. Arias, "The sn-zn (tin-zirconium) system," *Bulletin of Alloy Phase Diagrams*, vol. 4, no. 2, pp. 147–154, 1983. [Online]. Available: http://dx.doi.org/10.1007/BF02884861

[7] R. L. Beck, "Zirconium-hydrogen phase system," *Am. Soc. Metals, Trans. Quart.*, vol. 55, 1962.

[8] B. Nath, G. Lorimer, and N. Ridley, "The relationship between gamma and delta hydrides in zirconium-hydrogen alloys of low hydrogen concentration," *Journal of Nuclear Materials*, vol. 49, no. 3, pp. 262–280, 1974.

[9] S. Mishra, K. Sivaramakrihnan, and M. Asundi, "Formation of the gamma phase by a peritectoid reaction in the zirconium-hydrogen system," *Journal of Nuclear Materials*, vol. 45, no. 3, pp. 235–244, 1972.

[10] C. Coleman, "Effect of texture on hydride reorientation and delayed hydrogen cracking in cold-worked zr-2.5 nb," in *Zirconium in the Nuclear Industry: Fifth International Symposium, ASTM STP*, vol. 754, 1977, pp. 393–411.

[11] J. Kearns and C. Woods, "Effect of texture, grain size, and cold work on the precipitation of oriented hydrides in zircaloy tubing and plate," *Journal of Nuclear Materials*, vol. 20, no. 3, pp. 241–261, 1966.

[12] H. Chu, S. Wu, and R. Kuo, "Hydride reorientation in zircaloy-4 cladding," *Journal of Nuclear Materials*, vol. 373, no. 1, pp. 319–327, 2008.

[13] K. B. Colas, A. T. Motta, M. R. Daymond, and J. D. Almer, "Effect of thermomechanical cycling on zirconium hydride reorientation studied in situ with synchrotron x-ray diffraction," *Journal of Nuclear Materials*, vol. 440, pp. 586 – 595, 2013. [Online]. Available: http://www.sciencedirect.com/science/article/pii/S0022311513006557

[14] M. Kerr, M. Daymond, R. Holt, and J. Almer, "Strain evolution of zirconium hydride embedded in a zircaloy-2 matrix," *Journal of Nuclear Materials*, vol. 380, no. 1, pp. 70–75, 2008.

[15] V. Alvarez, J. Santisteban, P. Vizcaino, A. Flores, A. Banchik, and J. Almer, "Hydride reorientation in zr2. 5nb studied by synchrotron x-ray diffraction," *Acta Materialia*, vol. 60, no. 20, pp. 6892–6906, 2012.

[16] C. Ells, "The stress orientation of hydride in zirconium alloys," *Journal of Nuclear Materials*, vol. 35, no. 3, pp. 306–315, 1970.

[17] R. Marshall, "Influence of fabrication history on stress-oriented hydrides in zircaloy tubing," *Journal of Nuclear Materials*, vol. 24, no. 1, pp. 34–48, 1967.

[18] P. SLOVIC, J. H. FLYNN, and M. LAYMAN, "Perceived risk, trust, and the politics of nuclear waste," *Science*, vol. 254, no. 5038, pp. 1603–1607, 1991. [Online]. Available: http://www.sciencemag.org/content/254/5038/1603.abstract

[19] E. Brach, "Cladding considerations for the transportation and storage of spent fuel," US Nuclear Regulatory Commission, Spent Fuel Project Office, Rockville, MD, Interim Staff Guidance-11 Rev. 3, 2003.

[20] Y. S. Kim, "Delayed hydride cracking of spent fuel rods in dry storage," *Journal of Nuclear Materials*, vol. 378, no. 1, pp. 30 – 34, 2008. [Online]. Available: http://www.sciencedirect.com/science/article/pii/S0022311508002419

[21] M. Mayuzumi and T. Onchi, "Creep deformation of an unirradiated zircaloy nuclear fuel cladding tube under dry storage conditions," *Journal of Nuclear Materials*, vol. 171, pp. 381 – 388, 1990. [Online]. Available: http://www.sciencedirect.com/science/article/pii/002231159090384Y

[22] R. E. Einziger, H. Tsai, M. Billone, and B. Hilton, "Examination of spent pwr fuel rods after 15 years in dry storage," in *10th International Conference on Nuclear Engineering*. American Society of Mechanical Engineers, 2002, pp. 351–358.

[23] M. Puls, *The Effect of Hydrogen and Hydrides on the Integrity of Zirconium Alloy Components: Delayed Hydride Cracking*, ser. Engineering Materials. Springer London, 2012. [Online]. Available: http://books.google.com/books?id=wKDxctPfv-gC

[24] C. Lemaignan and A. T. Motta, "Zirconium alloys in nuclear applications," *Materials Science and Technology*, 1994.

[25] M. Oskarsson, "Study on the mechanisms for corrosion and hydriding of zircaloy," Ph.D. dissertation, KTH, Materials Science and Engineering, 2000.

[26] C. Simpson and C. Ells, "Delayed hydrogen embrittlement in zr-2.5 wt *Journal of Nuclear Materials*, vol. 52, no. 2, pp. 289 – 295, 1974. [Online]. Available: http://www.sciencedirect.com/science/article/pii/0022311574901743

[27] C. Coleman and J. Ambler, "Delayed hydrogen cracking in zr-2.5 nb alloy," *Reviews on Coating and Corrosion III (2 and 3)*, pp. 105–157, 1979.

[28] S. AAS, "Mechanical interaction between fuel and cladding," *Nuclear Engineering and Design*, vol. 21, no. 2, pp. 237 – 253, 1972. [Online]. Available: http://www.sciencedirect.com/science/article/pii/0029549372900751

[29] S. MacEwen, C. Coleman, C. Ells, and J. F. jr, "Dilation of h.c.p. zirconium by interstitial deuterium," *Acta Metallurgica*, vol. 33, no. 5, pp. 753 – 757, 1985. [Online]. Available: http://www.sciencedirect.com/science/article/pii/0001616085900987

[30] G. Weatherly, "The precipitation of -hydride plates in zirconium," *Acta Metallurgica*, vol. 29, no. 3, pp. 501 – 512, 1981. [Online]. Available: http://www.sciencedirect.com/science/article/pii/0001616081900742

[31] C. Chao, K. Yang, and C. Tseng, "Rupture of spent fuel zircaloy cladding in dry storage due to delayed hydride cracking," *Nuclear Engineering and Design*, vol. 238, no. 1, pp. 124–129, 2008.

[32] D. Haeffner, J. Almer, and U. Lienert, "The use of high energy x-rays from the advanced photon source to study stresses in materials," *Materials Science and Engineering: A*, vol. 399, no. 1, pp. 120–127, 2005.

[33] D. A. Young, *Phase diagrams of the elements*. University of California, Lawrence Livermore Laboratory, 1975.

[34] D. L. Douglass, "Metallurgy of zirconium." Univ. of California, Los Angeles, Tech. Rep., 1971.

[35] B. Lichter, "Precision lattice parameter determination of zirconium-oxygen solid solution," *Trans. Met. Soc. AIME*, vol. 218, 1960.

[36] A. Lowe, G. Parry, A. C. B.-. on Reactive, R. Metals, and Alloys, *Zirconium in the Nuclear Industry: Proceedings of the Third International Conference*, ser. ASTM special technical publication. ASTM, 1977. [Online]. Available: http://books.google.com/books?id=yFLACMvgyQsC

[37] R. Kuwae, K. Sato, E. Higashinakagawa, J. Kawashima, and S.-i. Nakamura, "Mechanism of zircaloy nodular corrosion," *Journal of Nuclear Materials*, vol. 119, no. 2, pp. 229–239, 1983.

[38] W. Yang, R. Tucker, B. Cheng, and R. Adamson, "Precipitates in zircaloy: Identification and the effects of irradiation and thermal treatment," *Journal of Nuclear Materials*, vol. 138, no. 2, pp. 185–195, 1986.

[39] S. R. Luc Moulin and E. Tenckhoff, "Correlation between fabrication parameters, microstructure, and texture in zircaloy tubing," in *Zirconium in the Nuclear Industry: Sixth International Symposium*. ASTM STP 824, 1984, pp. 225–243.

[40] E. Tenckhoff, *Deformation mechanisms, texture, and anisotropy in zirconium and zircaloy*. ASTM International, 1988, vol. 966.

[41] *ASTM B811-13, Standard specification for wrought zirconium alloy seamless tubes for nuclear reactor fuel cladding*, American Society for Testing and Materials Std., 2013.

[42] A. Garde, G. Smith, and R. Pirek, "In-pwr irradiation performance of dilute tin-zirconium advanced alloys," *ASTM SPECIAL TECHNICAL PUBLICATION*, vol. 1423, pp. 490–504, 2002.

[43] K. Barraclough and C. Beevers, "Some observations on the phase transformations in zirconium hydrides," *Journal of Nuclear Materials*, vol. 34, no. 2, pp. 125–134, 1970.

[44] J. Bradbrook, G. Lorimer, and N. Ridley, "The precipitation of zirconium hydride in zirconium and zircaloy-2," *Journal of Nuclear Materials*, vol. 42, no. 2, pp. 142–160, 1972.

[45] M. Warren and D. Bhattacharya, "γ zr-hydride precipitate in irradiated massive δ zr-hydride," *Journal of Nuclear Materials*, vol. 56, no. 1, pp. 121–123, 1975.

[46] B. Nath, G. Lorimer, and N. Ridley, "Effect of hydrogen concentration and cooling rate on hydride precipitation in α-zirconium," *Journal of Nuclear Materials*, vol. 58, no. 2, pp. 153–162, 1975.

[47] G. Dey and S. Banerjee, "Decomposition of the β-phase in zr-20% nb," *Journal of Nuclear Materials*, vol. 125, no. 2, pp. 219–227, 1984.

[48] J. Bailey, "Electron microscope observations on the precipitation of zirconium hydride in zirconium," *Acta metallurgica*, vol. 11, no. 4, pp. 267–280, 1963.

[49] C. Cann and A. Atrens, "A metallographic study of the terminal solubility of hydrogen in zirconium at low hydrogen concentrations," *Journal of Nuclear Materials*, vol. 88, no. 1, pp. 42–50, 1980.

[50] C. Cann, M. Puls, E. Sexton, and W. Hutchings, "The effect of metallurgical factors on hydride phases in zirconium," *Journal of Nuclear Materials*, vol. 126, no. 3, pp. 197–205, 1984.

[51] R. Daum, Y. Chu, and A. Motta, "Identification and quantification of hydride phases in zircaloy-4 cladding using synchrotron x-ray diffraction," *Journal of Nuclear Materials*, vol. 392, no. 3, pp. 453–463, 2009.

[52] E. Tulk, M. Kerr, and M. Daymond, "Study on the effects of matrix yield strength on hydride phase stability in zircaloy-2 and zr 2.5 wt% nb," *Journal of Nuclear Materials*, vol. 425, no. 1, pp. 93–104, 2012.

[53] B. D. Cullity, "Elements of x-ray diffraction," *American Journal of Physics*, vol. 25, pp. 394–395, 1957.

[54] C. P. Kempter, R. O. Elliott, and K. A. Gschneidner Jr, "Thermal expansion of delta and epsilon zirconium hydrides," *The Journal of Chemical Physics*, vol. 33, no. 3, pp. 837–840, 1960.

[55] M. Cassidy and C. Wayman, "The crystallography of hydride formation in zirconium: Ii. the δ ε transformation," *Metallurgical and Materials Transactions A*, vol. 11, no. 1, pp. 57–67, 1980.

[56] O. T. Woo and G. J. Carpenter, "Eels characterization of zirconium hydrides," *Microscopy Microanalysis Microstructures*, vol. 3, no. 1, pp. 35–44, 1992.

[57] Z. Zhao, J.-P. MORNIROLI, A. Legris, A. Ambard, Y. Khin, L. Legras, and M. BLATYRIEIX, "Identification and characterization of a new zirconium hydride," *Journal of microscopy*, vol. 232, no. 3, pp. 410–421, 2008.

[58] A. Steuwer, J. Santisteban, M. Preuss, M. Peel, T. Buslaps, and M. Harada, "Evidence of stress-induced hydrogen ordering in zirconium hydrides," *Acta Materialia*, vol. 57, no. 1, pp. 145–152, 2009.

[59] J. Santisteban, M. Vicente-Alvarez, P. Vizcaíno, A. Banchik, and J. Almer, "Hydride precipitation and stresses in zircaloy-4 observed by synchrotron x-ray diffraction," *Acta Materialia*, vol. 58, no. 20, pp. 6609–6618, 2010.

[60] K. Colas, A. Motta, J. Almer, M. Daymond, M. Kerr, A. Banchik, P. Vizcaino, and J. Santisteban, "In situ study of hydride precipitation kinetics and re-orientation in zircaloy using synchrotron radiation," *Acta Materialia*, vol. 58, no. 20, pp. 6575–6583, 2010.

[61] V. Alvarez, J. Santisteban, G. Domizzi, and J. Almer, "Phase and texture analysis of a hydride blister in a zr–2.5% nb tube by synchrotron x-ray diffraction," *Acta Materialia*, vol. 59, no. 5, pp. 2210–2220, 2011.

[62] O. Zanellato, M. Preuss, J.-Y. Buffiere, F. Ribeiro, A. Steuwer, J. Desquines, J. Andrieux, and B. Krebs, "Synchrotron diffraction study of dissolution and precipitation kinetics of hydrides in zircaloy-4," *Journal of Nuclear Materials*, vol. 420, no. 1, pp. 537–547, 2012.

[63] K. Une and S. Ishimoto, "Dissolution and precipitation behavior of hydrides in zircaloy-2 and high fe zircaloy," *Journal of Nuclear Materials*, vol. 322, no. 1, pp. 66–72, 2003.

[64] A. E. of Canada Limited, M. Puls, and W. N. R. Establishment, *Hydrogen-induced Delayed Cracking, 2, Effect of Stress on Nucleation, Growth and Coarsening of Zirconium Hydride Precipitates*. Pinawa, Man.: Whiteshell Nuclear Research Establishment, 1984.

[65] M. Louthan Jr and R. Marshall, "Control of hydride orientation in zircaloy," *Journal of Nuclear Materials*, vol. 9, no. 2, pp. 170–184, 1963.

[66] R. Singh, R. Kishore, S. Singh, T. Sinha, and B. Kashyap, "Stress-reorientation of hydrides and hydride embrittlement of zr–2.5 wt% nb pressure tube alloy," *Journal of nuclear materials*, vol. 325, no. 1, pp. 26–33, 2004.

[67] F. Nagase and T. Fuketa, "Influence of hydride re-orientation on bwr cladding rupture under accidental conditions," *Journal of nuclear science and technology*, vol. 41, no. 12, pp. 1211–1217, 2004.

[68] H.-H. Hsu and L.-W. Tsay, "Effect of hydride orientation on fracture toughness of zircaloy-4 cladding," *Journal of Nuclear Materials*, vol. 408, no. 1, pp. 67–72, 2011.

[69] D. Hardie and M. Shanahan, "Stress reorientation of hydrides in zirconium- 2.5% niobium," *Journal of Nuclear Materials*, vol. 55, no. 1, pp. 1–13, 1975.

[70] M. Leger and A. Donner, "The effect of stress on orientation of hydrides in zirconium alloy pressure tube materials," *Canadian Metallurgical Quarterly*, vol. 24, no. 3, pp. 235–243, 1985.

[71] A. Alam and C. Hellwig, "Cladding tube deformation test for stress reorientation of hydrides," *Journal of ASTM International*, vol. 5, no. 2, 2008.

[72] R. S. Daum, S. Majumdar, Y. Liu, and M. C. Billone, "Radial-hydride embrittlement of high-burnup zircaloy-4 fuel cladding," *Journal of nuclear science and technology*, vol. 43, no. 9, pp. 1054–1067, 2006.

[73] K. Sakamoto and M. Nakatsuka, "Stress reorientation of hydrides in recrystallized zircaloy-2 sheet," *Journal of Nuclear Science and Technology*, vol. 43, no. 9, pp. 1136–1141, 2006.

[74] L. Bell and R. Duncan, "Hydride orientation in zr-2. 5wt/onb, how it is affected by stress, temperature and heat treatment" report aecl-5110," *Atomic Energy of Canada Ltd*, 1975.

[75] S. Hong and K. Lee, "Stress-induced reorientation of hydrides and mechanical properties of zircaloy-4 cladding tubes," *Journal of nuclear materials*, vol. 340, no. 2, pp. 203–208, 2005.

[76] Y. Mishima and T. Okubo, "Effect of thermal cycling on the stress orientation and circumferential ductility in zircaloy-2," *Canadian Metallurgical Quarterly*, vol. 11, no. 1, pp. 157–164, 1972.

[77] Y. Nakada, W. Leslie, and T. Churay, "Stress-orienting of fe 16 n 2 precipitates in an fe-n alloy," *ASM TRANS QUART*, vol. 60, no. 2, pp. 223–227, 1967.

[78] J. Bai, N. Ji, D. Gilbon, C. Prioul, and D. Francois, "Hydride embrittlement in zircaloy-4 plate: Part ii. interaction between the tensile stress and the hydride morphology," *Metallurgical and Materials transactions A*, vol. 25, no. 6, pp. 1199–1208, 1994.

[79] M. Puls, "Atomic energy of canada limited report aecl-8381," *Atomic Energy of Canada, Mississauga, Ontario*, 1984.

[80] A. R. Massih and L. O. Jernkvist, "Stress orientation of second-phase in alloys: Hydrides in zirconium alloys," *Computational Materials Science*, vol. 46, no. 4, pp. 1091–1097, 2009.

[81] T. Kido and M. Sugano, "Development of a method to charge hydrogen into zirconium alloys." *Transactions of the Atomic Energy Society of Japan*, vol. 1, no. 4, pp. 469–471, 2002.

[82] R. Checchetto, G. Trettel, and A. Miotello, "Sievert-type apparatus for the study of hydrogen storage in solids," *Measurement Science and Technology*, vol. 15, no. 1, p. 127, 2004.

[83] E. Zuzek, J. Abriata, A. San-Martin, and F. Manchester, "The h-zr (hydrogen-zirconium) system," *Bulletin of alloy phase diagrams*, vol. 11, no. 4, pp. 385–395, 1990.

[84] J. Almer, U. Lienert, R. L. Peng, C. Schlauer, and M. Odén, "Strain and texture analysis of coatings using high-energy x-rays," *Journal of applied physics*, vol. 94, no. 1, pp. 697–702, 2003.

[85] A. Hammersley, S. Svensson, and A. Thompson, "Calibration and correction of spatial distortions in 2d detector systems," *Nuclear Instruments and Methods in Physics Research Section A: Accelerators, Spectrometers, Detectors and Associated Equipment*, vol. 346, no. 1, pp. 312–321, 1994.

[86] K. T. Erwin, O. Delaire, A. T. Motta, Y. S. Chu, D. C. Mancini, and R. C. Birtcher, "Observation of second-phase particles in bulk zirconium alloys using synchrotron radiation," *Journal of nuclear materials*, vol. 294, no. 3, pp. 299–304, 2001.

[87] R. S. Daum, "Hydride-induced embrittlement of zircaloy-4 cladding under plane-strain tension," Ph.D. dissertation, The Pennsylvania State University, 2007.

[88] M. Young, J. Almer, M. Daymond, D. Haeffner, and D. Dunand, "Load partitioning between ferrite and cementite during elasto-plastic deformation of an ultrahigh-carbon steel," *Acta materialia*, vol. 55, no. 6, pp. 1999–2011, 2007.

[89] X. Pan, X. Wu, K. Mo, X. Chen, J. Almer, J. Ilavsky, D. R. Haeffner, and J. F. Stubbins, "Lattice strain and damage evolution of 9–12% cr ferritic/martensitic steel during¡ i¿ in situ¡/i¿ tensile test by x-ray diffraction and small angle scattering," *Journal of Nuclear Materials*, vol. 407, no. 1, pp. 10–15, 2010.

[90] H. Shen and C. Lissenden, "3d finite element analysis of particle-reinforced aluminum," *Materials Science and Engineering: A*, vol. 338, no. 1, pp. 271–281, 2002.

[91] P. E. Armstrong and H. L. Brown, "Dynamic young's modulus measurements above 1000 c on some pure polycrystalline metals and commercial graphites," *Trans. Aime*, vol. 230, no. LADC-6100, 1964.

[92] R. L. Snyder, J. Fiala, and H. J. Bunge, *Defect and microstructure analysis by diffraction*. Oxford University Press Oxford, 1999, no. s 785.

[93] F. Jones, "The measurement of particle size by the x-ray method," *Proceedings of the Royal Society of London. Series A, Mathematical and Physical Sciences*, pp. 16–43, 1938.

[94] G. Williamson and W. Hall, "X-ray line broadening from filed aluminium and wolfram," *Acta metallurgica*, vol. 1, no. 1, pp. 22–31, 1953.

[95] T. Ungár, I. Groma, and M. Wilkens, "Asymmetric x-ray line broadening of plastically deformed crystals. ii. evaluation procedure and application to [001]-cu crystals," *Journal of applied crystallography*, vol. 22, no. 1, pp. 26–34, 1989.

[96] K. Une, K. Nogita, S. Ishimoto, and K. Ogata, "Crystallography of zirconium hydrides in recrystallized zircaloy-2 fuel cladding by electron backscatter diffraction," *Journal of nuclear science and technology*, vol. 41, no. 7, pp. 731–740, 2004.